UNIVERSITY OF COLORADO BOULDER

Physically based modeling of biological semi-flexible materials: a novel micromechanical model describing the viscoelastic-plastic response of agarose and fibrin networks

by

Victor Crespo-Cuevas

M.S., Industrial Engineering, Universitat Politècnica de Catalunya, 2016

B.S., Industrial Engineering, Universitat Politècnica de Catalunya, 2012

A thesis submitted to the faculty of the Graduate School of the University of Colorado at Boulder in partial fulfillment of the requirement for the degree of Doctor of Philosophy

Department of Mechanical Engineering

2023

Committee in charge:

Dr. Virginia L. Ferguson

Dr. Franck J. Vernerey

Dr. Jason Burdick

Dr. Sarah Calve

Dr. Rong Long

Crespo-Cuevas, Victor (Ph.D., Mechanical Engineering)

Physically based modeling of biological semi-flexible materials: a novel micromechanical model describing the viscoelastic-plastic response of agarose and fibrin networks.

Thesis directed by Professor Virginia L. Ferguson and Professor Franck J. Vernerey.

In this Ph.D. thesis, I investigated the mechanics of soft matter, specifically focusing on the viscoelastic-plastic response of agarose and fibrin networks. The study utilized a combination of experimental observations, statistically based continuum mechanics, and discrete numerical modeling techniques to develop physically based computational models of biological soft materials. In Chapter 2, I proposed a novel model for predicting the time-dependent behavior of agarose networks which offered insights into bond kinetics that can be applied to other biopolymer networks. Chapter 3 presented a coarse-grained, discrete numerical model for examining topological changes in transient semi-flexible networks, capturing the appropriate physics for various temperature limits and deformation rates. In Chapter 4, I concentrated on fibrin gels. I developed two models to better understand their behavior. The first, a comprehensive protofibril bundle model, was designed to capture the energetic penalty linked with highly stretched networks. The second, a fibrin fiber model, aimed to capture the macroscopic viscoelastic response of the gels and predict network realignment following applied deformation. This research has broad implications for biopolymer networks, bioengineering, tissue engineering, and cell-scale mechanobiology. By characterizing the critical microstructural features and dynamics that dictate the mechanical response of semi-flexible networks, I lay the foundation for further advancements in material choice, design, and the understanding of the interplay between soft matter physics and biological processes.

ACKNOLEDGEMENTS

I am deeply indebted to my advisor, Dr. Virginia L. Ferguson. Her support, empathic understanding, and tireless efforts have shaped this journey, and her guidance has been instrumental in my growth as a researcher, writer, and individual. The opportunity to join her group in 2018 was a turning point that I will forever cherish. Every moment spent in her lab has been a priceless learning experience.

My gratitude extends to my advisor, Dr. Franck J. Vernerey, for his patience, inspiring guidance, valuable critiques, and continuous encouragement throughout my tenure at the University of Colorado at Boulder. But above all of this, I am particularly thankful for the opportunity to join his research group in 2020 and for introducing me to the captivating world of biophysics.

My committee members, Dr. Jason Burdick, Dr. Sarah Calve, and Dr. Rong Long, along with all the academic mentors and collaborators I have encountered over the years, deserve a special acknowledgment. Their insightful guidance and constructive feedback have been invaluable in shaping this dissertation.

I am grateful to my former and current lab-mates, who warmly welcomed me into the Ferguson group and into the Vernerey group. Thanks to Dr. Kevin Eckstein, Dr. Andrew Tomaschke and Dr. Tong Shen, whose enduring support has been a source of strength and I am lucky to call them friends. Special thanks to Sam Lamont, whose expertise, dedication, and support, even from Paris, were a lifeline during challenging times. Your success in your Ph.D. is just around the corner, and I wish you all the best.

To my family, I am forever grateful. My parents have been exceptional role models, demonstrating hard work and perseverance. To my elder brother, Ivan, his wife, Patricia, and the best nephews in

the world, Juan and Liz. You have shaped me into who I am today, and I could not have asked for a better family.

I am indebted to my Boulder family: Laura Paz, Gerard Casas, Dr. Irene Francino, Dr. Oscar Fuentes, and Dr. Alberto Roper. You all have made my time in this beautiful city an extraordinary experience. A special thanks to Luis Rubio, my steadfast friend, who, despite being in Germany, has always been there for me. I am so fortunate to have you all as part of my family, and I am looking forward to our next adventures together. This achievement is also yours.

Ines, words cannot express my gratitude for your unwavering support throughout this journey. From the moment we learned about my acceptance to CU during our vacation, you have been my rock. A separate dissertation would be needed to encapsulate my gratitude for having you by my side. You made every step of this process worthwhile.

Finally, I would like to express my profound gratitude to Pere Balsells and the University of Colorado for entrusting me with their fellowship. Their commitment to keeping this program alive has made this thesis and many others possible. Without their support, none of this would have been conceivable.

TABLE OF CONTENTS

LIST OF FIGURES

Figure

LIST OF TABLES

Table

CHAPTER 1:

INTRODUCTION

Over recent decades, the field of soft matter physics has experienced a surge of interest, with a focus on subjects such as colloidal matter[1], membranes[2], gels[3], surfactants[4], liquid crystals[5], and polymers[6], among others. This burgeoning field serves as a bridge between life science and nanotechnology[7–9]. Comprehensive understanding of soft matter mechanics is essential, as it elucidates the governing principles of soft materials, which find applications in diverse domains, such as tissue engineering, materials science, and medical research. By employing sophisticated computational tools from continuum mechanics, such as finite element techniques and other related continuum and discrete modeling approaches, researchers can explore the mechanical behavior of soft materials with unprecedented depth and interpretation[10]. This ultimately leads to a better understanding of the underlying mechanisms and enables the development of novel materials and applications that harness the unique properties of soft matter.

1.1. MECHANICS OF SEMI-FLEXIBLE BIOPOLYMER NETWORKS

The vast majority of solid-like soft matter is made of networks of connecting elements. Numerous applications of random fiber network mechanics are found in soft matter physics. Many biological materials present a microstructure composed of a network of fibers that determines their mechanical characteristics. From a mechanical perspective, these fibrous materials may be thought of as acting as flexible or semi-flexible networks, based on the features of each individual fiber[11,12].

Whereas the behavior of flexible networks has been extensively studied, the mechanics of semi-flexible networks remain poorly understood due to their unique characteristics [6]. The interplay between bending and axial modes of deformation, and long-range correlations in their non-affine deformation field[13] make semi-flexible networks more challenging to analyze and model compared to their flexible counterparts, leaving many aspects of their behavior yet to be explored. An improved understanding of semi-flexible networks mechanics is crucial for novel insights into how various biological materials and their microstructures behave. Such advances in understanding will support researchers to develop better models and simulations, thus leading to improved understanding and manipulation of biological materials.

Characterizing the mechanics of semi-flexible networks has garnered more attention in recent years due to rising interest in comprehending the mechanical and rheological characteristics of complex systems, such as connective tissue and components within the extracellular matrix[14]. While existing models are descriptive, most do not connect the network topology with the macroscopic mechanical response. Such models lack accuracy as they do not account for the movement and rearrangement of molecules within the biopolymer network. Indeed, the mechanical response and fracture properties of soft polymeric materials strongly depend on their topological structures including local connectivity, bond types, and crosslinking density. Thus,

there is a need for more sophisticated models that accurately capture the complex interplay between network topology and mechanical properties. Developing such models will not only improve our understanding of the mechanical behavior of biological tissues but also have broader implications in areas such as material science and engineering[15].

The elasticity and deformation of many biological systems, including the cytoskeleton, collagenous connective tissues (i.e., cartilage and tendon), fibrin, and biopolymers such as agarose hydrogels among many others, are defined by the mechanics of random fiber networks. For example, the structure and composition of the extracellular matrix of blood clots directly influences how well these networks perform mechanically[16]. Fibrin, a crucial protein in blood clotting, forms a fibrous mesh that provides support to injured tissue and aids in the healing process[17]. The organization of the fibrin network changes in response to loading. In stress-free conditions, with no applied tensile or compressive loading, the orientation distribution of fibrin fibers is isotropic, while when a load is applied, the fibrin network aligns in the direction of deformation and fibers become more densely packed[18]. Similar to fibrin, agarose hydrogels are also characterized by their random fiber networks. Agarose gels exhibit unique properties such as biocompatibility, transparency, low protein absorption, and adjustable mechanical strength, making them suitable for various biomedical applications including drug delivery, cell culture, tissue engineering, and regenerative medicine medicine[13,19]. The mechanical strength of agarose hydrogels can be fine-tuned by altering factors such as the concentration of agarose or the gelation temperature[20]. This tunability enables researchers to create hydrogels with specific mechanical properties tailored to the requirements of a particular application. Thus, both fibrin and agarose hydrogels demonstrate the significance of understanding and manipulating the mechanics of

random fiber networks, as this knowledge enables researchers to create materials with specific mechanical properties tailored to the requirements of diverse applications in biomedicine.

Agarose and fibrin networks can be conceptualized as dynamic networks[21,22]. Bonds in dynamic networks have the potential to reversibly separate and reconnect, giving them a viscoelastic, nonlinear mechanical response. Even dynamic networks made up of components that appear to be simple can show sophisticated emergent dynamics. Engineers attempting to create synthetic versions of dynamic networks (i.e., dynamic gels used as scaffolds for tissue engineering) seek to understand how the local and physical interactions in these systems give rise to their globally emergent responses. This is because such systems may exhibit a variety of rich mechanical behaviors. Agarose gels are excellent candidates for tissue engineering as they are tunable, viscoelastic, and show a pronounced strain-stiffening response. These characteristics make them ideal to create *in vitro* environments to grow cells and develop tissues. Due to the presence of physical crosslinks in agarose supramolecular fibers form from the aggregation of double helices, their networks are assumed to be dynamic, wherein the polymer chains associate and dissociate over time[23,24]. Similarly, fibrin gels also behave as viscoelastic materials. The presence of knob-hole bonds within fibrin gels affect viscoelastic properties by changing their strength with tensile force[22]. These force-dependent cross-links may help fibrin gels resist large deformations and prevent premature rupture and directly affect the deformation of blood clots and wound healing matrices. Agarose and fibrin serve as examples of the broader class of biopolymer networks that are common in biological systems and play critical roles in various biological processes. Hence, understanding the factors that determine and regulate the viscoelasticity of biological materials like agarose and fibrin, as well as other biopolymer networks, is not only of considerable relevance to tissue engineering and regenerative medicine, but also to many applications in robotics (i.e., to

create soft robotic components such as actuators, sensors, and skins that can mimic the functions of biological tissues[25]), manufacturing (i.e., to create biodegradable polymers that reduce environmental pollution[26]) and food science (i.e., to create edible films and coatings that enhance the quality and safety of food products[27]).

1.2. TRANSIENT NETWORK THEORY: AN OVERVIEW

Previous attempts to model the mechanical behavior of semi-flexible networks frequently use multiscale models ranging from continuum methods (i.e., linear Maxwell or Kelvin-Voigt model[28]) to high fidelity discrete methods (i.e., molecular dynamics[29]) to predictably construct these networks or conversely comprehend their structure-property functions. Statistical mechanics stands out as an alternative to continuum models by connecting molecular physics to macroscopic mechanical behavior. Miehe and Goktepe (2004) developed a micro-sphere model to connect the stretch of molecular chains with polymer response[30,31]. In their approach, a chain's end-to-end distance is captured by a micro-tube that represents the chain's micro-mechanics. By homogenizing the micro-state variables on a unit sphere that depicts the chain orientation in three dimensions, the macroscopic response of the polymer network is computed. However, because viscoelasticity is brought on by the reptation motion of entangled chains, this theory can only describe static (i.e., covalent) networks. Further effort is needed to generalize this theory to describe the behavior of physical networks, where the viscoelasticity results from the breakage and reformation of physical cross-links. In this dissertation, the constitutive material models developed are based on the transient network theory (TNT)[12,32–34] that establishes a bridge between polymer chain configuration and the stress in the network.

Briefly, the TNT begins with the statistical treatment of networks comprised of randomly oriented flexible chains connected by reversible bonds with intrinsic association and dissociation rates, k_a and k_d, respectively (Figure 1.1). The TNT has been amply used to understand the molecular origin of the viscoelastic response by transient networks[3,10,35,36]. To provide the reader a general view of the proposed theoretical and numerical framework which will be used in all following chapters, some of the fundamental concepts of the TNT are introduced. In the TNT, the mechanical

response of a polymer can be described by the states of the chains and their contribution to the overall response of the network. TNT predicts the Cauchy stress of a dynamic network comprised entirely of linear entropic springs as $\boldsymbol{\sigma} = ck_bT\boldsymbol{\mu} + \pi\boldsymbol{I}$, where c is the attached chain concentration, k_b is the Boltzmann constant, T is the ambient temperature, $\pi\boldsymbol{I}$ is the isotropic pressure enforcing incompressibility, and $\boldsymbol{\mu}$ represents, in an average sense, the stretch experienced by chains in the network. If we assume that the chains deformation follows the macroscopic deformation $\boldsymbol{L}$ (i.e., affine deformation), it is possible to construct an evolution equation for the conformation tensor evolves according to $\dot{\boldsymbol{\mu}} = \boldsymbol{L\mu} + \boldsymbol{\mu L}^T - k_d(\boldsymbol{\mu} - \boldsymbol{I})$, where $\boldsymbol{L}$ is the velocity gradient $\boldsymbol{L} = \dot{\boldsymbol{F}}\boldsymbol{F}^{-1}$. Deformation is measured by the deformation gradient $\boldsymbol{F}(t) = d\boldsymbol{x}(t)/d\boldsymbol{X}$ which represents the linear mapping between the position vector $\boldsymbol{X}$ of a material point in the reference configuration and its position $\boldsymbol{x}(t)$ in the current configuration.

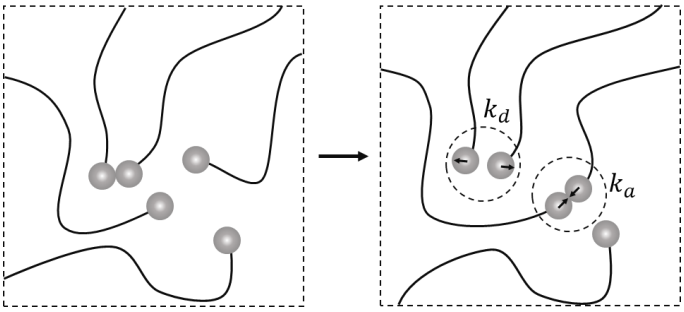

Figure 1.1. Schematic representation of dynamic bonds in a polymer network, where dissociation and re-association happen with rates of k_a and k_d, respectively.

The TNT enables us to clearly link molecular processes at the level of polymer chains (i.e., sliding[37], entanglement[38], and the breaking and reformation of physical bonds[39]) to the macroscopic response of the network. The Maxwell and Kevin-Voigt models[40–42], which are phenomenological viscoelastic models, are divergent from this. Details can be found in Chapter 2.

1.3. MESOSCALE MODELING OF COMPLEX POLYMER NETWORKS

Nonetheless, macroscopic statistical frameworks, such as the TNT, are incapable of capturing pronounced property gradients and the non-affine deformation introduced by hierarchical network architectures and transient bonds. High-resolution discrete methods (e.g., molecular dynamics or dissipative particle dynamics) can mitigate these shortcomings, but often incur substantial computational costs, complicating accurate microscale-to-macroscale parameter mapping. Hence, researchers have adopted a third category of mesoscale network models, employing coarse-grained elements to maintain microstructural insights while reducing computational demands.

Mesoscale modeling has emerged as an effective method for studying complex polymer networks, as it circumvents the high computational cost associated with simulating the elemental units of a network[43]. By employing coarse-grained representations of entire chains and prescribing their mechanical properties through statistical models, such as the ideal Gaussian model[44], mesoscale models facilitate the investigation of intricate microstructural changes occurring during network evolution[45–47]. Extensive research utilizing mesoscale models has elucidated the limitations of continuum models in predicting network mechanics near the percolation threshold due to the affine assumption[48]. Mesoscale models, on the other hand, inherently track network topological evolution and enable probabilistic rupture of bonds through theoretical frameworks like Eyring's[49] or Bell's[50]. Recently, these models have been used to examine the influence of chain properties and concentrations in the permanent damage, mechanical toughness, and loading rate-dependence[51,52].

The logical progression of such research is to employ mesoscale modeling to explore dynamic networks with reversible bond dissociation. Although biophysicists have investigated active dynamic systems like actin-myosin or cytoskeletal networks using mesoscale approaches[53,54], these studies veil the isolated effects of factors such as topology, chain properties, and bond

kinetics, which are of primary interest in the context of thermally driven dynamic networks. Conventional methods for modeling dynamic cross-linking networks (i.e., molecular dynamics-Monte Carlo simulations or the development of statistical approximations[55]) face the same challenges of computational cost and inaccessibility to larger time and length scales as encountered with elemental unit simulations.

Consequently, the development and application of a generalized mesoscale framework for networks with reversible bonds presents a promising avenue for advancing our understanding of complex polymer networks. Embracing this approach will facilitate the exploration of their mechanics and properties, ultimately contributing to the optimization of material design and performance.

1.4. OVERARCHING OBJECTIVES

In summary, there exists a need to accurately model and predict the combination of elastic stresses, viscous flow and continuous changes in material properties occurring in semi-flexible biopolymer networks. Numerical modeling developed based on viscoelastic material models has therefore become an attractive tool to understand and eventually control the deformation process of these networks. Thus, the **principal objective** of this dissertation was to develop physically based computational models of biological soft materials and provide new insights in the emergent viscoelastic-plastic response of agarose and fibrin networks employing a combination of experimental observations, statistically based continuum transient network theory (TNT), and discrete numerical modeling techniques. The **first aim** of this work explored the nonlinear viscoelasticity of agarose hydrogels by conceptualizing them as biopolymer networks with transient bond dynamics. This theoretical contribution was supplemented by an experimental component that consisted of creep and stress-relaxation tests. We found that the nonlinear rheology of agarose gels originates from two distinct mechanisms which are characterized by distinct time scales. The **second aim** of this work was to develop a modeling framework integrating fiber realignment and associated stress-stiffening with an underexamined characteristic of semi-flexible biological networks: their viscoelastic response, self-healing, and restructuring over long-time scales. These networks frequently exhibit dynamic crosslinks with temporal association and dissociation, providing them with the capacity for temporal reconfiguration. The **third aim** of this work was to evaluate the nonlinear viscoelastic and plastic mechanical response of fibrin networks at their protofibril and fiber level. We developed a mesoscale model to capture the dynamic cross-linking (detachment and attachment events) between fibrin fibers and to allow us to relate the macroscopic viscoelastic response directly to the topological evolution of the fibrillar network.

1.5. SUMMARY OF GOALS AND AIMS

Overarching goal of this dissertation: *Develop physically based computational models of biological soft materials to provide new insights in the emergent viscoelastic-plastic response of agarose and fibrin networks while employing a combination of experimental observations, statistically based continuum transient network theory (TNT), and discrete numerical modeling techniques*. In support of this overarching objective, I completed the following three Aims:

- Aim 1: Poroviscoelasto-Plasticity of Agarose-Based Hydrogels

Using agarose gels as a model system, Aim 1 evaluated the complex time-dependent mechanical response under unconfined compression. We developed a physics-based constitutive model that can accurately describe time-dependent behavior by using the foundation of the transient network theory. The model presented in this study can be used to provide control guidance on the material design in numerous applications that necessitate the use of agarose-based gels.

- Aim 2: Time-Dependent Mechanics of Dynamically Cross-Linked Semi-flexible Networks

Aim 2 developed a mesoscopic model framework to correctly describe the mechanical response of semi-flexible rods. The model was built in a highly parallelized framework (i.e., LAMMPS). The generation of this model will greatly improve the spatiotemporal scales that may be modeled through these methods, thus permitting broader investigation of materials with higher degrees of hierarchical microstructure and heterogeneity.

- Aim 3: A Mesoscale Viscoelastic-Plastic Constitutive Model of Fibrin Gels

Aim 3 sought to adapt the model presented in Aim 2 to fibrin networks and to define their mechanical behavior at a protofibril and fiber length scale (i.e., mesoscale). Developing a robust mesoscopic model of protofibril bundles and fibrin gels enhanced our understanding of the time-

dependent mechanical properties of fibrin at different length-scales and may have significant implications for the field of mechanobiology.

This dissertation has significantly enhanced our comprehension of soft matter mechanics, particularly the viscoelastic-plastic behavior of agarose and fibrin networks. This has been achieved by creating cutting-edge computational models that combine experimental observations, statistically based continuum mechanics, and discrete modeling methods. By identifying the crucial microstructural characteristics and dynamics that govern the mechanical response of semi-flexible networks, we have established the groundwork for future progress in cellular length-scale mechanobiology and the development of innovative materials for various applications. As we continue to improve and validate our models, we expect our research to deepen our understanding of the connections between soft matter physics and the biological processes they influence. This will ultimately lead to solutions for challenges in biotechnology, nanotechnology, and beyond.

CHAPTER 2:

POROVISCOELASTO-PLASTICITY OF AGAROSE-BASED HYDROGELS[*]

Agarose gels are excellent candidates for tissue engineering as they are tunable, viscoelastic, and show a pronounced strain-stiffening response. These characteristics make them ideal to create *in vitro* environments to grow cells and develop tissues. As many other biopolymers, viscoelasticity and poroelasticity coexist as time-dependent behaviors in agarose gels. While the viscoelastic behavior of these hydrogels has been considered using both phenomenological and continuum models, there remains a lack of connection between the underlying physics and the macroscopic material response. Through a finite element analysis and complimentary experiments, we evaluated the complex time-dependent mechanical response of agarose gels in various conditions. We then conceptualized these gels as a dynamic network where the global dissociation/association rate of intermolecular bonds is described as a combination of a fast rate native to double helices forming between aligned agarose molecules and a slow rate of the agarose molecules present in the clusters. Using the foundation of the transient network theory, we developed a physics-based constitutive model that accurately describes agarose behavior. Integrating experimental results and model prediction, we demonstrated that the fast dissociation/association rate follows a nonlinear force-dependent response, whose exponential evolution agrees with Eyring's model based on the transition state theory. Overall, our results establish a more accurate understanding of the time-dependent mechanics of agarose gels and provide a model that can inform design of a variety of biopolymers with a similar network topology.

[**] The results presented in this chapter have been published to *Soft Matter* as: Crespo-Cuevas, V. Ferguson, V. L., Vernerey, F., Poroviscoelasto-Plasticity Of Agarose-Based Hydrogels.

2.1. BACKGROUND AND MOTIVATION

Biopolymers are used extensively as both commodity materials and for specialized applications[56–58]. For example, chitin is important for medical devices and wound-healing dressings[59], carrageenan films play an important role in extending the shelf life of foods[60], alginate is used to prevent dehydration of meats[61], and agar is common for culturing cells[62–64]. Biopolymers are selected for their ease of manufacture from natural precursor materials as well as for their ability to bear loads over long time scales. However, biopolymers also exhibit complex behaviors that may influence their durability and function. An accurate characterization of these materials is thus critical to guide material selection and design, yet many aspects of how biopolymers respond to loads applied over time remain poorly understood. Their physical behaviors are complex and vary across multiple length scales[65], where many behave as semiflexible networks. Typically, these polymeric systems have supramolecular assemblies which can vary between about one nanometer and tens of nanometers. Of particular interest are agarose-based hydrogels, which are commonly used as scaffolds in tissue engineering due to their low cost, biodegradability, and highly controllable elastic properties[20]. Agarose gels are viscoelastic semiflexible biopolymer hydrogels whose mechanical response depends on the polymer concentration[66] and has been demonstrated to exhibit a strain stiffening response that is likely to influence cellular responses[67,68]. While bulk properties are important to bear loads, cells respond directly to the small-length scale properties and behavior of their host scaffolds. Modulus, viscoelasticity, plasticity, and nonlinear elasticity of substrates and scaffolds influence cells and alter the fundamental processes of growth, proliferation, migration, and differentiation[6,19].

To better understand the characteristic mechanics and time-dependent response of agarose gels, let us first describe its network features. Below the gelation point, double helices are formed

through the conglomeration of agarose molecules. Each agarose molecule participates in more than one double helix. Supramolecular fibers form from the aggregation of double helices through hydrogen bonding. These bonds govern the self-gelation of agarose gels (Figure 2.1.A) and enable the network to be dynamic through bond formation and dissociation which dissipates elastic stored energy when exposed to mechanical stimuli. The agarose molecules within the supramolecular fibers of the network structure thus possess a solid-like behavior that has been proposed to be capable of fast energy dissipation. In contrast, agarose molecules present in the clusters or junctions and that are not aligned can dissipate energy much more easily as they slide over adjacent molecules thus generating a fluid-like behavior[24]. Hence, it has been proposed that bond exchange processes taking place in the junctions will correspond to longer relaxation times or slower dissipation of the stored elastic energy. Clusters formed by several suprafibers within agarose networks increase the number of connected bonds under deformation. The adjacent agarose molecules that are not part of the cluster in a stress-free configuration are then able to form new crosslinks which increases the size of the cluster and strengthens the network. This process enables agarose to dissipate stress when loaded over long time periods. Elucidating the complex behavior of agarose gels is crucial to design more controllable materials, but also to elucidate the factors leading to cell responses when subjected to externally applied loads. In addition, a deeper understanding of agarose behavior will provide novel insight into many biological materials which present similar network topology (i.e., actin filaments and collagen gels) (Figure 2.1.B).

The behavior of agarose gels, and many other biopolymers, is considered to be poroviscoelastic because of their high-water content[69–71]. Fluid movement and mass transport through the solid network influence behavior. However, existing poroviscoelastic models fail to connect the network topology with the mechanical response of the solid phase within hydrogels. Such models lack

accuracy as they do not account for the movement and rearrangement of molecules within the polymer network. Generally, existing mathematical models used to characterize the macroscopic mechanical response of agarose are empirical. Most either describe the mechanical response by approximating its structure as a combination of simple linear elements (i.e., Maxwell or Kelvin-Voigt model) or describe the stress-strain relations from the stored elastic energy expressions (i.e., Neo-Hookean or Holzapfel model). Studies using a linear combination of phenomenological models, such as Prony series viscoelastic model[72], can broadly be found in literature to describe the time-dependent response of agarose-based hydrogels. For example, Chen *et al.* (2011)[73] used this approach to study the deformation of chondrocytes seeded in agarose gels while Pauly *et al*. (2017)[74] investigated the effects of additives on the mechanical properties of agarose hydrogels. On the other hand, Caccavo and Lamberti (2017)[75] used fundamental balance laws to describe the poroviscoelastic behavior of hydrogels under large deformation, and applied it to agarose-based hydrogels[76]. This latter model provided an important step towards the development of refined models for biopolymers; however, this modeling approach is empirical which limits its use for design purposes. High-precision atomistic simulations, such as molecular dynamics, have been the subject of increasing developments in the last two decades. The molecular modeling of hydrogels incorporates into a model every single element that is part of the system (i.e., atomic positions, velocities, and forces). In this context, Casalini (2013)[29] developed a molecular model of an agarose-carbomer hydrogel to explore the effect of mesh size on solvent diffusion at low solute concentration. Although atomistic models remove all the assumptions that limit the application of a specific model, they are still computationally expensive and difficult to apply to polymeric networks models at large time scales. Thus, while viscoelasticity in agarose networks have been

studied extensively, no studies to date evaluate if the time-dependent response of hydrogels can be accurately described by dynamic bond evolution.

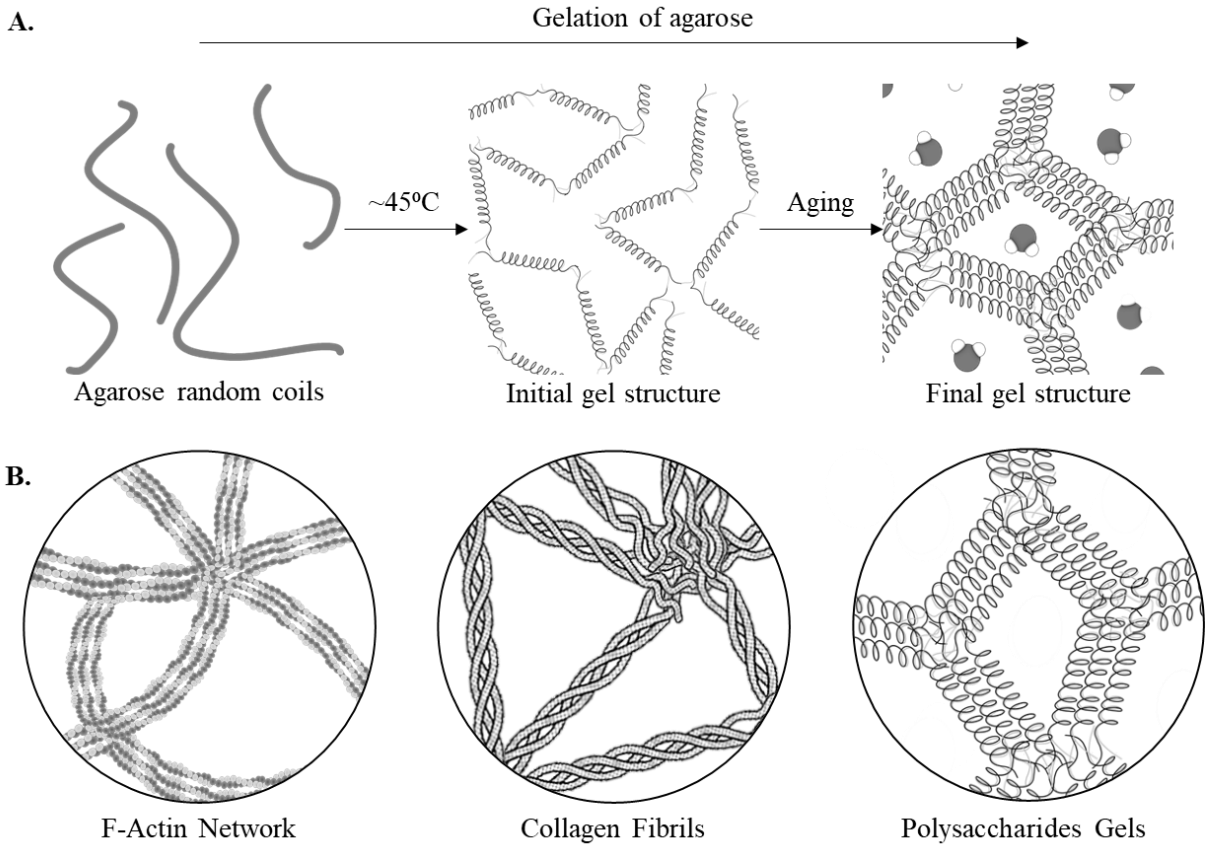

Figure 2.2. A. Gelation mechanism of agarose, from left to right: When water is added to agarose and it is heated up, agarose untangle and forms random coils. As the agarose cools (~45^{o}C), coils pair to form helices. As the temperature continues to drop, the helices bundle and form higher-order assemblies (suprafibers) that are coincident with water inside the gel. **B**. Schematic representation of different biopolymer networks showing cluster and thick fibers structure.

In this study, we connect the viscoelastic macroscopic response with the chain-level physics of agarose-based hydrogels. This work seeks to establish a fundamental understanding of mechanisms responsible for nonlinear viscoelasticity of agarose hydrogels by adapting the

Transient Network Theory (TNT)[12] to the case of agarose networks. More specifically, the TNT is modified to capture the force-dependent response of the fast bond dynamics observed during creep and to capture the nonlinear plastic flow-like behavior observed during the multi-step stress-relaxation experiment. We propose bond dynamics as a novel mechanism for describing strain-stiffening and force-dependent viscoelastic material behavior of agarose. With new data we sought to better understand the time-dependent mechanics of agarose gels to inform their design and to provide a model that may be extended to a range of biopolymers which share similar network topology. The manuscript is organized as follows. In Section 2, we present and analyze experimental results on the behavior of agarose subjected to unconfined compression and study the poroelastic contribution on the overall time-dependent response. In Section 3 we review the main elements of the TNT to model the response of dynamic polymer networks and introduce the nonlinear bond dynamics of agarose-based gels based on network topology. We then modify the TNT to capture the experimental observations reported in Section 2. Finally, in Section 4, we provide a comprehensive overview of the model.

2.2. CHARACTERIZATION OF THE TIME-DEPENDENT RESPONSE OF AGAROSE UNDER UNCONFINED COMPRESSION

In this section, we present and analyze experimental results on the behavior of agarose subjected to unconfined compression. We described the time-dependent mechanical response of agarose gels for multi-step stress-relaxation and steady creep conditions with the objective of establishing a connection with chain-level physics. Because agarose is a biphasic material comprised of a solvent-filled biopolymer network, we first aimed to characterize the role of poroelastic effects, i.e., the time dependence of the response related to solvent transport, on the gel's overall response. Thus, finite element analysis (FEA) was used to model and reproduce fluid transport in experimental specimens during loading over time.

2.2.1. Experimental methodology

Agarose Gel Fabrication. Hydrogels were prepared by dissolving 5%, 7.5% and 10%, (w/w) agarose (Sigma A9539) into phosphate buffered saline (PBS, pH 7.4, Invitrogen), and while stirring the agarose powder was slowly added to prevent clumping. The solution was weighed, covered with aluminum foil to reduce evaporation, and boiled (~95^{o}C) and magnetically stirred to maintain homogeneity for 5-10 minutes until agarose was dissolved. Agarose solutions were drawn into 3-, 5-, and 10-ml syringes cooled at room temperature. The hydrogels were removed from the syringes and cut into 8.66 mm, 12 mm and 16 mm lengths, respectively, to create 1:1 cylinders (height:diameter ratio).

Unconfined Compressive Multi-step Stress-Relaxation Test. A total of 15 samples were swelled to equilibrium in PBS for 48 h. Unconfined Compressive stress-relaxation testing (n = 3 samples/composition/dimension) was conducted on a Mechanical Testing System (MTS Insight II; Eden Prairie, MN; 250 N load cell; data recorded at 1 Hz) at room temperature; testing was

performed with samples immersed in PBS. Aluminum compression platens were rigid, impermeable, and smooth. A minimum contact force of 30 mN ensured full contact between platen and sample (Figure 2.2.A). A USB-camera (Dino-Lite 1.3MP EdgePLUS AM4117MZT) was used to assess for full contact prior to testing as well as to evaluate uncompressed, fully compressed, and recovered (48 hours of swelling after testing) dimensions to calculate lateral expansion. The test profile included four incremental steps in strain ϵ = {5%, 10%, 15%, 20%}. Each of these stages was divided into a compression phase and a relaxation phase. Samples were deformed at a strain rate of $\dot{\epsilon}$ = 0.05/s over 1 s, and then each strain was held for 5 h to reach an equilibrium stress state (Figure 2.2.B).

Water absorption/release quantification. After swelling in PBS for 48 hours, 5% w/w samples (*n* = 3) were weighed for initial mass m_0 (before mechanical testing and final mass m_f (after stress-relaxation experiments). Samples were weighed quickly to avoid water reabsorption and minimize evaporation, and the amount Δm of solvent exchanged with the media Δm was calculated. This procedure was used for the lower agarose concentration gels since their higher porosity (Table 1) made them best candidates to have larger values for Δm. Samples were next re-submerged in PBS and weighed after 48 hours to assess for mass of fluid reabsorbed.

Unconfined Compressive Creep Test. Unconfined compressive creep tests were also conducted to evaluate short-term time-dependent responses. Creep testing was performed in PBS at room temperature on an MTS with closed-loop load control. A total of 9, cylindrical, 12x12 mm samples (*n* = 3/group) were subjected to constant compressive stress based on the overall strains achieved after a fast-loading stage ($\dot{\epsilon}_l$ = 0.05/s.). The overall strains achieved during the loading stage were ϵ_l = {1%, 2.5%, 5%, 7.5%, 10%, 15%}. The loading stage was followed by a 120 s creep hold at ϵ_l.

2.2.2. Experimental approach: multi-step stress-relaxation

The multi-step stress relaxation depicted in Figure 2.2. C-E shows the mean stress versus time response of the three different sample sizes for each of the three agarose gels compositions. At each level of applied strain, the stress increased immediately after the step-strain application, followed by a relaxation stage that reaches a quasi-steady value, referred to as the plateau stress σ_p in the remainder of the manuscript. We observed that this value increases with the applied strain while being independent of specimen size. Equilibrium values for the stress at the end of the stress-relaxation testing were determined to be 0.028 ± 0.00082 MPa, 0.055 ± 0.0011 MPa and 0.083 ± 0.0005 MPa for 5% w/w, 7.5% w/w and 10% w/w respectively. The stress relaxation data were consistent between different samples showing a small variability.

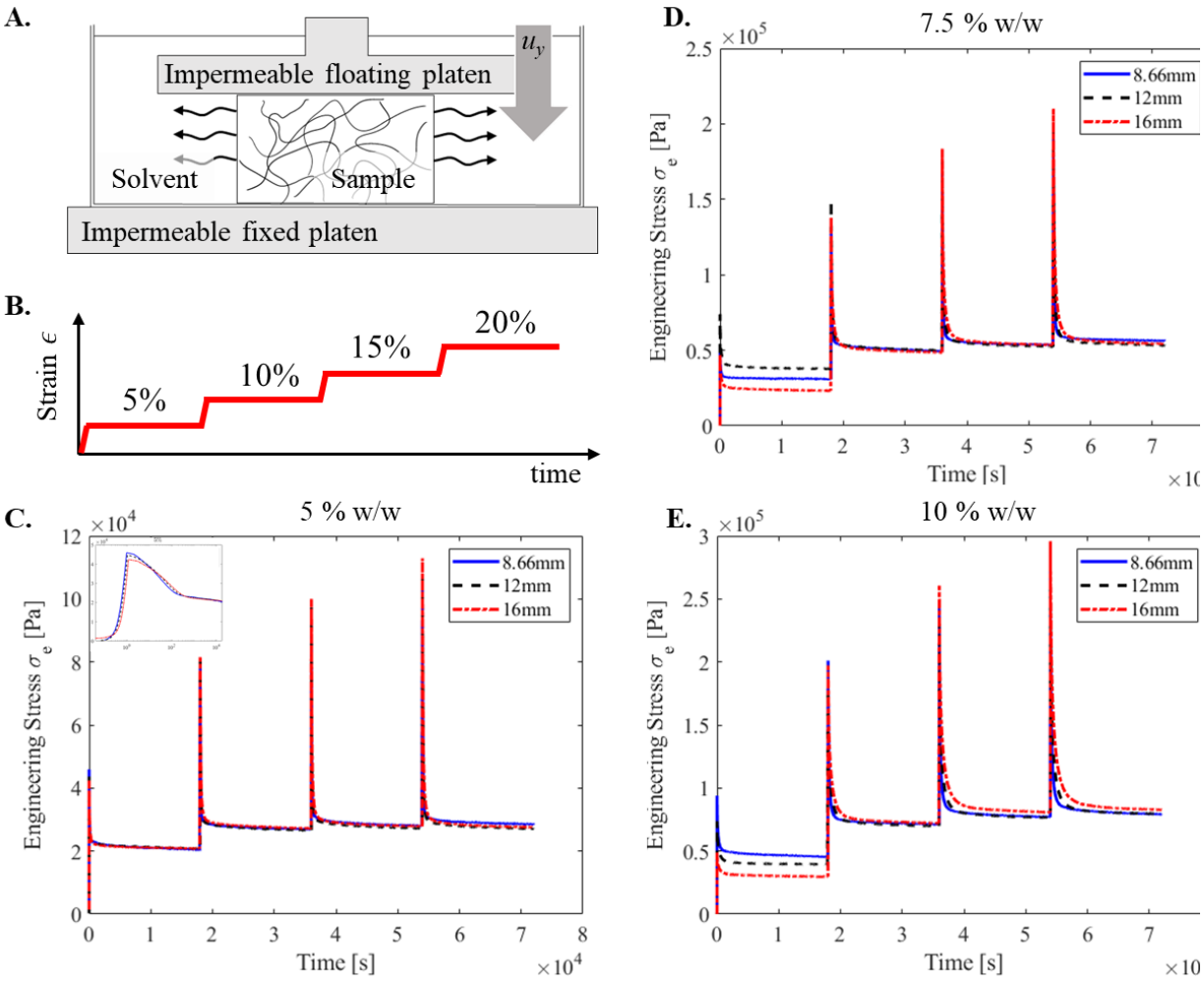

Figure 2.3. **A**. Schematic of the unconfined compression test of a cylindrical disk of hydrated hydrogel. **B**. Strain vs. time function features multiple steps with holding times to observe relaxation. **C**, **D,** and **E.** Experimental results obtained from multi-step stress-relaxation (8.66 mm, 12 mm, and 16 mm) for 5%, 7.5%, and 10% w/w agarose compositions, respectively. For each dimension, the averaged data is represented. For each composition, agarose gels showed the same long-term stress-relaxation response independent of the sample size. The inset in **C**. shows the stress evolution for the first loading and relaxation step in a semilogarithmic scale along the x-axis.

A similar "stress-plateau effect" behavior was observed in multi-step stress relaxation testing (with a 30 minute relaxation period) on the data reported by Roberts *et al.* (2011)[66] in their comparative study of the viscoelastic mechanical behavior of agarose and poly(ethylene glycol) hydrogels. Because of the relatively short time used between step strains in this previous study, the stress does not plateau as clearly as reported here although general trends are constant between the two studies.

2.2.3. Experimental approach: steady-state creep.

When subjected to a constant compressive load, the agarose sample displayed a combination of elastic deformation and creep as described below and as shown in Figure 2.A. First, following a period of fast elastic deformation, the specimen displayed a transitory regime where creep rate first substantially decreased with respect the loading rate $\dot{\epsilon}$ = 0.05/s and then later increased before reaching a steady-state creep (Figure 2.3.C). We also observed a convergence of the strain rate to a constant over time, which indicated steady-state creep and not consolidation effects from fluid transport out of the gel. We further noted that the average creep rate increased with applied stress (Figure 2.3.B), suggesting that the creep response of agarose is force dependent. At higher loads, however, creep could only be sustained for a while before the specimen ruptures. We finally did not notice major differences between the creep response of agarose with different compositions.

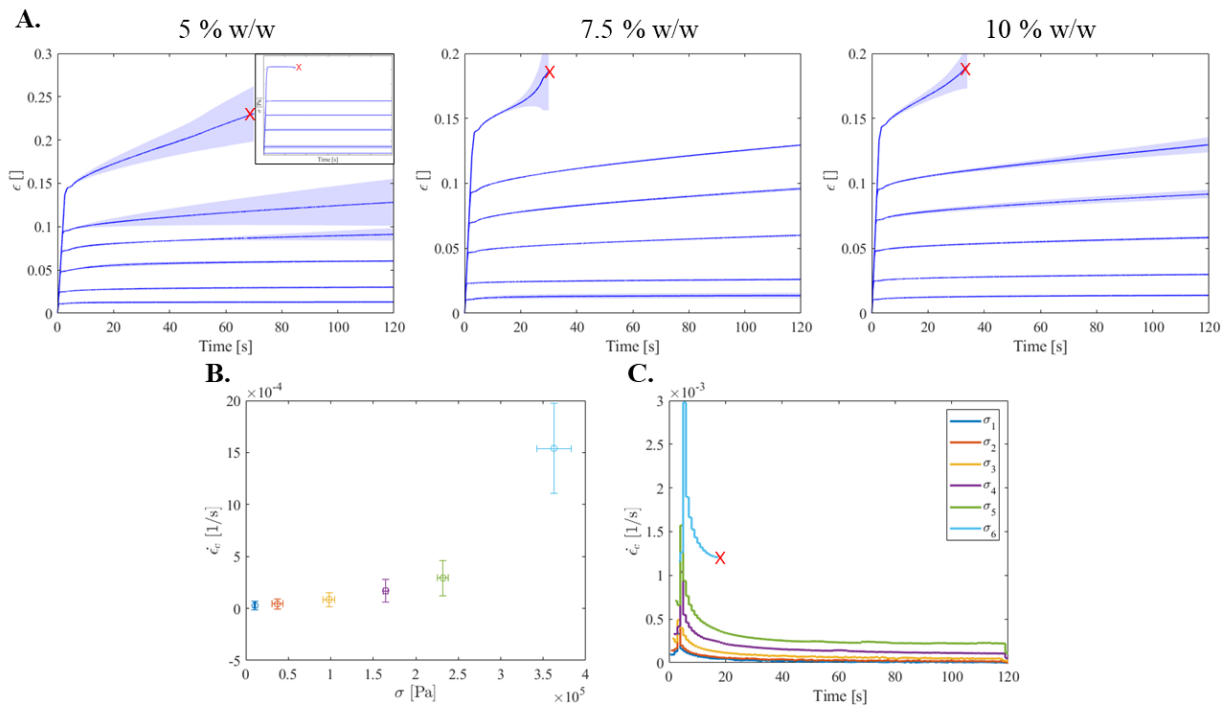

Figure 2.4. A. Experimental results obtained from creep tests of 12 mm height (and diameter) samples for each of the agarose compositions (n = 3/composition). Data is reported using a solid blue line (average values from samples tested), and a blue region (± standard deviation). The red-cross indicates mechanical failure. Agarose gels showed same creep response independent of agarose composition. **B.** Evolution of the average data for the creep strain rate $\dot{\epsilon_c}$ respect the average data of the constant stress applied σ_i ($\sigma_1 < \cdots < \sigma_6$) during the creep test. **C.** Evolution of the average data for the creep strain rate $\dot{\epsilon_c}$ over time for the different constant stresses applied σ_i. Red-cross indicates the mechanical failure.

2.2.4. Poromechanical effects

As most biopolymers, agarose can be considered as a biphasic mixture consisting of two constituents: a solid skeleton phase that is intermixed with a fluid phase. In the following, we therefore use superscripts s and f to denote the solid and fluid phases, respectively[69,77,78]. For

simplicity, the solid matrix is assumed to have an isotropic and uniform pore distribution on the whole domain while the mixture is assumed to have reached its equilibrium swollen state so it can be considered fully saturated. During deformation, however, the fluid can move relative to the solid skeleton, producing an effective time-dependence of the mixture, independently of the material response of the polymer matrix. This poroelastic effect brings a challenge to data interpretation as it is difficult to decouple the viscoelastic and poroelastic origins of the material's time behavior[79–82]. The volume fraction $n^{\alpha}(\boldsymbol{X}, t)$ of phase α ($\alpha = s$ or f) is defined as $n^{\alpha}(\boldsymbol{X}, t) = \frac{dv_{\alpha}}{dv}$, where $\boldsymbol{X}$ is the material coordinate, t is the time, and dv_{α} is the differential volume fraction of constituent α. The saturation condition implies that $n^{s} + n^{f} = 1$ and the total Cauchy stress can be decomposed into a solid and fluid component as[83]:

$$\boldsymbol{\sigma} = \boldsymbol{\sigma^{s}} + \boldsymbol{\sigma^{f}} = \boldsymbol{\sigma^{s}} - p^{f}\boldsymbol{I} \qquad 2.1$$

Here, p^{f} stands for the fluid pressure, $\boldsymbol{\sigma^{s}}$ is partial stress of solid skeleton[84] and $\boldsymbol{I}$ is the identity tensor. Interstitial fluid flow is modeled based on isotropic Darcy's law as $\nabla p^{f} = -\frac{1}{K}\frac{e}{1+e}(v^{f} - v^{s})$[85] where e is the void ratio, K is the hydraulic conductance, v^{s} is the velocity of the solid phase and v^{f} is the velocity of the fluid phase, as before.

To explore the extent of these effects on material response, we implemented the above linear poromechanics model into a general-purpose FEA software Abaqus 2019 (Dassault Systèmes Simulia Corp., USA). The specimen was modeled as an axisymmetric cylinder around its axis of revolution ($r = 0$) (Figure 2.5.B). Solvent transport was assumed isotropic and modeled by defining the hydraulic conductance of the fluid K, the void ratio e and the specific weight of the fluid γ_{s}. Gu *et al.* (2003)[86] described the evolution of K and e as a function of the deformation applied to agarose gels (detailed description on Appendix I). The compression step was run using the SOILS

analysis in Abaqus, which accounts for the pore pressure response and permeability. Because large deformation was used on our tests, the nonlinear geometric option (NLGEOM) was applied. To avoid discontinuities on the step resolution, the maximum pore pressure change per increment was set to 10 Pa.

Regarding boundary conditions, the fluid pore pressure p^f was set to zero on the cylindrical periphery (right side) to allow the fluid flow in the radial direction. Furthermore, to simulate the rigid and impermeable platen, all displacements and rotations were constrained using an encastre boundary condition on the bottom platen. The contact with the platens compressing the hydrogels was assumed to be perfectly lubricated and defined as a frictionless contact. Two different predefined fields were created on the initial step. The first one was used to initialize the internal state variables, which were set to zero. The second one defined the initial void ratio of the sample and was set to e_0 (see Appendix I).

Nonlinear analysis was performed using the Newton-Raphson algorithm. The hydrogel sample was modeled by the coupled pore-fluid/stress CAX8P elements, 8-node quadrilateral axisymmetric elements that consider biquadratic displacement and bilinear pore pressure. By subsequent mesh refinements, the results presented here were demonstrated to be mesh-size independent.

This model was used to simulate the two different tests conducted for this study: multi-step stress-relaxation and creep. To simulate stress-relaxation, a displacement u_y was prescribed on the top platen using a tabular amplitude to match the strain previously described in Section 2.1. To simulate creep, a range of pressures P_y were prescribed to the top platen with its respective tabular amplitude as well to simulate a constant strain ratio during the compression stage. To assess the role of poromechanics alone, we first assumed that the solid skeleton behaves as a compressible

Neo-Hookean hyperelastic solid. In this context, the sample deformation is measured by the deformation gradient $\boldsymbol{F}(t) = d\boldsymbol{x}(t)/d\boldsymbol{X}$ which represents the linear mapping between the position vector $\boldsymbol{X}$ of a material point in the reference configuration and its position $\boldsymbol{x}(t)$ in the current configuration (Figure 2.4). In the case of unconfined compression, this tensor takes the simple form $\boldsymbol{F}(t) = diag[\lambda, \lambda_l, \lambda_l]$, where $0 < \lambda \leq 1$ is the length ratio along the vertical direction and $\lambda_l \geq 1$ represents the lateral length ratio.

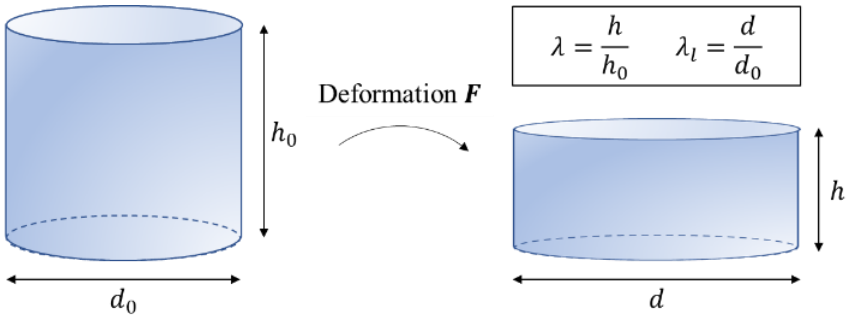

Figure 2.5. Conceptual diagram of deformation gradient tensor $\boldsymbol{F}$, the length ratio along the axial direction λ and the lateral length ratio λ_l.

The material strain is defined by the Finger deformation tensor (or left Cauchy-Green deformation tensor) $\boldsymbol{b} = \boldsymbol{F}\boldsymbol{F}^T$, which may further be decomposed into a volumetric component $J_e = \sqrt{\det \boldsymbol{b}}$ and an isochoric component $\bar{\boldsymbol{b}} = J_e^{-\frac{2}{3}} \boldsymbol{b}$. With these definitions, the strain energy density (per reference volume) of our compressible Neo-Hookean model is provided by

$$\psi = c_{10}\left(\mathrm{tr}\,\bar{\boldsymbol{b}} - 3\right) + \frac{1}{D_1}(J_e - 1)^2 \qquad 2.2$$

The material constant c_{10} and D_1 can further be written in terms of the more familiar elastic modulus E_s and the Poisson's ratio ν_s of the solid network respectively:

$$c_{10} = \frac{E_s}{4(1+\nu_s)} \; and \; D_1 = \frac{6(1-2\nu_s)}{E_s} \qquad 2.2.b$$

The true (Cauchy) stress tensor can then be derived as:

$$\boldsymbol{\sigma} = \frac{2}{J_e}\boldsymbol{b}\frac{\partial \psi}{\partial \boldsymbol{b}} = \frac{2}{J_e}c_{10}\mathrm{Dev}\,\bar{\boldsymbol{b}} + \frac{2}{D_1}(J_e - 1)\boldsymbol{I} \qquad 2.3$$

where the deviatoric part of $\bar{\boldsymbol{b}}$ is given by $\mathrm{Dev}(\bar{\boldsymbol{b}}) = \left(\bar{\boldsymbol{b}} - \frac{\mathrm{tr}\,\bar{\boldsymbol{b}}}{3}\boldsymbol{I}\right)$. The Poisson's ratio ν_s for the solid network was experimentally determined by imaging and measuring dimensions of each sample before compression and 50 minutes after the load was applied. Poisson's ratio was found to be ν_s = 0.17, which is in good agreement with previous studies[70,87]. The Poisson's ratio in this study was assumed to remain constant during testing.

To obtain the elastic modulus E_s of the network, an optimization algorithm was developed to directly compare the contact force from modeling results and the experimental data (see Appendix III). In this case, contact force obtained from first compression stage (ϵ = 0.05) on the multi-step stress-relaxation on 5% w/w agarose gels was used. E_s is set to be equal to 0.81 MPa.

Numerical simulations together with experimental findings indicate that poromechanics plays only a minor role in stress relaxation. From simulations, we can state fluid transport occurred within the first 2000 s (~ 35 min) (Figure 2.5.C and 5.D); then stress remained constant until the end of the simulation.

2.2.5. Experimental confirmation of poromechanical effects

We next sought to experimentally confirm our finding that poroelasticity did not dominate the behavior of agarose under the parameters applied in our computational analysis. Mass loss from samples was performed to experimentally confirm the minor role of energy-dissipation from

poromechanics (Table 2.1). The amount of water released increased with increasing sample diameter due to the higher water content in the initial state. In relative terms, Table 2.1 shows that the amount of water loss remained constant with respect the initial gel mass $\left(\|\Delta\overline{m}\| = \left\|\frac{\Delta m}{m_1}\right\| = 10.1\%\right)$, independently of sample size.

d [mm]	m_1 [g]	Δm [g]
8.66	0.57 ± 0.022	- 0.05 ± 0.028 (-9.34%)
12	1.32 ± 0.084	- 0.14 ± 0.033 (-10.7%)
16	3.43 ± 0.17	- 0.35 ± 0.069 (-10.3%)

Table 2.1. The initial mass of the agarose gels is shown as m_1. Mass variation on gels due to the water mass loss, is reported as Δm and is calculated as $\Delta m = m_2 - m_1$, where m_1 initial mass of the sample and m_2 is the mass measured after the experimental test.

The effect of water loss was also assessed through the diametrical contraction of the sample during stress-relaxation testing (Figure 2.5.E). When compression is held, pressurized pore fluid slowly leaves the system in the radial direction of the sample while pores within it collapse reducing its volume. When diametrical contraction stops due to this phenomenon, it can be understood as the end of the poromechanics contribution to the energy dissipation. The experimental data recorded dissipated energy after the poroelastic model (Section 2.4) plateaued which increased the difference between the equilibrium forces. Based on this observation, the purely poroelastic computational model was insufficient to explain the behavior of agarose in response to unconfined compression observed during the relaxation stage. However, for lower agarose concentrations, agarose network may become poorly crosslinked (i.e., near the percolation threshold). Arbabi and

Sahimi (1993) concluded that for networks with low connectivity, the capabilities of continuum models may be limited since the affine deformation assumption can no longer be applied[48]. Due to the network's decreased cross-link density, viscoelasticity might not be as dominant in that situation as for higher agarose concentration.

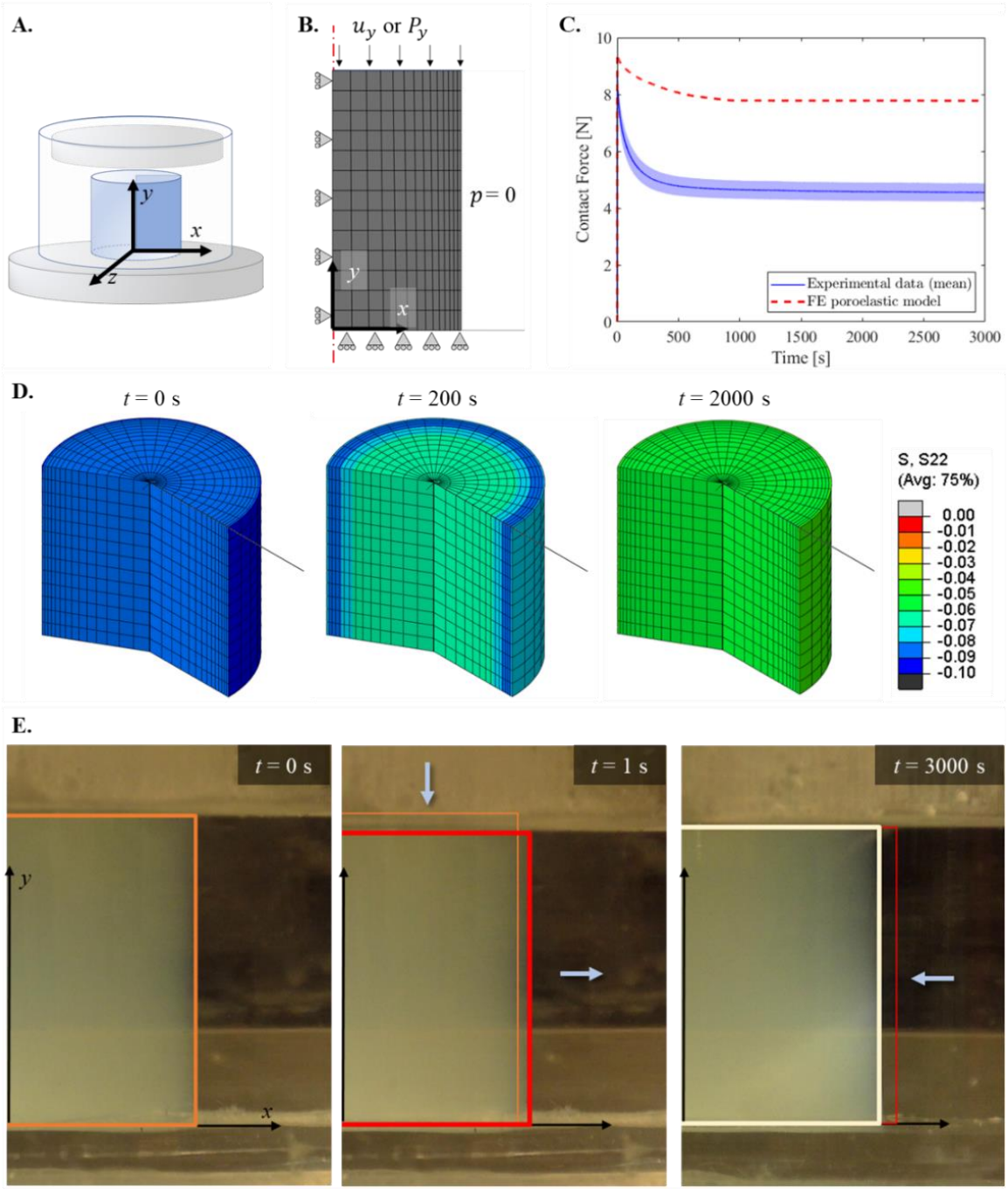

Figure 2.6. **A**. Schematic of unconfined compression of a cylindrical agarose sample. **B**. The computational domain along with the mesh and the boundary conditions implemented. In the boundary conditions, p is the pore pressure and u_y the axial displacement applied when multi-step stress-relaxation is simulated or P_y the axial pressure applied when creep is simulated. **C**. Abaqus poroelastic model prediction results (red dashed line) for stress-relaxation test for 16 mm, 5% w/w agarose gels versus experimental data (solid blue line -average value from the different samples tested- and a blue region -average ± standard deviation). **D.** Three different time frames (from top to bottom, 1 s, 200 s and 2000 s) are plotted to show the stress distribution in the axial direction. It is possible to observe how the poroelastic effect generates a gradient on the stress distribution. After the fluid transport ceased, the stress field became uniform, and the solid network was the only part of the system dissipating energy. **E**. Photographs were taken during stress-relaxation test on 16 mm, 5% w/w agarose gels to experimentally quantify the Poisson's ratio of the solid skeleton and determine the order of magnitude of the characteristic time corresponding to the fluid leaving the system. The compression stage had a duration of 1 s where the gel expanded laterally. The relaxation process was recorded while the gel contracted laterally due to the fluid leaving the system. The gel stopped shrinking at 3000 s after the compression stage.

2.3. AGAROSE AS A NONLINEAR TRANSIENT NETWORK

The time-dependent inelastic response of agarose samples in this study was dominated by viscoelasticity, rather than poroelasticity. In the literature, the mechanical behavior of agarose have generally been characterized by an elastic and a time-dependent or viscous component using phenomenological viscoelastic models[72–74] (i.e., the simplest being the Maxwell model). These models however remain mostly empirical, which motivates the current work as an attempt to build a connection between the gel's network topology and its mechanical response.

2.3.1. Preliminaries: the transient network theory

Let us start by introducing a theoretical framework to describe the nonlinear viscoelasticity of polymer networks, known as the transient network theory (TNT)[10,12]. Due to the presence of physical crosslinks in agarose structure[88], the network is assumed to be dynamic, wherein the polymer chains associate and dissociate over time.

The polymer is thus idealized as a network of polymer strands with the end-to-end vector $\boldsymbol{r}$ which represents as the segment between two nodes or crosslinks. For convenience, we introduce the normalized end-to-end vector $\boldsymbol{\lambda} = r/r_0$ where r_0 is the natural (force-free) length of a strand. In the TNT, a statistical description of the network is provided by the density c of connected strands and the so-called strand conformation tensor, with indices μ_{ij} given by

$$\boldsymbol{\mu}(t) = 3\langle \boldsymbol{\lambda} \otimes \boldsymbol{\lambda} \rangle \tag{2.4}$$

where the operation $\langle\ \rangle$ denotes the average chain deformation of all connected strand within a representative volume element. If the network is initially isotropic, it verifies $\boldsymbol{\mu}(0) = \boldsymbol{I}$. Under the affine deformation assumption[89], the change in stretch of a connected strand verifies $\dot{\boldsymbol{\lambda}} = \boldsymbol{L} \cdot \boldsymbol{\lambda}$ where $\boldsymbol{L}$ is the velocity gradient $\boldsymbol{L} = \dot{\boldsymbol{F}}\boldsymbol{F}^{-1}$. Therefore, it is possible to construct an evolution

equation for the strand conformation tensor if the rates of chain association and dissociation previously described are known[12].

$$\dot{\boldsymbol{\mu}} = \boldsymbol{L\mu} + \boldsymbol{\mu L}^T - k_d\boldsymbol{\mu} + k_a\frac{C-c}{c}\boldsymbol{I} \tag{2.5}$$

where C is the total number of strands per unit volume the network (including both connected and dangling contributions), and k_a and k_d are the kinetic rates describing polymer chains association and dissociation, respectively. For simplicity, we assume there is a perfect bond exchange within the network, meaning each detachment event is immediately followed by an attachment event[90]. We also consider the case of incompressible plastic flow. The evolution equation becomes the following[35]:

$$\dot{\boldsymbol{\mu}} = \boldsymbol{L\mu} + \boldsymbol{\mu L}^T - k_d\left(\boldsymbol{\mu} - \frac{3}{\mathrm{tr}\,\boldsymbol{\mu^{-1}}}\boldsymbol{I}\right) \tag{2.6}$$

From this relation, it is straightforward to show that for a covalently cross-linked network ($k_d = 0$) the conformation tensor $\boldsymbol{\mu}$ is equivalent to the left Cauchy-Green tensor $\boldsymbol{b}$, i.e. $\boldsymbol{\mu} = \boldsymbol{b} = \boldsymbol{FF}^T$[12]. Similarly to Equation 2.3, the true stress tensor can then be derived in terms of the conformation tensor as[10,32]

$$\boldsymbol{\sigma} = \frac{2}{J_e}\boldsymbol{\mu}\frac{\partial\psi}{\partial\boldsymbol{\mu}} = \frac{2}{J_e}c_{10}\mathrm{Dev}\,\bar{\boldsymbol{\mu}} + \frac{2}{D_1}(J_e-1)\boldsymbol{I} \tag{2.7}$$

where the deviatoric part of $\bar{\boldsymbol{\mu}}$ is given by $\mathrm{Dev}\,\bar{\boldsymbol{\mu}} = \bar{\boldsymbol{\mu}} - \frac{\mathrm{tr}\,\bar{\boldsymbol{\mu}}}{3}\boldsymbol{I}$. Material constants c_{10} and D_1 were defined in Equation 2.2.b. This model describes a material that displays a linear elastic response (through its Neo-Hookean form), and a linear viscoelastic response (since the rate constant k_d remains constant). Note that this model may however still capture nonlinear geometrical effects since it is valid for large strains. The viscoelasticity of agarose was however observed to be quite

nonlinear, which motivates the development of a more physical model regarding the relaxation mechanisms occurring within the polymer structure. Such a theoretical improvement must therefore involve a rate constant k_d that changes with stress as previously discussed in Hui *et al.* (2021)[39].

2.3.2. Nonlinear bond dynamics of agarose-based gels

Hydrogen bonding not only governs the self-gelation of agarose gels, but it also facilitates the complex dynamics of the resulting network. Hydrogen-bonding side groups found in agarose facilitate the formation of transient supramolecular structures with viscoelastic responses[21]. It is theorized that there are two main microstructural features that contribute to agarose viscoelastic behavior. First, aligned agarose molecules that form double helices have a limited mobility in comparison with single agarose molecules. This dynamic gel structure has been proposed to occur at short relaxation times. In contrast, agarose molecules present in clusters that are not aligned with each other can dissipate energy much more easily as they slide over adjacent molecules, corresponding to a fluid-like behavior[24]. This behavior is illustrated in Figure 2.6.

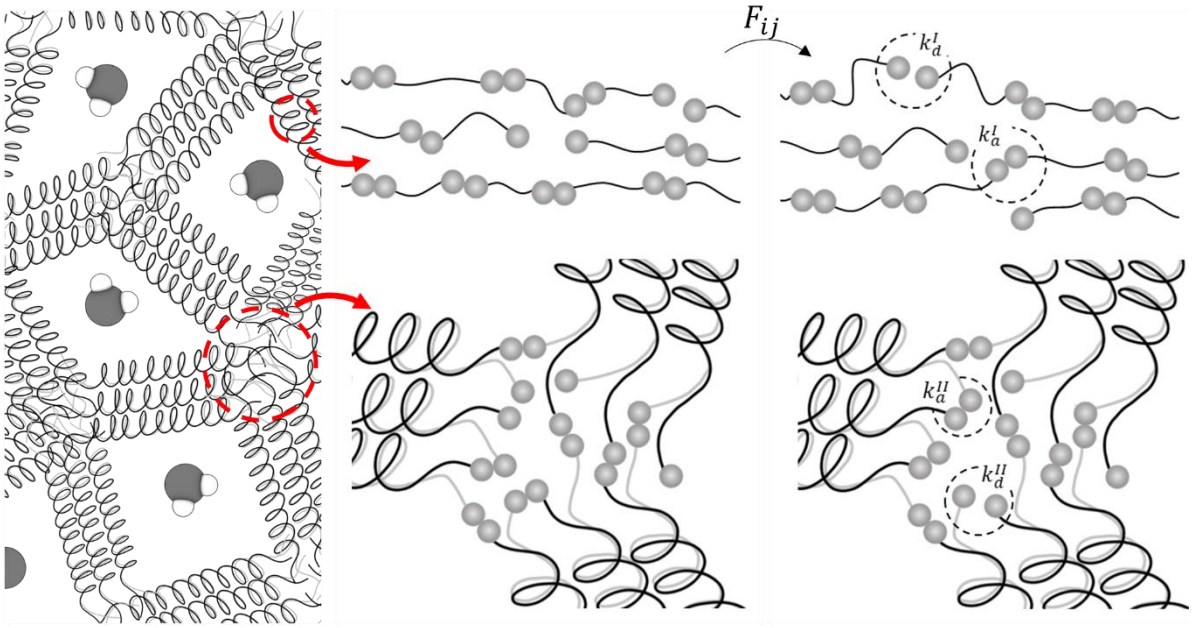

Figure 2.7. Schematic of the short relaxation time on agarose corresponding to the fast bond dynamics (k_d^I and k_a^I) of the strands aligned on the double helices (top) and of the long relaxation times associated to the slow bond dynamics (k_d^{II} and k_a^{II}) where agarose molecules presented in the suprafibers clusters can dissipate energy much more easily as the they slide over adjacent molecules (bottom).

Our experimental results suggest that agarose networks have two different dissipation mechanisms when subjected to an external stress[23]. To construct a model for this network, we first assume each mechanism has its own characteristic dissociation rate such that global the kinetic rate k_d is decomposed as:

$$k_d = k_d^I + k_d^{II} \tag{2.8}$$

Here k_d^I is the fast dissociation rate associated to the rearrangement of the strands aligned forming the double helix structure and k_d^{II} is the slow dissociation rate associated with the bond exchange in the suprafiber junctions. A closer look at experimental data suggests that the transition between

the above two relaxation mechanisms is smooth and a function of the overall stress-state of the specimen. The fast rates k_d^I is assumed to change with the level of stress, or alternatively, the level of elastic deformation while the slow constant k_d^{II} is assumed to remain constant over the time scale of the experiments. For simplicity, we follow classical plasticity theory and assume that volumetric deformation does not affect inelastic flow[91]. This model assumption can easily be relaxed in future implementation of the model if further experiments show it to be inaccurate. We can therefore define a scalar measure of the isochoric elastic deformation via an "effective elastic strain" defined as:

$$\bar{\mu} = \sqrt{\frac{3}{2}\mathrm{Dev}(\boldsymbol{\bar{\mu}}) : \mathrm{Dev}(\boldsymbol{\bar{\mu}})} \ ,$$

such that the fast relaxation rate is defined with a generic function $f(\bar{\mu})$ in the form:

$$k_d^I = k_{d0}^I f(\bar{\mu}) \qquad 2.9$$

The scalar function $f(\bar{\mu})$ need to be derived based on the experimental data collected. Observation of the creep test data suggests that agarose does not show significant creep for $\bar{\mu} < \beta$. However, for values of $\bar{\mu} > \beta$ (Figure 2.8.A), creep suddenly accelerates and the function k_d^I maybe assumed to follow the relation $k_d^I = k_d^0 \exp(\gamma\bar{\mu})$. This exponential relation is in line with the theoretical model presented by Eyring experiencing force-dependent bond dynamics[49,92,93]. Combining this statement along with the observation made from multi-step stress relaxation tests, the evolution of k_d is hypothesized to follow a generalized logistic function with the following expression:

$$f(\bar{\mu}) = \frac{e^{\gamma\bar{\mu}}}{1 + e^{-\alpha(\bar{\mu}-\beta)}} \qquad 2.10$$

where β represents the elastic strain trigger for bond dynamics, and γ is defined as the stress-sensitivity of bond dynamics. In addition, as depicted in Figure 2.7, coefficient α describes the sharpness of the transition between the two energy dissipation mechanisms; if $\alpha \to \infty$, the transition is very steep and converges to a step function while $\alpha \to 0$ indicates a very smooth transition showing a perfect coupling between the two relaxation mechanisms during the whole relaxation process. The coefficient β follows the evolution of the equilibrium or plateau stress σ_p point seen in Figure 2.2.C-D-E.

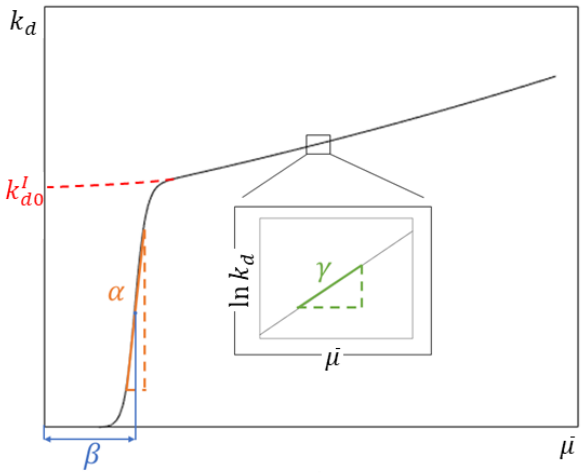

Figure 2.8. Physical interpretation of the fitting parameters used to describe the bond dynamic evolution: α is the bond dynamics transition steepness, β is the elastic strain trigger for bond dynamics, γ is the stress-sensitivity of bond dynamics and k_{d0}^I is the spontaneous dissociation once the stress threshold is triggered.

2.3.3. Implementation and experimental validation

The above viscoelastic model was implemented into a UMAT Abaqus subroutine requiring the calculation of the Cauchy stress $\boldsymbol{\sigma}(\bar{\boldsymbol{\mu}})$ and tangent stiffness matrix $\boldsymbol{C}(\bar{\boldsymbol{\mu}})$. Using expressions provided in Appendix II, Equation 2.6 was invoked to enforce the evolution of the conformation

tensor as a function of the dissociation ratio of the network. To summarize, the material behavior of the hydrogel depends on two physical processes that are captured by (a) a UMAT subroutine for the solid matrix based on the TNT to control the viscoelasticity of the skeleton, and (b) an Abaqus material library to describe the poroelasticity due to the pore fluid flow of the solvent.

Running the optimization procedure detailed on Appendix III on the creep data and, separately, on the multi-step stress-relaxation data, it was further possible to accurate calculate model parameters α, β, γ and k_{d0}^{I}. Using data from the creep test, it was further possible to accurate calculate the exponential evolution of k_d^I where, independently of the concentration of agarose used, we found mean values of $k_{d0}^{I} = 0.001164$ 1/s and $\gamma = 2.412$ (Figure 2.8.A); this expression accurately predicts the values for k_d^I when $\bar{\mu} < \beta$.

Using data from the multi-step stress-relaxation and our optimization algorithm, the parameters α and β were empirically fitted for various agarose composition and applied strain (see Figure 2.8.B). Different initial guess values were used as an input to the optimization algorithm.

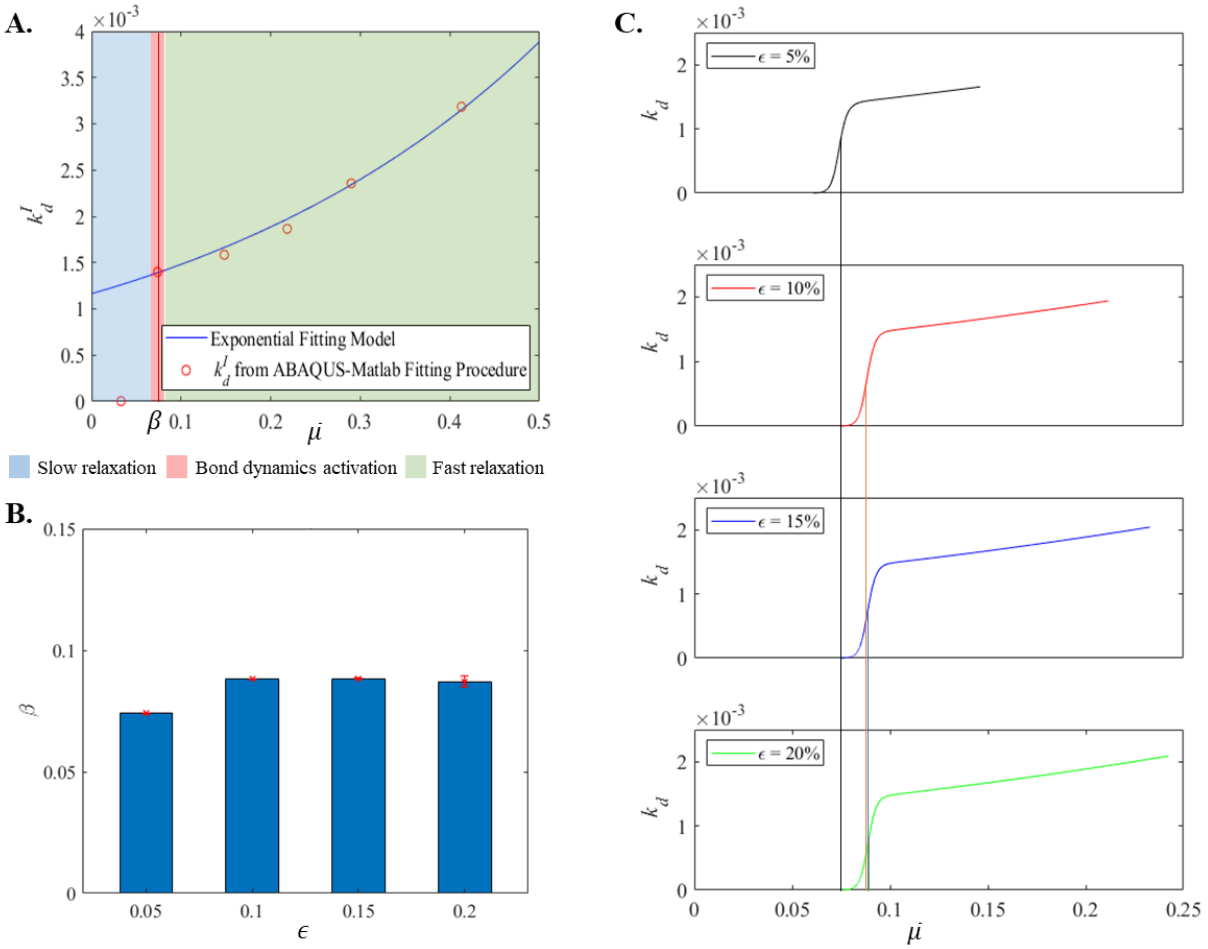

Figure 2.9. A. Dissociation rate exponential evolution obtained from the optimization algorithm ran on the experimental creep test data on 12 mm, 5% w/w agarose gels. Graphing the results shows three different zones: slow relaxation domain (blue zone), fast relaxation domain (green zone) and the elastic strain trigger, β, zone for bond dynamic activation (red zone). **B.** For $\alpha = 500$, average values for the different agarose concentrations of the evolution of the elastic strain trigger for bond dynamics β at different applied strains during the multi-step unconfined compression test. **C.** For 10% w/w agarose, evolution of the bond exchange rate as a function of $\bar{\mu}$. Vertical lines represent the values for the bond dynamic trigger parameter β.

This data suggests that while the sharpness of the bond dynamics transition remains constant across the multiple compression steps, the elastic strain trigger, β, changes its values to account for the stress plateauing during the whole test (Figure 2.8.B). Therefore, β follows the plateau point evolution. For the 5% w/w case, β decreases for the last stress-relaxation step. This agrees with the experimental data of Figure 2.2.C where the plateau stress σ_p measured in the last compression step (20% strain), is below the one measured for 15% strain. For 7.5% and 10% w/w agarose, the same fitting parameter were used for strains > 5%. In these cases, the sharpness of the transition remains constant, but β slightly increases its value at each deformation step. Taken together, these results suggest that the evolution of bond dynamics is independent of agarose concentration.

The dissociation constant k_d^{II} of the cluster was obtained using the optimization algorithm. We found that k_d^{II} is generally insensitive to stress and agarose concentration which confirms it can be kept constant. We estimated the mean rate constant as $k_d^{II} = 2.76\text{E-}6$ 1/s (i.e., $k_d^{II} \ll k_d^I$). In the remainder of our analysis (i.e., that concentrates on shorter time scales), this rate can therefore be neglected compared to k_d^I, and a general evolution equation for the general kinetic rate is $k_d \approx k_d^I = k_{d0}^I f(\bar{\mu})$. Therefore, as an input for the UMAT subroutine five parameters are necessary to describe the solid matrix behavior: the elastic modulus E_s of the solid network, Poisson's ratio ν_s of the solid matrix and the empirical variables α, β, γ and k_{d0}^I.

Figure 2.9. demonstrates agreement between the poroviscoelastic model and the time-dependent mechanical response of agarose gels during experimental creep (5% w/w agarose) and multi-step stress relaxation (5, 7.5, 10% w/w agarose) testing. Figure 2.8.B. and Figure 2.9.B-D. also verify the evolution of bond exchange rate behaves independently of agarose concentration. Inset plot in panel A in Figure 2.9 corroborates the model captures the three creep regimes (primary, secondary and tertiary creep) in experimental data. Insets plots in panels B-D in Figure 2.9, shows the model

captures the short-term experimental response of agarose gels. We notice energy is dissipated faster on the experimental data than on the computational model for short time scales, yet such difference does not affect the equilibrium response.

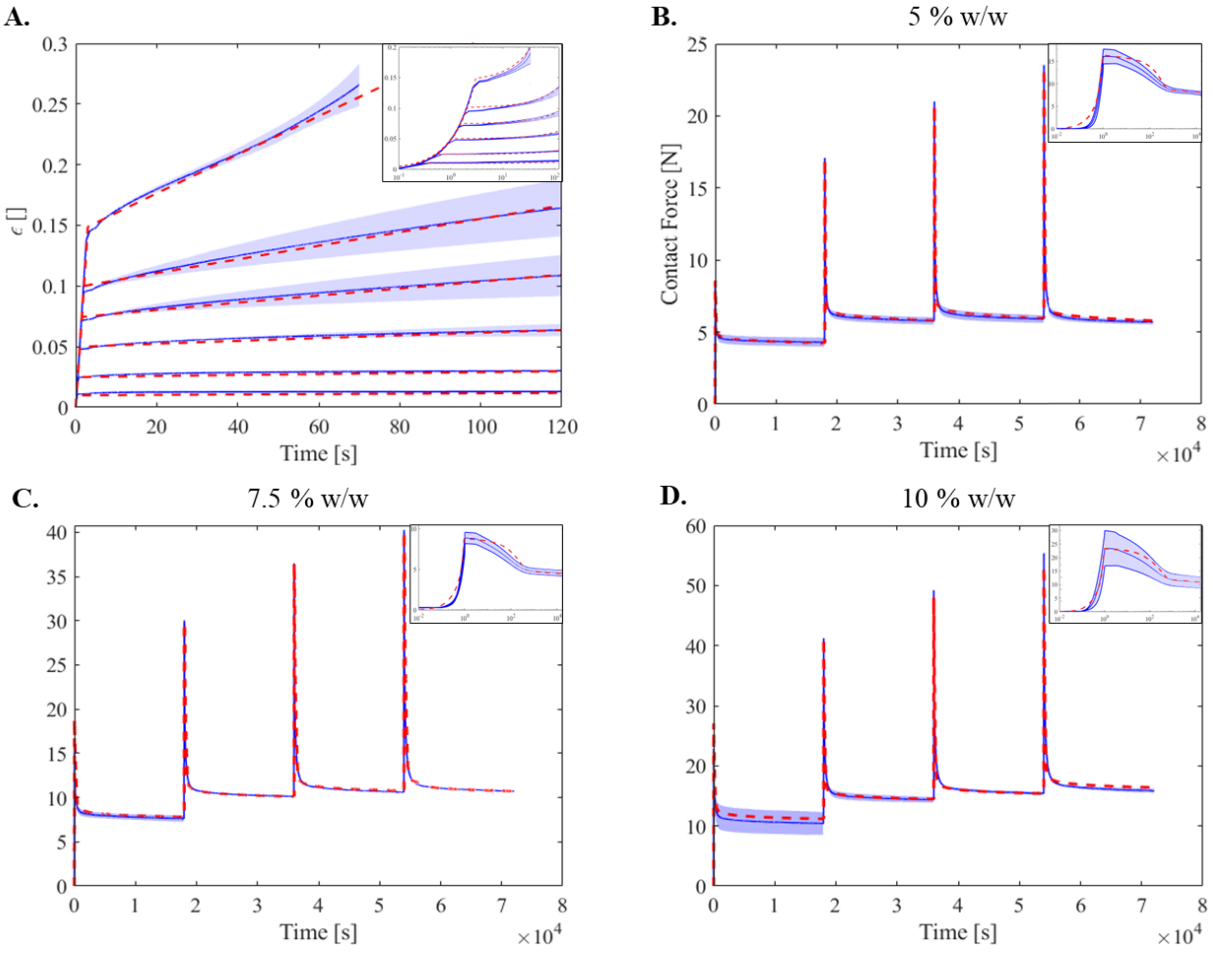

Figure 2.10. Comparison of the prediction from finite element predictions against experimental measurements for tested samples. Abaqus simulation results are represented by red dotted line, and experimental results are reported as a blue solid line (mean values from experimental tests) and blue region (average ± standard deviation). **A.** Results of creep test for 12mm, 5% w/w agarose gels. The inset in **A**. shows creep test results in a semilogarithmic scale along the x-axis. **B.**, **C.**, and **D**. Results of multi-step stress relaxation tests for 5%, 7.5% and 10% w/w agarose

gels respectively. The inset in **B-D**. shows the stress evolution for the first loading and relaxation step in a semilogarithmic scale along the x-axis.

2.4. DISCUSSION

We developed a physically based model to describe and predict the time-dependent behavior of agarose networks under unconfined compression. Unlike prior phenomenological and continuum models describing viscoelasticity, our approach considers the time-dependent evolution of the stress-dependent variables that result from bond-exchange within the polymer network. This work provides a reinterpretation of agarose network viscoelastic behavior using the transient network theory (TNT). Using the characterization of the two main microstructural features that contribute to agarose viscoelastic behavior, which are based on dissociation and reassociation of molecular bonds within agarose, we demonstrated that the network deforms over time through non-linear force-dependent evolution of bond dynamics.

Agarose gels are formed from hydrogen (e.g., dynamic) bonds that re-attach after disengaging which imparts gels with viscoelastic behavior. Here, viscoelasticity was assumed to follow the two main characteristic microstructures of the gel network described by Labropoulos *et al.* (2001)[23]. Assuming perfect bond exchange, we hypothesized that the overall dissociation rate (k_d) results from a linear combination of the dissociation rate corresponding to double helices forming between aligned agarose molecules (k_d^I) and the dissociation rate of the agarose molecules present in the clusters (k_d^{II}). Due to the degree of mobility of the agarose, these factors are responsible for the short ($1/k_d^I$) and longer ($1/k_d^{II}$) relaxation times, respectively. The present work incorporated these topologically based phenomena into a mathematical model, the TNT, thus enabling a novel quantitative understanding of the relationships between molecular physics and overall mechanical response. This methodology may be extrapolated to other biopolymer networks with similar topologies (i.e., collagen and fibrin networks) to predict their emerging material response as a function of bond kinetics.

The fast bond dynamics of agarose network (k_d^I) associated to the aligned agarose molecules exhibited significant force-sensitive dynamics. In the creep test, we observed that the magnitude of the applied stress had the effect of weakening the solid-like behavior of the network associated to the fast energy dissipation mechanism. We interpreted this behavior as a reorientation of the agarose network along the direction of applied compression which is a particular property of semiflexible networks. Our model suggested an exponential force-dependent response of the fast dissociation rate, which agrees with Eyring's theory[92]. Capturing this phenomenon revealed a novel insight in agarose viscoelastic properties: i.e., the lifetime of a bond depends on the force applied to that bond.

We further demonstrated the non-linear viscoelasticity of agarose hydrogels throughout the implementation of a non-constant dissociation rate. In our study, the nonlinear viscoelasticity could be observed by a stress-plateauing effect during a multi-step stress relaxation test. In particular, the equilibrium stress at the end of the relaxation phase plateaued and reached the same value independent of the applied deformation. We developed a master equation to describe the bond exchange (Equation 2.10) based on physics-based parameters such as the elastic strain trigger for bond dynamics and the stress-sensitivity of the bond rate. The same behavior was observed in multi-step stress relaxation testing (with a 30 minute relaxation period) reported by Roberts *et al.* (2011)[66] in their comparative study of the viscoelastic mechanical behavior of agarose and poly(ethylene glycol) hydrogels. Because of the relatively short time used between step strains in their study, the stress did not plateau as reported herein; however, the trends in both studies are consistent.

Following the stability of adhesion clusters model presented by Erdmann and Schwarz (2004)[94], we hypothesized that the clusters formed by several suprafibers within agarose networks increased

the number of connected bonds during the deformation process (Figure 2.10). Cluster adhesion was presented in previous literature as a likely mechanism for stress relaxation in biopolymers[95–97]. For example, Prechtel *et al.* (2002) studied cluster dissociation under a linear ramp of force and described the strength of the adhesion of living cells to model membranes[98]. Briefly, Erdmann and Schwarz postulated a detailed theoretical analysis of the stochastic dynamics of a cluster of parallel bonds under shared constant loading and with rebinding. The adjacent agarose molecules that are not part of the cluster in a stress-free configuration may be available to later form new crosslinks with the initial components of the cluster. This theory provides a mechanism for increasing cluster size and strengthening of the network. Following this theory, we found the elastic modulus of agarose slightly increased with elastic deformation which indicated a mild strain stiffening effect during sustained compression (Appendix IV). Future investigations should further evaluate our hypothesis for a potential relationship between the elastic strain trigger for bond dynamics and cluster size and should also consider other possible competing mechanisms such a viscoelastic elongation of the network chains[99,100].

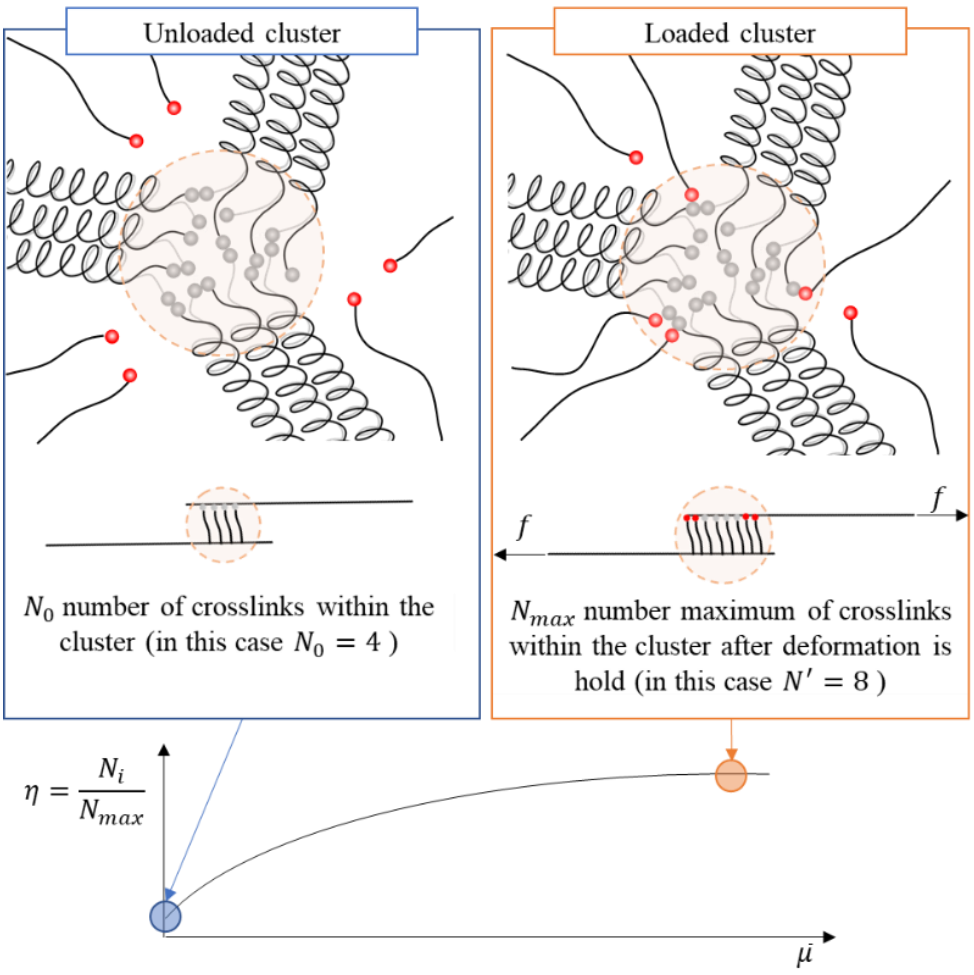

Figure 2.10. Schematic representation of the number of bonds N_i within a cluster in agarose network before and after a stress field is applied. Unbonded agarose molecules join the cluster as the external force increases. Variable η is defined to represent the cluster bond saturation plateauing after the force f held by the cluster exceed a certain threshold value.

Poromechanical effects in agarose did not significantly contribute to energy dissipation during stress-relaxation. These results followed the well-studied poroelastic material behavior of agarose in the literature[86,101–105]. We observed that the influence of time-dependent fluid displacement on the gel's response to be small. However, we still incorporated it in our analysis for the following reasons. First, we observed a reduction of the initial hydrogel mass during long-duration

compression tests; this effect can only be captured by poromechanics. Second, the incorporation of fluid transport during loading allowed for a more general formulation that may explain coupling of poromechanics with network relaxation; this point can be used to better understand poroviscoelastic behavior of agarose gels. Demonstrating the minor role of poromechanics in agarose supported the use of the TNT to control and predict the macroscopical time-dependent response of physically crosslinked gels.

Unlike prior applications of the TNT in 2D[10], our study demonstrated the application of the TNT into a commercial FEA software. This approach will allow for future 3D modeling of complex polymer behavior (i.e., crack propagation or cavity generation[106]) using an underlying mechanism-based material model. We also demonstrated an initial step that will enable a continuum approach of the TNT to be applied to more complex geometries (i.e., 3D printed hydrogels) than the cylindrical geometry presented in this study. The computational implementation of the TNT into a commercial FEA package, combined with experimental testing, allowed us to assess the influence of poroelastic and viscoelastic effects in the overall macroscopic response of agarose to time-dependent experiments.

Finally, we emphasize that the model presented in this study can be used to provide control guidance on the material design in numerous applications, many of which are applicable to bioengineering, that necessitate the use of agarose and similar gels. The TNT model also offers the possibility to design and fabricate gels based on their bond dynamic to obtain a specific time-sensitive behavior. One important future effort is to extend the current model to different biopolymers with similar network topology and to determine if the TNT can be universally applied to describe behavior of similar biopolymers. Finally, our work may also support a variety of tissue engineering applications and provide physical insights to understand the force-dependent

viscoelastic behavior. For instance, understanding how the yielding behavior of agarose gels may be crucial for a wide range of biomedical applications where gels are subjected to loads over long periods of time.

CHAPTER 3:

TIME-DEPENDENT MECHANICS OF DYNAMICALLY CROSS-LINKED SEMI-FLEXIBLE NETWORKS

Semi-flexible networks, which are essential backbones within most soft connective tissues, exhibit unique mechanical properties including non-linear elastic responses, viscoelasticity and self-healing. Moreover, these networks are commonly remodeled through processes that are mediated cells[107]. The diverse mechanical responses observed in these networks make developing a general theoretical framework challenging. Within the intracellular milieu and extracellular matrix, filaments are generally significantly longer than the flexible cross-linkers ($R > 1$). Examples include biopolymers like actin networks and fibrillar proteins including collagen type I, respectively. We thus developed a physically based mesoscale model for semi-flexible networks to study time-dependent response and plastic deformation, and we proposed bond dynamics as a novel mechanism for describing strain-stiffening and viscoelastic behavior. The primary objective of this work was to better understand the time-dependent mechanics of semi-flexible networks, which can inform their design and be extended to other biopolymers with similar network topology. The model successfully replicated the Gasser, Ogden, and Holzapfel (GOH) continuum stress-stretch approximation for networks with permanent bonds, validating the applicability of this approach for biopolymer networks. We found that network orientation and Weissenberg number significantly impact the mechanical response and network reconfiguration of semi-flexible networks with dynamic bonds. Holding time during stress-relaxation was found to be a crucial factor affecting stress evolution and plastic realignment in networks with bond dynamics. Our study offers a comprehensive understanding of the mechanical response and network reconfiguration of semi-flexible networks with permanent and transient cross-links. This work also

provides valuable insights into the interplay between microscopic structure and macroscopic mechanical properties, paving the way for future research in optimizing and controlling mechanical properties of these networks for various applications.

3.1. INTRODUCTION

Semi-flexible networks constitute most of the soft connective tissue across several length-scales. Their characteristic nonlinear elastic response has been the object of many studies from both theoretical and experimental side. These models couple fiber realignment and the associated stress-stiffening, often defined by a *J*-shaped stress-strain curve[108,109]. A less studied signature of semi-flexible biological networks is their viscoelastic response, self-healing, and remodeling over long time scales. These networks often possess dynamic cross-links that can associate and dissociate, giving them the ability to reconfigure over time[13].

Introducing a general theoretical framework for this variety of networks is tempting but may be challenging due to the diversity of response that can be observed depending on the network topology. One of the parameters that significantly affects the network response if the ratio R of filament to cross-linker's length. Thus, when the flexible cross-linkers are long compared to the filaments ($R < 1$), the former dominate the network response. In this case, the time-dependent response is accurately captured by model such as that introduced by Hui et coworkers[110] and more recently by the transient network theory[12,32]. In this case, the stress relaxes over time, but filament alignment remains insignificant to the response due to their small size. When the filaments are on the order of the cross-linkers size ($R \approx 1$), several non-trivial nonlinear effects arise from the mechanical coupling between filaments rotation and cross-linkers' stretch. Theoretically, a first model was introduced by Sridhar and Vernerey (2020)[111] to understand the mechanics of transient nematic networks, for which rods are strongly aligned and are assumed to rotate with the surrounding continuum. More recently, this approach was generalized to capture independent rod rotation and the associated effects including soft elasticity and the strain stiffening from rod realignment. Mathematically, the addition of independent degrees of freedom unfortunately brings

significant difficulties in the derivation of simple solutions, despite its ability to describe a rich spectrum of responses.

In the present work, we consider the case of a dynamic semi-flexible network in which filaments are significantly longer than the flexible cross-linkers (i.e., $R > 1$). In this case, the response is expected to be dominated by the filaments' elasticity and realignment, while the role of dynamic cross-links consists in relaxing the mechanical constraints between adjacent filaments over time. The case $R > 1$ is of particular importance for a variety of biopolymers such as actin networks cross-linked by filamin, spectrin and other proteins in the cytoskeleton of most mammalian cells[112,113]. Collagen type I is a viscoelastic semi-flexible, and it is the main structural protein within the extracellular matrix (ECM)[114–118].

As other semi-flexible networks, collagen has been shown to have a stiffening response to strain that is expected to affect cellular responses[119,120]. While some studies reported entropic elasticity of individual polymers resisting extension[121] is what causes the strain-stiffening in these networks, other studies suggest it is caused by the alignment of fibers in the direction of the applied load[122,123]. According to Nam et al. (2016)[124], the strain stiffening of collagen matrices relates to their viscous behavior independently of the strain-stiffening underlying mechanism. At larger deformations, these matrices stiffen significantly but subsequently, the strain stiffening gradually decreases over time due to strain-enhanced stress relaxation. Guidry et al. (1987)[125] suggested that contracted gels are stabilized by the formation of non-covalent bonds between the nearby collagen fibers preventing the full elastic recovery of the network deformation as the external load is removed. Even plastic deformation of collagen networks has been shown in the literature[126–128]; yet, compared to elasticity and viscoelasticity, it is still largely unexplored.

The mechanical properties of hierarchical semi-flexible materials ranging from individual molecules to large-scale macroscopic connective tissues have received significant attention[129,130]. Relating the local properties and topologies of such networks to their global mechanical response is highly sought after by researchers aiming to elucidate the origins of biophysical phenomena. For example, Buehler (2006)[131] used full atomistic calculations to predict the mechanical properties of tropocollagen molecules under different types of mechanical loading. The main limitation of atomistic models is the enormous number of degrees of freedom that would be required for an all-atom simulation of a collagen fibril. Their elevated computational cost makes atomistic models impractical for modelling statistically representative volume elements (RVEs) that describe the macroscopic behavior. By analyzing the relaxation time distribution spectrum obtained from stress relaxation tests, Xu et al. (2013)[132] were able to explain the macroscopic viscoelastic behavior of collagen matrices, which likely corresponds to relaxation mechanisms involving fiber, inter-fibril, and fibril sliding. Unfortunately, because continuum models frequently include smoothing assumptions, researchers are restricted from examining the influence of local heterogeneities or microstructural characteristics.

To overcome these limitations, mesoscale (or coarse-grained) models are used. Briefly, mesoscale models are molecular simulations model where atoms and chains are transformed into a smaller number of chemical sites reducing the complexity of the problem with respect the atomic model while keeping essential interactions for concerned properties. The mesoscale model proves necessary for the exploration of localized stochastic events, such as variability of the bond kinetics, or the nucleation of micro-cavities that likely conceive damage and fracture. Tang et al. (2009)[133] investigated the mechanical behavior of initially flawless finite size collagen fibrils exposed to uniaxial strain using coarse-grained molecular dynamics simulations and concluded that

deformation mechanisms, associated with rupture and sliding of tropocollagen molecules, were strongly influenced by fibril length, width, and cross-linking density. A natural extension of such work is to then apply mesoscale modeling in the exploration of dynamic networks and capture the formation and breaking of bonds along collagen fibers. Sight et al. (2020)[55] used traditional methods of molecular dynamics-Monte Carlo simulations to model the dynamic cross-linking reactions during thermomechanical loading and Wagner et al. (2021)[134] developed novel methodology for predicting the mechanical response of sol-gel mixtures using mesoscale modelling. Despite this progress, those methodologies are limited to 2-D problems due to their elevated computational costs and do not include the enthalpic bending contribution since the cross-links are modeled as freely attached pin joints.

In this work, we developed a mesoscopic model for semi-flexible networks to study the time dependent response and the mechanisms of plastic deformation of cross-linked fibrous materials using physically based mathematical models. We propose bond dynamics as a novel mechanism for describing strain-stiffening and viscoelastic material behavior of these systems. With this model we sought to better understand the time-dependent mechanics of semi-flexible networks to inform their design and to provide a framework that may be extended to a range of biopolymers which share similar network topology.

3.2. CONSTITUTIVE RELATION FOR SEMI-FLEXIBLE NETWORKS

To motivate the form of the constitutive relations for the continuum model, we begin by considering the network-level behavior of a semi-flexible material. A variety of these systems exist in the form of biological networks found in the cell cortex[135], arterial wall tissue[131], and blood clots[136]. In such biological systems, a variety of chemical and biological interactions may be at play due to the presence of various enzymes and proteins. We considered a simplified view of a semi-flexible network consisting of a collection of long fibers connected by relatively small cross-links (Figure 3.1.A). In this context, a fiber was considered long if its persistence length l_p is much greater than the length of a cross-link. Furthermore, the cross-links may be static or dynamic, but were assumed to be much stiffer than the fibers and thus act as rigid inter-fiber connections.

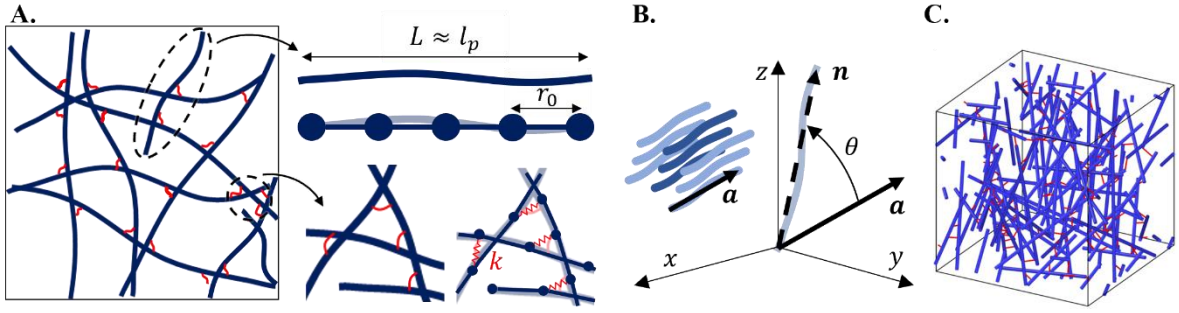

Figure 3.1. A. Schematic of the semi-flexible dynamic networks considered in this work, composed of rigid rods (blue) cross-linked by flexible cross-linkers (red). Discretization of each of the rods in N smaller segments of length r_0. Each of the junctions are the particles of our system. **B**. Characterization of an arbitrary unit vector $\boldsymbol{n}$ as a function of its angle θ from the vector director $\boldsymbol{a}$. **C**. Visualization of the discrete network model generated to describe an isotropic semi-flexible network.

3.2.1. Discrete model for semi-flexible networks

To probe the network-level response of this system, we designed a series of explicit simulations to model semi-flexible networks at a coarse-grained scale. To model the fibers, we discretized them into N segments with initial length r_0 such that the total initial length of the fiber was $L = Nr_0$ (Figure 3.1.A). An orientation vector $\boldsymbol{n}$ is assigned to each fiber, which was defined as the unit vector connecting the first segment to the last. To ensure that the response of the system reflects a semi-flexible network, we maintained the length of the fiber to be close to its persistence length, i.e., $L \approx l_p$. For this study, we maintained each segment in a filament to be aligned and consider the only mode of deformation to be stretching the rod along $\boldsymbol{n}$.

To initialize the network, we randomly placed filaments into a periodic cubic domain of edge length $D \gg L$. As is standard for biological filament networks such as collagen, we considered a transversely isotropic distribution of filament orientations about an arbitrary director $\boldsymbol{a}$ such that the orientation $\boldsymbol{n}$ of the fiber is only a function of its angle θ from $\boldsymbol{a}$ (Figure 3.1.B). As considered by Gasser et al (2006)[137], the distribution function of θ in the network is governed by the π-periodic *von Mises* distribution:

$$\rho(\theta) = 4\sqrt{\frac{b}{2\pi}}\frac{exp[b(cos(2\theta)+1)]}{\text{erfi}\left(\sqrt{2b}\right)}, \tag{3.11}$$

where $b > 0$ is a concentration parameter dictating alignment and $\text{erfi}(x) = -i\text{erf}(x)$ denotes the imaginary error function. As discussed in Gasser et al (2006)[137], we noted that b may be implicitly related to the alignment parameter κ. To ensure a dense packing of filaments, we assigned a minimum overlap distance $\delta \approx l_p$, which is the smallest distance allowed between any two filaments in the network. The filament procedure then goes as follows: (i) a random center point

is chosen anywhere inside the domain, (ii) a random filament orientation θ is sampled from the distribution in Eq. 3.11, (iii) the distance between the attempted filament and every other filament is calculated, if the minimum distance is less than δ, then placement was successful. This procedure continues until 100 subsequent failed placement attempts occur, which means that the system can no longer hold any filaments (Figure 3.1.C).

After the network was created, we considered the motion of the nodes after applying a perturbation. Before defining the equations of motion, we first defined the constitutive behavior of the segments that form each discretized filament. The worm-like chain model is commonly used to model the response of semi-flexible polymers whose persistence length is close to the contour length of the filament[138]. Here, we consider the Blundell-Terentjev elastic energy functional[139], such that the energy ψ_c stored in a filament is

$$\psi_b(\hat{r}) = k_b T \left[\frac{\pi}{2} \frac{l_p}{L} (1 - \hat{r}^2) + \frac{2}{\pi} \frac{L}{l_p} \frac{1}{(1 - \hat{r}^2)} \right], \tag{3.12}$$

where $k_b T$ is the thermal energy scale, L is the contour length of the filament, and $\hat{r} = r/L$ is the normalized end-to-end distance of the chain. Thus, the constitutive behavior of each discretized segment is assigned such that the full chain obeys this energy potential. Specifically, we set the contour length and persistence length of each segment to be proportional to the number of segments per filament and the overall magnitudes of L and l_p of each filament. Therefore, if a filament with $L = l_p$ = 10 is discretized into N = 10 segments, each segment will have a contour length and persistence length of 1.

In the discrete model, the energy potential in Eq. 3.12 defines a force $\boldsymbol{f_b} = \partial \psi_b / \partial \boldsymbol{r}$ acting on each node in the network. The force-extension and stored energy based on the Blundell-Terentjev

model were added to LAMMPS (Large-scale Atomic/Molecular Massively Parallel Simulator)[140] as a bond interaction between pairs of segment junctions. To verify the accurate implementation of the force-extension expression, a single filament model with a different number of segments was generated and subjected to axial loading. Independently of the number of segments used in the filament, the simulation results in filament axial force agreed with the analytical solution.

When the network was perturbed, we used an explicit Brownian integration scheme to evolve the nodes according to the net force acting on them. Further details will be discussed in Chapter 4. For this study, we considered the quasi-equilibrium response of the network such that the network was evolved until the maximum force acting on any node was below a threshold minimum.

3.2.2. Hyperelastic continuum model

We examined the model's ability to replicate the continuum stress-stretch approximation described by Gasser, Ogden and Holzapfel (GOH)[141] for its relevance to biological solids. The Helmoltz free energy function for a quasi-incompressible network is then written:

$$\psi_{GOH}(\bar{E}, J) = \frac{1}{2}c(\bar{I}_1 - 3) + \frac{k_1}{2k_2}[\exp(k_2\bar{E}^2) - 1] + \frac{K}{2}(J-1)^2 \qquad 3.13$$

where, $\bar{I}_1 = \mathrm{tr}\,\overline{\boldsymbol{C}}$ denote the first invariant of the symmetric modified right Cauchy–Green tensor $\overline{\boldsymbol{C}}$, c is the neo-Hookean parameter, $\bar{E}$ is the Green-Lagrange strain-like quantity which characterizes the strain in the direction of the mean orientation $\boldsymbol{a_0}$, $k_2 > 0$ is a dimensionless parameter and $k_1 > 0$ is a stress-like parameter to be determined from mechanical tests, and K can be interpreted as a bulk modulus that penalizes deviations of the volumetric stretch ratio $J = \det \boldsymbol{F}$ from unity. The Green-Lagrange strain-like quantity is defined as

$$\bar{E} = \kappa \bar{I}_1 + (1 - 3\kappa)\bar{I}_4 - 1 \qquad 3.14$$

where $\bar{I}_4 = \boldsymbol{a_0} \otimes \boldsymbol{a_0} : \overline{\boldsymbol{C}}$ is the fourth invariants of the symmetric modified right Cauchy–Green tensor $\overline{\boldsymbol{C}}$. For the case κ = 0, the network is isotropic while when 0 < κ < 1, the networks are anisotropic. In particular, the case κ = 1 corresponds to a fully aligned fibrous network, such as found in tendons and other strongly aligned connective tissues.

This allowed us to express the symmetric Cauchy stress tensor as:

$$\boldsymbol{\sigma}_{GOH} = \frac{2}{J}\left[\frac{\partial \psi}{\partial I_1}\boldsymbol{b} + I_4 \frac{\partial \psi}{\partial I_4}\boldsymbol{a_0} \otimes \boldsymbol{a_0}\right] + \frac{\partial \psi}{\partial J}\boldsymbol{I} \qquad 3.15$$

where $\boldsymbol{b}$ is left Cauchy–Green tensors. To examine the discrete model's ability to replicate the continuum stress-stretch approximation described by the GOH model, five different networks were formed utilizing the approach detailed in Section 3.1. Harmonic cross-links were established to connect distinct filaments with an initial length of less or equal than a threshold distance. The number of filaments and cross-links per unit volume was kept constant while varying κ over five values between 1/3 and 0. Figure 3.2.A illustrates for κ = 1/3, 1/6 and 0, that the discrete model generated in LAMMPS accurately captured the mechanical response of the GOH model.

This study revealed the impact of the network orientation parameter κ on the GOH characteristic parameters k_1 and k_2. Figure. 3.2.B demonstrates that as the network becomes more isotropic ($\kappa \rightarrow$ 1/3), k_1 and k_2 increase exponentially. Both parameters have been normalized for better comparison. Moreover, the analysis also revealed that increasing the number of fibers and cross-links per unit volume leads to higher k_1 values for each κ value, while k_2 appears to be independent of the number of fibers and cross-links per unit volume (Figure 3.3 C). Defining the fiber volume fraction as $\rho = N^F L/V$, where N^F is the number of fibers, L is the length of the fibers and V is the

total volume of the network; then, for a constant value of alignment κ, the expression $k_1 = \rho k_1^0$ can be deduced, where k_1^0 is a stress-like constant parameter.

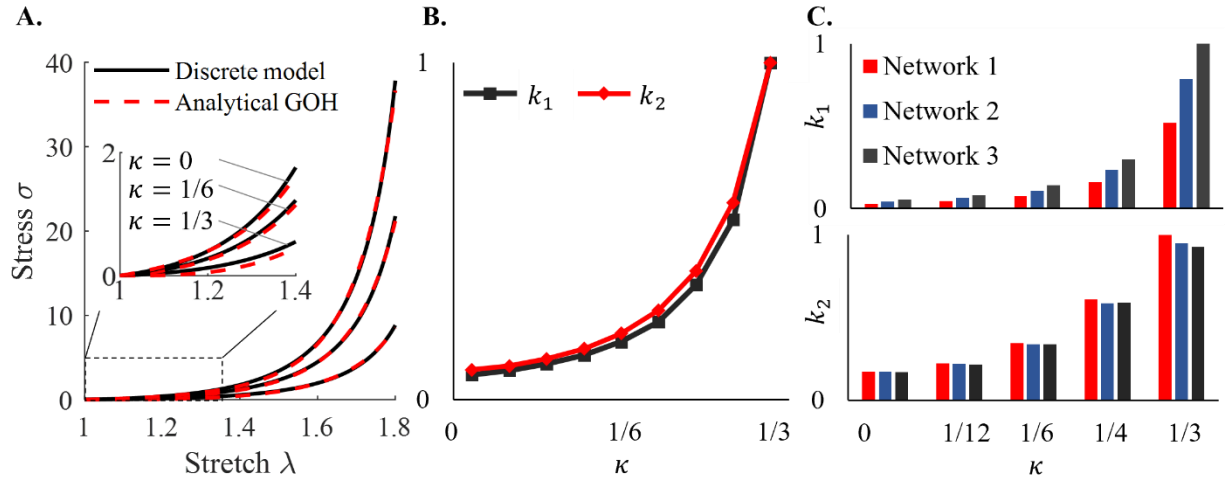

Figure 3.2. Validation of the discrete model. **A**. Comparison between stress-strain evolution obtained from the GOH analytical solution (dotted red lines) and the discrete model (solid black lines) for three different alignment degrees of the network κ. **B**. Evolution of GOH parameters k_1 and k_2 as a function of κ. **C**. Compression between the evolution of k_1 and k_2 as a function of κ for a network with 562 (*Network 1*), 782 (*Network 2*) and 983 (*Network 3*) filaments.

3.3. TIME-DEPENDENT RESPONSE IN SEMI-FLEXIBLE NETWORKS

Our main interest in this study was to understand the time-dependent response and evolution of a semi-flexible network when the cross-linking junctions between elastic filaments are dynamic. The word *dynamic* here refers to the case where junctions have the ability to temporally break and later reform between either different, or the same filaments, but at various locations along their length. The way in which these events occur is stochastic and may be influenced by a variety of factors, such as chemistry, temperature, and mechanical forces. In this work, our objective was to consider perhaps the simplest situation, where these events occurred at a mean frequency, denoted as k_d (for rate of detachment). We further assumed that a detachment event was quickly followed by an attachment event so that we did not need to consider eventual competition between the attachment and detachment rates.

To examine the time-dependent response of the discrete network, we considered the same discretized fiber system as before, but now allowed cross-links to be created and destroyed dynamically. We described creation and deletion events by their characteristic timescales, k_a and k_d respectively, which have units of inverse seconds. Briefly, the stochastic deletion procedure is as follows: first, at a numerical time t, all nodes within a cutoff are considered as potential bonding partners. If detachment events are uncorrelated, the probability of a successful deletion event is $P = 1 - \exp(-k_d t)$, where t is the size of the numerical timestep. For each potential event, a random number is generated and compared to its probability of detachment. If the deletion is successful, the cross-link is removed. The creation procedure is identical and occurs simultaneously within the system. Finally, we noted that after every timestep on which we allowed for bond dynamics, we equilibrated the system to comply with the quasi-equilibrium assumption before resuming the simulation.

3.3.1. Strain-rate effect on the viscoelastic response

To examine the time-dependent viscoelastic behavior of a semi-flexible network, we performed simulations on a network comprised of 1200 Blundell-Terentjev semi-flexible fibers. Each fiber was comprised by 15 segments with a contour length (L) and persistence length (l_p) of 1 unit in a volume of 30x30x30 units. We assumed perfect bond exchange ($k_d = k_a$) and employ Brownian time integration to update the positions and velocities of all particles in the network with a drag parameter $\gamma_t = 10$. A reduced style of units *lj*, which sets fundamental values such as the Boltzmann constant to 1, was used. Prior to loading the system, we allowed a healing period to initialize the formation of transient bonds followed by an equilibration procedure to minimize both the potential energy and force equilibrium within the network system.

In our simulations, we first controlled the mechanical behavior of the network by varying the Weissenberg number, W, while keeping the dissociation constant, k_d, fixed at 0.1. Shortly, the Weissenberg number is a dimensionless parameter commonly used to study viscoelastic materials, defined as the ratio of the dissociation constant k_d to the stretch rate $\dot{\lambda}$. Strain-rate effect on semi-flexible networks has been studied in various fields such as mechanics, physics, and biology. In this study, we considered four different values of W: 100, 10, 1, and 0.1. Our simulations revealed the network's sensitivity to the strain rate, manifested through a more rigid response at higher Weissenberg numbers. At lower values of W, the network exhibited a more compliant response, attributable to the rapid breaking and reformation of bonds when compared to the stretching rate.

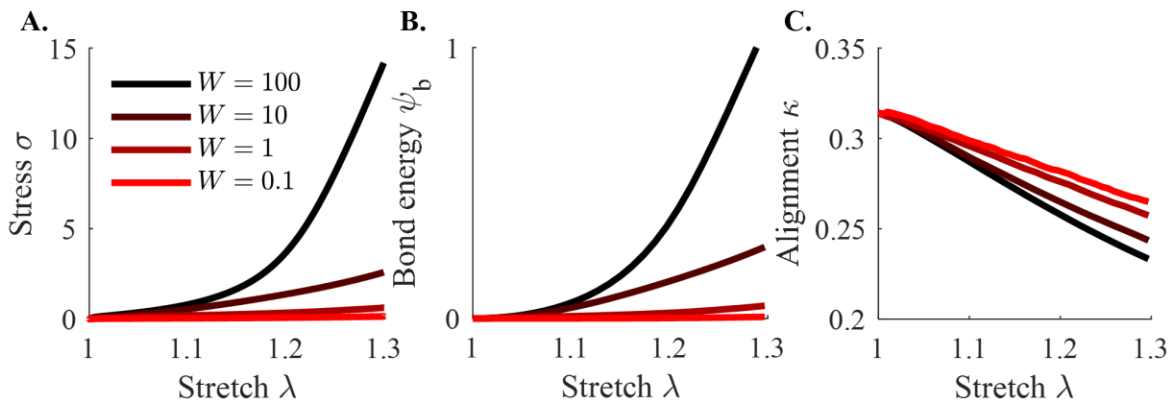

Figure 3.3. Strain-rate effect on semi-flexible networks for the stress (**A**), free energy (**B**) and alignment coefficient κ (**C**).

In Figure 3.3, we presented the simulation results for all values of W. The results revealed a non-linear response of the network over time, with an applied stretch of 1.25 in all cases (Figure 3.3 A). Notably, the stress σ and elastic potential ψ_b exhibited a divergence for W = 100 relative to lesser W values. Accelerated network stretching resulted in enhanced alignment while rigid cross-links function as unyielding anchor points permitting the reorientation of semi-flexible beads in the direction of the applied tension. All the simulations were initialized with a κ = 0.32 (approximating isotropic conditions) and achieved different degrees of alignment, ranging from approximately 0.23 to 0.27, depending on W. Our model confirmed the time-dependent viscoelastic response of the network during loading stage and underscored the crucial role played by the Weissenberg number in controlling the mechanical behavior of semi-flexible networks.

3.3.2. Stress-relaxation response on semi-flexible networks with dynamic bonds and effect of holding time on plastic realignment

We examined the network's plastic reconfiguration by applying a tensile stretch λ = 1.25 (W = 10), followed by an unloading phase to investigate network rearrangement at σ = 0. Utilizing a

consistent stretch ratio $\dot{\lambda}$ for both loading and unloading, five distinct holding durations were employed, ranging from 0 s to complete relaxation (Figure 3.4 A-B).

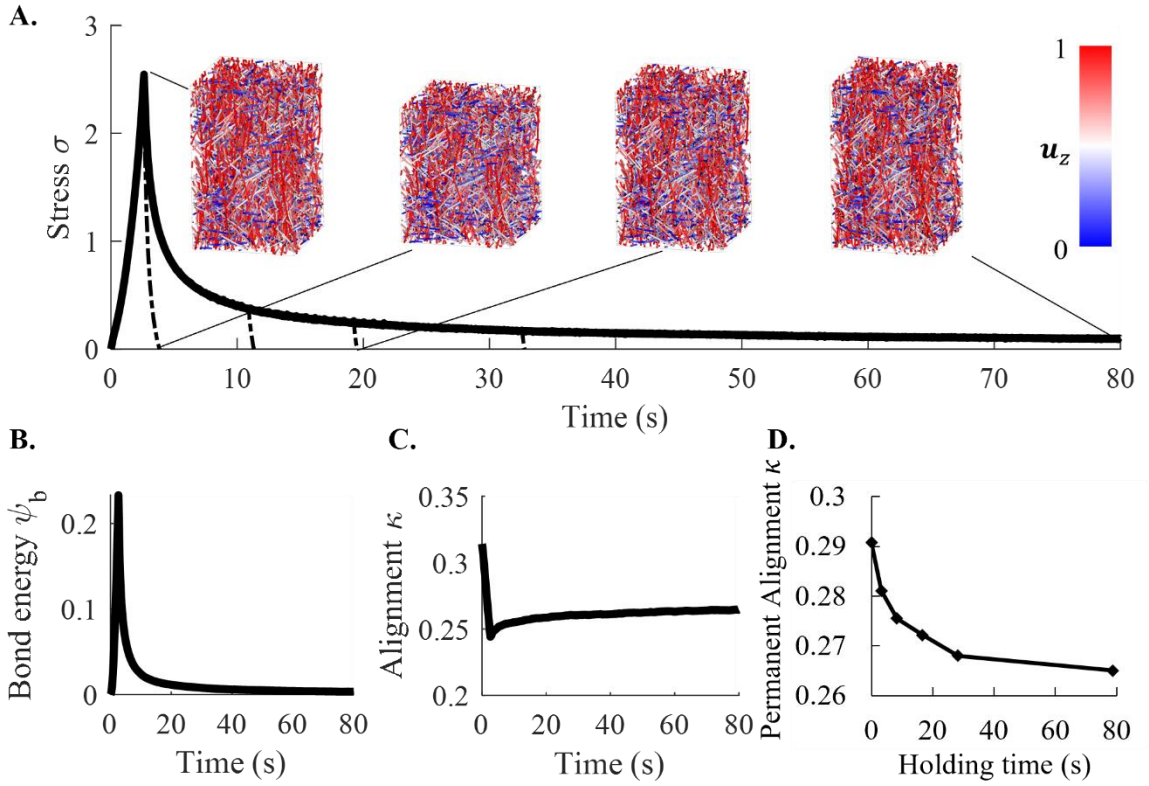

Figure 3.4. Effect of holding time on plastic realignment after stress-relaxation. **A.** Stress evolution. Highlights of the discrete network model at σ = 0 for different relaxation times. Color-scale shows the relative alignment of the beads with respect to the orientation vector. **B-C.** Evolution of the free energy ψ_b and alignment parameter κ for a complete relaxation stage. **D.** Permanent alignment at σ = 0 as a function of the duration of the relaxation stage.

Figure 3.4 presents the stress evolution post removal of the applied stretch for each holding time. Network orientation is emphasized in (A), where bead coloration corresponds to its relative orientation to the previously established alignment vector $\boldsymbol{a}$. This model delineated how alignment amplified during the loading phase up to the relaxation stage. In our simulation, the initial network

alignment was κ_0 = 0.32 while the final alignment at the conclusion of the complete relaxation stage was κ_f = 0.26 (Figure 3.4 C). It is important to notice that realignment reaches its maximum at the end of the loading stage, κ_{max} = 0.24, and then decreases during the relaxation stage. In a polymer network, the chains have a natural tendency to adopt random coil conformations due to their entropic nature. When a deformation is held during stress-relaxation, the chains may still attempt to adopt more entropically favorable conformations, which can lead to a change in alignment even without further macroscopic deformation.

Simulations revealed that holding time had a significant effect on plastic realignment in networks with bond dynamics during stress-relaxation (Figure 3.4 D). Holding time refers to the duration for which a material, in this case, a semi-flexible network, is subjected to constant strain during a stress-relaxation experiment. In polymer networks with reversible bond dynamics, the longer the holding time, the more opportunities there are for the bonds to break and reform. This leads to a more significant plastic realignment when the system returns to a stress-free configuration (σ = 0) as the network is allowed to adapt and reorganize its structure.

3.4. CONCLUSION

In this study, we have addressed the problem of understanding the mechanical response and network reconfiguration of semi-flexible networks with transient cross-links. We have developed a physically based mesoscale model framework and implemented simulations that capture the essential features of these networks, specifically focusing on the viscoelastic behavior, strain-rate dependence, and stress-relaxation response.

Our model demonstrated its ability to replicate the continuum stress-stretch approximation described by Gasser, Ogden, and Holzapfel (GOH) for hyperelastic materials ($k_d = k_a = 0$), which is particularly relevant to biological solids. The GOH model has been widely adopted in the literature for characterizing the mechanical behavior of biological materials due to its capability to capture the non-linear anisotropic response exhibited by these systems. Our study revealed the impact of the network orientation parameter, κ, on the GOH characteristic parameters, k_1 and k_2.

Notably, as the network became more isotropic, both k_1 and k_2 increased exponentially. Furthermore, our analysis unveiled that increasing the number of fibers and cross-links per unit volume leads to higher k_1 values for each κ, while k_2 appears to be independent of the number of fibers and cross-links per unit volume. The successful replication of the GOH model in our simulations validates the applicability of our theoretical framework and computational approach to the study of biological materials. By capturing the relationship between the network orientation parameter and the GOH characteristic parameters, our model provided valuable insights into the mechanical behavior of biological solids, including their anisotropic and non-linear response to deformation.

Through our simulations, we demonstrated the strain-rate effect on the viscoelastic response of semi-flexible networks with dynamic bonds ($k_d = k_a > 0$). By varying the Weissenberg number,

W, while keeping the dissociation bond frequency, k_d, fixed, we observed that the network's sensitivity to strain rate manifested through a more rigid response at higher Weissenberg numbers. Conversely, at lower values of W, the network exhibited a more compliant response due to the rapid breaking and reformation of bonds compared to the stretching rate. This behavior highlights the importance of the Weissenberg number in regulating the mechanical response of semi-flexible networks.

Our study found that network orientation plays a crucial role in the stress evolution post removal of the applied stretch. The model outlined in Figure 3.4 A that alignment amplified during the loading phase and up to the relaxation stage. This behavior is attributed to the entropic nature of polymer chains, which have a natural tendency to adopt random coil conformations. Furthermore, our simulations revealed that holding time significantly impacts plastic realignment in networks with bond dynamics during stress-relaxation, as shown in Figure 3.4 D. In polymer networks with reversible bond dynamics, an increase in holding time allows more opportunities for the bonds to break and reform. Consequently, this leads to a more significant plastic realignment when the system returns to a stress-free configuration, as the network reorganizes its structure.

In forthcoming research, we endeavor to develop an advanced continuum theoretical framework, based on the transient network theory, particularly tailored to semi-flexible networks with relatively short cross-links. This framework will enable a more comprehensive understanding of the mechanical behavior of such networks. Furthermore, by comparing the results from continuum model simulations with those from the discrete model simulations, we aim to validate the accuracy and reliability of both approaches.

In summary, our study provided a comprehensive understanding of the mechanical response and network reconfiguration of semi-flexible networks with transient cross-links. Our simulations

offered valuable insights into the complex interplay between microscopic structure and macroscopic mechanical properties in semi-flexible networks with permanent cross-links. The subject matter was highlighted by the ubiquity of semi-flexible networks in various fields, including mechanics, physics, and biology. Our work not only provides a sense of closure on the fundamental aspects of semi-flexible networks but also opens new avenues for future research, ultimately aiming to optimize and control the mechanical properties of these networks for various applications.

CHAPTER 4:

A MESO-SCALE VISCOELASTIC-PLASTIC CONSTITUTIVE MODEL OF FIBRIN GELS

In recent years, there has been a growing interest in understanding the mechanical properties of biological tissues and their role in regulating cellular behavior. Among the various components of the extracellular matrix (ECM), fibrin has gained particular attention due to its widespread presence in blood clots, role in wound healing, and for its use in tissue engineering applications. A comprehensive understanding of the viscoelastic and plastic behavior of fibrin gels at the meso-scale is essential for developing effective therapeutic strategies and designing biomaterials that mimic the native ECM.

4.1. BACKGROUND AND MOTIVATION

The extracellular matrix (ECM) of multicellular organisms is responsible for carrying stresses and maintaining tissue structure while influencing many other biological properties and functions of the tissue. ECM is composed of a variety of different molecules including proteins, carbohydrates, lipids, and nucleic acids. These molecules interact with each other to form a sophisticated three-dimensional (3D) fibrillar network that supports and regulates cell activity and functionality. The unique composition and arrangement of these networks gives rise to tissues with different mechanical responses. For instance, a random (or isotropic) organization of the network fibers[142,143] leads to a more manageable and softer response to loading than highly aligned (or anisotropic) network fibers[144,145]. McKee *et al.* (2011) showed on different soft biological tissues that stiffness values for a single tissue can span several orders of magnitude if loads are applied in the preferred orientation of the fibers[146]. Besides network orientation and elastic properties, inelastic mechanical properties such as viscoelasticity and plasticity have an impact on cell spreading, motility, and differentiation[147,148]. For example, Chaudhuri *et al*. (2016) and Cameron *et al*. (2011) discovered the influence of changing substrate viscosity, regardless of substrate stiffness, on numerous cell behaviors[149–151]. Accurately characterizing the mechanical properties of the ECM is essential for advancing our understanding of the mechanical behavior of tissues, informing material design, and improving clinical outcomes. A key aspect of characterizing its mechanical properties precisely is the development of constitutive models that accurately describe the viscoelastic and plastic properties of ECM materials. In this chapter, we present a novel meso-scale viscoelastic-plastic constitutive model of fibrin gels, one of the main components of the ECM. Our model builds on previous work in this field and provides a framework for accurately

characterizing the mechanical behavior of fibrin gels, which has important implications for tissue engineering and regenerative medicine.

Fibrin is a crucial component of the extracellular matrix and plays a significant role in a wide range of cellular processes, such as cell adhesion, proliferation, and differentiation, wound healing, angiogenesis, and inflammation[17,152]. It is formed during blood clotting and serves as the scaffold for hemostatic clots and obstructive thrombi in blood vessels. Additionally, fibrin has extensive biomedical applications, serving as a versatile biomaterial in hemostatic sealants, tissue engineering, drug and cell delivery vehicles, and matrices for cell culturing[153,154]. Due to its fundamental biological and medical importance, molecular mechanisms of fibrin formation, as well as fibrin structure and properties, remain a major focus of investigation[155].

Fibrin gels possess a remarkable three-dimensional network structure made from fibrinogen and thrombin, two proteins involved in blood clotting[156]. The intricate architecture of fibrin gels is highly dependent on a multitude of factors, including fibrinogen concentration, thrombin activity, calcium ions, *p*H, temperature, and mechanical stress[154,157,158]. This multifaceted dependency gives rise to fibrin gels with a diverse array of properties, such as elasticity, stiffness, porosity, and fiber diameter, making them a compelling subject for in-depth study[159].

Thrombin has the unique ability to activate other proteins by cleaving them into smaller fragments. One such protein is fibrinogen, which, upon activation by thrombin, undergoes a transformation into fibrin monomers[160–162]. These monomers then assemble to form the fibrous network of fibrin gel. In addition to activating fibrinogen, thrombin also plays a crucial role in activating platelets and other factors involved in regulating coagulation, further highlighting its importance in the formation and behavior of fibrin gels. Thrombin cleaves fibrinopeptides *A* and *B* from fibrinogen,

unveiling knobs that can bind to holes on other fibrin molecules[152,163]. These knob-hole bonds dictate the structure and mechanical properties of fibrin gels[164].

Knob-hole bonds are essential non-covalent and reversible interactions that occur between fibrin monomers during fibrin polymerization. Knob-hole bonds are located in both the central nodule and the end nodules of fibrin monomers. After thrombin cleaves fibrinopeptides, knobs *A* and *B* are exposed in the central nodule, while holes *a* and *b* are consistently exposed in the γ- and β-nodules at the ends[165,166] (Figure 4.1 A). To form knob-hole bonds, knobs *A* and *B* bind to holes *a* and *b*, respectively[163,167]. These interactions form a stable fibrin network, which is crucial for clot formation as well as for tissue engineering applications. The resulting fibrin monomers interact with each other in a half-staggered manner to produce two-stranded protofibrils (Figure 4.1 B). Polypeptide chains, αC-regions, mediate the primary interaction between fibrin protofibrils forming covalent bonds by a plasma transglutaminase, Factor XIIIa[168,169]. The αC-regions are formed by compact αC-domains tethered to the bulk of the molecule with flexible αC-connectors and play a significant role during deformation of fibrin fibers[170]. As a result of fibrin polymerization initiated by knob-hole bonds, protofibrils with a half-staggered orientation are formed, constituting the fibers of the fibrin matrix (Figure 4.1 C). Fibrin fibers branch to yield a three-dimensional gelled network[17]. The knob-hole bonds impact various properties of the fibrin matrix, such as fiber diameter, branching density, viscoelasticity (and plasticity), extensibility, and resistance to rupture, which in turn influence the functionality of fibrin gels[171].

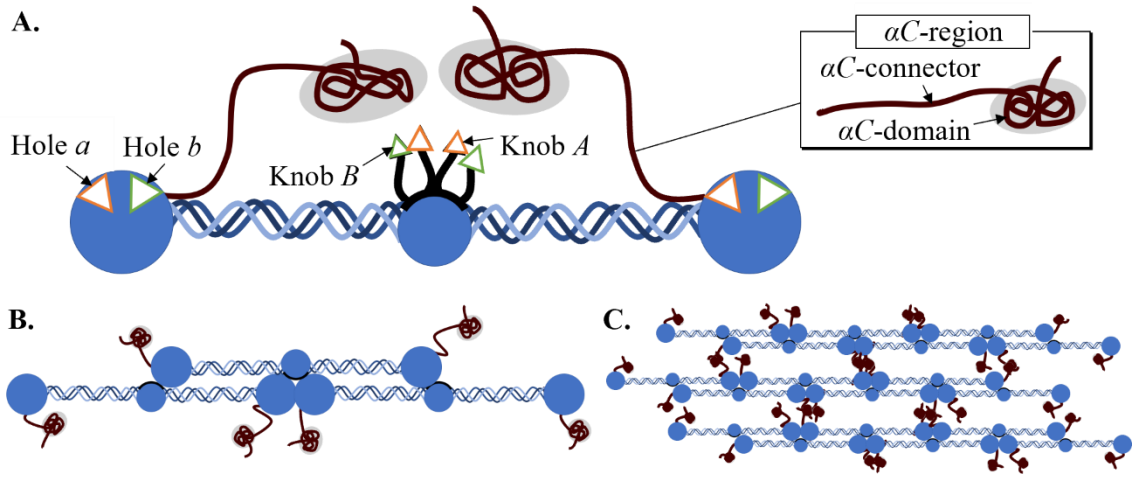

Figure 4.1. Multiscale arrangement of fibrin fiber. Hierarchical arrangement of fibrinogen (**A**) assembling into protofibrils (**B**), and lateral and axial aggregation to form fibers (**C**) is shown schematically.

Fibrin is recognized as a semiflexible polymer, exhibiting both rigidity and flexibility in its structure[122,172–174]. The mechanical behaviors of semiflexible polymers like fibrin are crucial for their biological functions. Fibrin gels are complex, highly adaptable networks which display unique mechanical properties due to their hierarchical structure and non-linear stress-strain response. The mechanical behavior of fibrin gels is dictated by factors such as fiber diameter, branching, and cross-linking density. Strain stiffening in fibrin gel networks is believed to stem from two possible mechanisms. The first, known as the entropic model, suggests that the entropic elasticity of individual polymers resists extension[175,176]. The second, referred to as the enthalpic model, proposes that strain stiffening arises from the alignment of fibers in the direction of the strain, transitioning to a regime dominated by fiber stretching at higher strains[123,138,177–180]. Both mechanisms contribute to the unique mechanical properties observed in fibrin gel networks. Stretched fibers causes them to stiffen more than surrounding fibers at lower stresses, allowing the

more strained, stiffer fibers to transmit strain load to the less stressed fibers and reducing strain concentration[158,181,182].

The strength of fibrin gels and their viscoelastic properties are significantly influenced by the non-covalent knob-hole bonds, which exhibit a "catch-slip" bond behavior[22,183,184]. These bonds become stronger as they are stretched, and then weaken, ultimately altering the gel's strength in response to tensile force. Such behavior plays a crucial role in the gel's ability to resist large deformations and prevent premature rupture, thus preserving the gel's structural integrity. These observations emphasize the importance of knob-hole bonds in regulating the mechanical properties of fibrin gels and shed light on their potential applications in developing novel biomaterials.

Research into fibrin has been conducted at multiple levels, from examining molecular interactions between its monomers[185,186], to investigating fiber network characteristics at the mesoscale[187–190], and analyzing stress-strain responses of entire gels at the macroscale[174,178]. Comprehending the development, progression, and spread of defects in fibrin gels, as well as their origins, is crucial for a proper characterization of these gels. The presence of pores and defects introduces inherent property gradients and heterogeneity at the network scale within the gels[191]. The size of these features restricts the applicability of continuum approaches, as these models typically assume smooth and homogenous materials. However, the length scale of these features also means that a significant number of constituents would need to be included in detailed modeling approaches, which limits the effectiveness of techniques like molecular dynamics (MD)[192]. Consequently, many MD studies concentrate on the interactions of just one or a few macromers. Even when using simplified MD methods, such as solvent smoothing, these approaches demand substantial computational time and resources[193]. Therefore, explicit, mesoscopic models are necessary to connect the microstructural and global mechanical property responses of gels. These models can

capture the length scale of heterogeneities and local topological features while utilizing statistical representations of elements like individual entropic chains[3]. Aghvami *et al.* (2016)[194] compared the mechanical response of fibrin gels using a nonfibrous strain-stiffening model and a volume-averaged fiber network model while Zohravi *et al.* (2023)[195] proposed a generalized-mesoscale-clustering (GMC) framework to study both static and dynamic states of cluster development on blood-related clustering ranging from fibrin network formation to platelet aggregation. Recently, Filla *et al.* (2023)[196] generated a model to describe the non-linear elastic response of protofibril bundle. Their proposed model was limited to a single fiber domain and did not include time-dependent effects due to bond dynamics between protofibrils. Despite significant progress in characterizing the mesoscopic mechanical properties of fibrin gels, there remains a need for physically based constitutive models that can accurately capture their meso-scale viscoelastic-plastic behavior and the network topology evolution.

Developing a robust mesoscale viscoelastic-plastic constitutive model of fibrin gels not only enhances our understanding of their mechanical properties, but also has significant implications for the field of mechanobiology. Cells are known to respond to the mechanical cues from their surrounding microenvironment, and these interactions play a crucial role in various biological processes such as cell migration, proliferation, and differentiation. By providing a detailed description of the mechanical environment experienced by cells within fibrin gels, the constitutive model can help elucidate the underlying mechanisms governing cellular behavior and response to mechanical stimuli.

In this chapter, we present a meso-scale viscoelastic-plastic constitutive model of fibrin gels that accounts for the structural and mechanical complexities observed in these networks. Through a comprehensive review of existing experimental data and theoretical models, we identified key

parameters that govern the mechanical response of fibrin gels and proposed a unified framework to describe their viscoelastic-plastic behavior. We proposed bond dynamics as a novel mechanism for describing strain-stiffening and force-dependent viscoelastic material behavior of fibrin gels. We sought to better understand the time-dependent mechanics of fibrin gels to inform their design and to provide a model that may be extended to a range of biopolymers which share similar network topology.

4.2. MATERIALS AND METHODS

The computational model proposed within this chapter is informed and verified by empirical findings from Jimenez *et al*. (2023). This section will provide a concise, yet comprehensive, overview of the methodological approach and materials employed in their investigation.

Fibrin gels fabrication: Uniform fibrin gels were created with final fibrinogen concentrations of 2 and 4 mg/mL by mixing human fibrinogen (FIB3, Enzyme Research Laboratories) and Alexa Fluor (AF) 488 or 546 labeled human fibrinogen (F13191, Molecular Probes) in a 1:10 ratio of fluorescent to non-fluorescent fibrinogen, along with 1 μL 2M CaCl2 and 0.5 U thrombin (HT 1002A, Enzyme Research Laboratories) for every mg of fibrinogen in phosphate buffered saline (PBS). The mixture was promptly transferred into molds containing frames to facilitate tensile testing and left to polymerize for 5 minutes.

Orthogonal fibrin gel imaging for three-dimensional mesoscale network analysis: To elucidate the intricate 3D mesoscale organization of fibrin networks, an orthogonal rotation bath was employed to facilitate imaging in the *x*-*y* and *x*-*z* planes. This approach was essential to attain precise fiber orientation distributions within the 3D network, compensating for the diminished resolution in the *z*-direction relative to the *x*-*y* plane due to objective constraints. Utilizing a STELLARIS 5 confocal microscope (Leica) with an Apochromatic 63× (NA = 0.90) water-immersible objective, image stacks (29.4 × 29.4 × 29.4 μm, 1024 × 1024 × 70 px resolution) were obtained at 0° and 90° rotations about the *x*-axis. Gels of 2 mg/mL (n = 3) and 4 mg/mL (n = 3) concentrations were examined.

Stress-relaxation experiments: Fibrin gels were subjected to 1-, 2-, and 3-mm displacements at a velocity of 66 μm/s (approximately 0.01 s−1), allowing for 60-minute relaxation intervals for each

increment. Both 2 mg/mL (n = 3) and 4 mg/mL (n = 3) gels were tested in each experiment, totaling 12 fibrin gels overall. Two fiducial markers of 50 × 50 μm dimensions were photobleached on fibrin gel surfaces, separated by 200 μm and embedded to a depth of 200 μm, utilizing a STELLARIS confocal microscope equipped with an Apochromatic 10× (NA = 0.40) water-immersible objective. Initial fibrin gel cross-sections, covering the entire region between the photobleached markers, were imaged at 10× magnification. Subsequently, fiber network image stacks were acquired at 63× following the methodology delineated above, exclusively in the x–y plane. Owing to microscale vibrations impeding the concurrent recording of force and confocal images, two distinct experiments were conducted to: (1) examine strain-dependent alterations in fibrin network architecture, and (2) assess stress relaxation in fibrin gels. A FemtoTools micromanipulator system (FT-RS1002) was employed for unidirectional tensile deformation of fibrin gels in both experiments, with distinct mounting systems.

4.3. CONSTITUTIVE RELATION FOR FIBRIN NETWORKS

In this section, we present our model, which incorporates mesoscale interaction potentials, pairwise bead bond interactions, and bond angle constraints or bending resistance. Additionally, we address bond exchange between fibrin fibers. By adopting this all-encompassing approach, we provide a highly accurate depiction of fibrin fiber mechanics, ultimately enhancing our understanding of the underlying mechanisms and potentially guiding the development of targeted therapies.

4.3.1. Non-affine deformation

Non-affine deformation refers to the irregular and complex changes in the structure and shape of a material when it is subjected to an external force. In the context of semi-flexible polymer networks, understanding non-affine deformation is essential for analyzing the mechanical behavior and structural properties of these materials[180]. In this section, we will discuss the concept of non-affinity and how it can be incorporated into a mesoscale model using a Brownian dynamics (BD) integrator.

Molecular dynamics (MD) simulations are a powerful tool for studying complex phenomena such as collision, aggregation, and breakage events in atomistic detail. MD simulations rely on classical Newtonian mechanics to model the motion of every molecule in the system, including solutes and solvents[197]. To accomplish this, interaction forces between molecules must be defined, typically through pairwise additive force laws for different molecule types (i.e., solute-solute, solute-solvent, and solvent-solvent). These forces are often derived from potential energy functions, such as the Lennard-Jones potential, which accounts for short-range repulsive forces and long-range attractive Van der Waals forces.

Briefly, BD technique is used to simulate the dynamics of particles that undergo Brownian motion using Newton's laws of motion in the limit that inertial forces are negligible compared to viscous forces. Assuming the thermal fluctuations are negligible, the stochastic equation of motion for the center of mass positions, $d\boldsymbol{r}$, is defined as $d\boldsymbol{r}/dt = -\gamma_t^{-1}\boldsymbol{f}$ [198,199], where γ_t is the drag coefficient, and $\boldsymbol{f}$ is the resultant force.

A comparison of the number of simulation time steps executed per second of CPU time demonstrated that there are more than 3 orders of magnitude speedup in the BD simulations[200]. Given these limitations, researchers have turned to alternative methods, such as BD simulations. This approach significantly reduces computational demands, making it a more feasible option for modeling mesoscale systems.

In the mesoscale model of semi-flexible polymer networks, non-affinity will be applied by incorporating the principles of Brownian dynamics. By leveraging the BD approach, we can gain valuable insights into the behavior of semi-flexible polymer networks under non-affine deformation, shedding light on their mechanical properties and potential applications.

4.3.2. Elastic energy and stress

As an illustration of the model, the beads connections are modeled following wormlike chain model or Blundell and Terentjev approximation[139,201]. This fully analytical model has the advantage of capturing the right physics in both the low and the high temperature limits, as well as in tension and compression/buckling regimes up to the highly bent elastic limit. To prescribe a finite contour length, we employ the following free energy expression $\psi_b(x)$ as a function of its end-to-end separation, $r = |\boldsymbol{r}(L) - \boldsymbol{r}(0)|$, which is useful in analyzing its mechanic properties, such as the force-extension relation.

$$\psi_b(\hat{r}) = k_b T \left[\frac{\pi^2}{2} \frac{l_p}{L} \, (1 - \hat{r}^2) + \frac{L}{l_p} \frac{2}{\pi(1 - \hat{r}^2)} \right], \tag{4.16}$$

where k_b is Boltzmann's constant, T is the reference temperature and $\hat{r}$ is defined as the end-to-end distance of the beads $\hat{r} = r/L$. The wormlike chain model assumes that the segments are unstretchable, i.e., the force in these interactions diverges in the limit $\hat{r} \to 1$ enforcing that $\psi_b(\hat{r}) \to \infty$ when the chains are stretched to their full contour length L. This nonlinear divergence at high chain stretch is common to semiflexible polymeric chains. In fully extended polymer chains, the conformational degrees of freedom are minimized, and the stiffness of the chains is no longer entropically driven, rather it is governed by the much stiffer stretching of the beads. From Eq. 4.16, the force-extension expression $f(\hat{r})$ can be written as:

$$f(\hat{r}) = k_b T \left[-\pi^2 \frac{l_p}{L^2} \hat{r} + \frac{4}{\pi l_p} \frac{x}{(1 - \hat{r}^2)^2} \right] \tag{4.17}$$

The finite extension limit for this approximation gives the divergent force scaling: $f \to (k_b T/\pi l_p)(1 - \hat{r})^{-2}$. To incorporate the effects of bending resistance into our mesoscale framework, let us assume that the local internal energy varies quadratically with the filament curvature. The bending modulus is related to the persistence length by $\kappa = l_p k_b T$.

Assuming the previously force-extension ($f(\hat{r})$) response of a single chain is known, the stress $\boldsymbol{\sigma}$ in the network can be directly evaluated through the virial formula as

$$\boldsymbol{\sigma} = \frac{1}{2V} \sum_{i}^{N} \sum_{j} \boldsymbol{r}_{ij} \otimes \boldsymbol{f}_{ij}, \tag{4.18}$$

where V is the domain volume, $\boldsymbol{r}_{ij}$ is the end-to-end vector between node i connected to node j and $\boldsymbol{f}_{ij}$ refers to the pairwise tensile and repulsive force between said nodes[202]. In this study, we

disregard the inertial component of virial stress, which is typically observed in atomistic or molecular discrete models. This decision is based on the overdamped assumption, positing that nodal inertia is inconsequential, and we employ the virial formulation that is intrinsic to continuum models.

4.3.3. Incorporating bond dynamics in mesoscale model

Recent force spectroscopy experiments into the nature of the adhesions between fibrin fibers indicated the presence of weak inter-fiber cross-links between compacted fibers that exhibit a Bell-like behavior under tension[184]. Mesoscale models easily permit probabilistic rupture of bonds through models such as Eyring's[49,92] or Bell's[50] theory, while inherently tracking the topological evolution of the network. To capture this behavior, we develop our model based on the transient network theory (TNT)[32]. The TNT begins with the statistical treatment of networks comprised of randomly oriented flexible chains connected by reversible bonds with intrinsic association and dissociation rates, k_a and k_d, respectively. Assuming perfect bond exchange ($k_d = k_a$),

$$k_d(f) = k_0 \, exp\left(\frac{f}{f_0}\right), \tag{4.19}$$

where k_0 is the spontaneous rate, f_0 is a sensibility parameter, and f is the current bond force. In their study, Litvinov *et al*. (2018)[184] performed single molecule forced unbinding experiments utilizing optical trap methodologies to elucidate the intricate influence of mechanical load on fibrin's structural integrity. By employing molecular modeling of the *A*:*a* knob-hole complex, they established the underlying structural basis for the catch-slip bond behavior observed in fibrin polymers. Their findings revealed that the noncovalent *A*:*a* knob-hole bond initially exhibits increased strength under tensile force (catch bonds), but subsequently experiences diminishing

strength once the force surpasses a critical threshold (slip bonds). In this study, we describe the time-dependent response of fibrin by characterizing the evolution of the dissociation rate.

4.4. COMPUTATIONAL APPROACH

Fiber network models provide insights into the microstructural mechanisms of deformation in fibrous matrices. Modelling fibrin at its fiber level will allow us to capture macroscopical behaviors such as strain-stiffening, viscoelasticity and plasticity while observing the underlying mechanisms that originate them.

Available data for informing our physically based model for fibrin gels at fiber length-scale is limited, particularly when contrasted with the abundance of data at the protofibril level[196,203]. This research introduces the first fibrin fiber network model to simultaneously: (1) computationally ascertain contour length (L^F) and persistence length (l_p^F) for fibrin fibers derived from the mechanical response of protofibril bundles; (2) reproduce the force-strain curve of fibrin fiber networks under tension; (3) incorporate force-dependent bond exchange between fibrin fibers; (4) generate accurate predictions of fibrin fiber mechanics and network alignment which are corroborated by experimental results. Computations are conducted utilizing the open-source Large-scale Atomic/Molecular Massively Parallel Simulator (LAMMPS)[140] and the atomistic simulation data are visualized using an open-source software package OVITO[204].

4.4.1. Protofibril bundle model

The multiscale modeling approach is essential when examining fibrin networks, as direct simulation of large-scale fibrin bundles would be computationally infeasible and excessively resource intensive. To mitigate these challenges, we derive the requisite material properties for fibrin fibers, namely contour length (L^F) and persistence length (l_p^F), by performing uniaxial stretch simulations on a representative protofibril bundle model. Furthermore, we analytically investigate

the influence of varying the cross-section number of protofibril (N) within a bundle on the properties L^F and l_p^F, elucidating the complex relationship between these variables.

Our protofibril bundle model is informed from previously acquired data. Zhmurov *et al*. (2018)[203] conducted an in-depth examination of fibrin protofibril morphology utilizing experimental AFM imagery. Their findings revealed an average contour length of 213 ± 101 nm and end-to-end distance of 197 ± 86 nm for fibrin protofibrils. A consequent end-to-end to contour length ratio of 0.94 ± 0.09 denotes an inherent bending propensity in these structures. In a study by Filla *et al*. (2023)[196], the protofibril count in fibrin fiber cross sections ranged from 207 to 421. Predictions from Filla's model indicated an αC-region persistence length of approximately 0.36 nm. Fablo *et al*. (2008)[205] revealed in their study that αC-region contour length is ~600 nm. A typical protofibril consists of 15-20 half-staggered monomers[206], therefore, each protofibril can be modeled as a straight chain with N^m beads. Each protofibril can be connected to neighbors protofibrils through αC-regions or *A*:*a* interactions. We incorporated Yesudasan and Averett's (2021)[207] neighboring protofibril configuration from their bundle model, utilizing a d_0 = 7 nm for radial and circumferential protofibril spacing[168] (Figure 4.2 A).

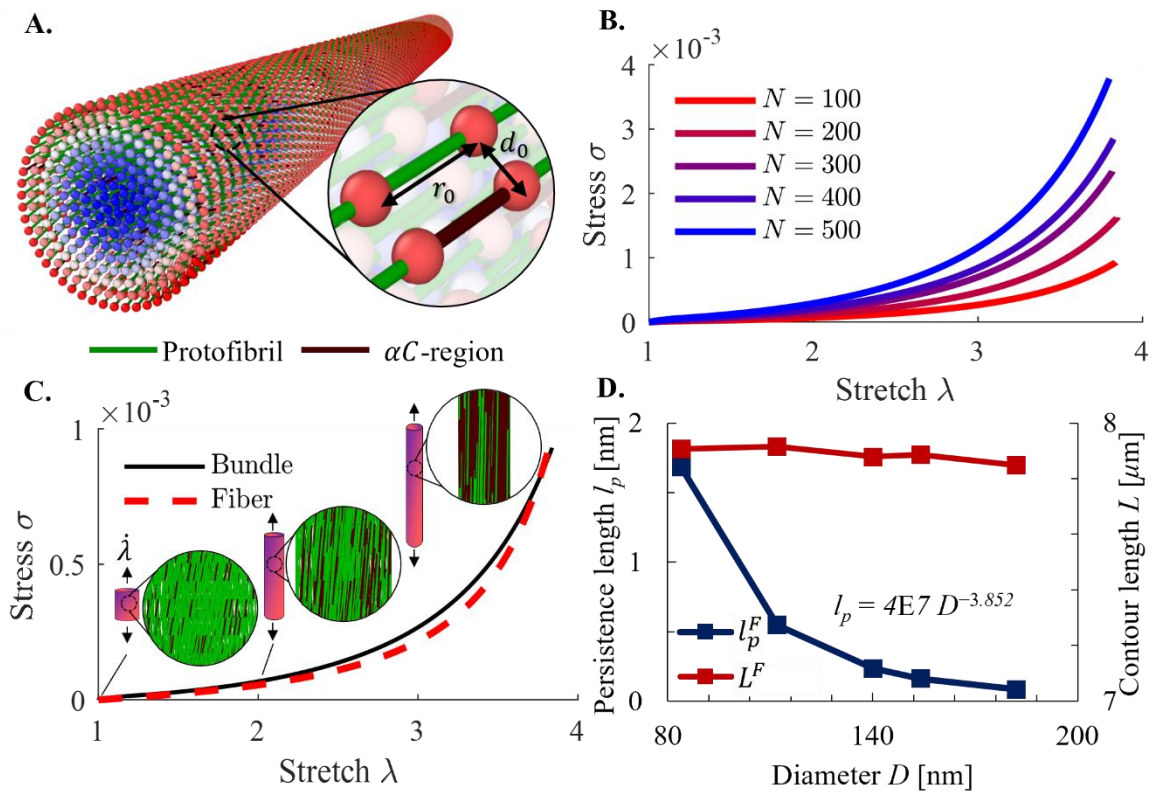

Figure 4.2. Comprehensive mechanical model of a fibrin fiber via protofibril bundle generation. **A.** Cross-sectional perspective of the protofibril bundle, revealing twisted protofibrils along the axial orientation. Particle hues range from blue to red for enhanced visual distinction, while an enlarged fiber surface representation illustrates the resting end-to-end distance (r_0) and inter-protofibril gap (d_0). **B.** Stress-stretch curve analysis for bundles exhibiting varying protofibril quantities within cross-sectional areas. **C.** Comparative evaluation of the anticipated fibrin fiber response and the corresponding protofibril bundle response (N = 100) with graphics depicting the details of the network configuration evolution. **D.** Determination of predicted persistence length (l_p^F) and contour length (L^F) for a fibrin fiber with a resting length of r_0^F = 1.7 μm, considering differing numbers of fibers in the cross-sectional arrangement

Bundles of protofibrils are generated by concatenated protofibril in series. Protofibrils within the bundle are twisted by rotating their positions around the z-axis[208,209]. Each of the protofibrils in

our model is divided into N^m segments (or beads) of length b^m. In our model, N^m follows a normal distribution between 15-20. Therefore, the contour length for each of the protofibrils is defined as $L^{PF} = N^m b^m$.

Connections between beads are used as binding points between the protofibrils and are used to assign bending stiffness (defined between three consecutive junctions) and extension resistance (defined between two consecutive junctions). The permanent intra-protofibrils connection points or nodes are used as anchor points for potential formation of cross-links with other fibers in the network. Each node is allowed to form 2 αC-regions cross-links and 2 A:a cross-links with the surrounding protofibrils at a maximum distance of 30 nm and 8 nm respectively.

Following successful cross-link formation among beads from distinct protofibrils, axial stretching is applied at a chosen constant stretch rate, $\dot{\lambda}$, to accurately characterize the bundle's elastic response. We subsequently analyze the impact of varying protofibril quantity within the cross-sectional area, N, on the mechanical response.

4.4.2. Fibrin network model

As shown in Chapter 3, our network model is able to generate discrete networks with a desired initial topology through the definition of the order parameter κ previosuly introduced by Gasser *et al.* (2006)[137]. Briefly, the network initialization involves randomly placing filaments within a cubic domain, adhering to a transversely isotropic distribution function of θ governed by the π-periodic von Mises distribution, and abiding by the minimum overlap distance δ. The initialization concludes once filament placement capacity is reached, succeeded by cross-link formation via harmonic spring elements.

Therefore, it is crucial to accurately initialize the network topology. Data from Jimenez *et al.*

(2023)[18] revealed that the initial volume fraction (computed from confocal images as the ratio of white pixels to the entire pixel domain) amounted to 0.102 and 0.151 for fibrin gels at concentrations of 2 mg/mL and 4 mg/mL, respectively. In our model, we assume the beads, or fibers in this context, are devoid of volume. To account for initial volume exclusion in our computational model, we assign a virtual diameter to the fibers, thereby preventing initial overlaps. Assuming fibers in our system are 1.7 x 0.25 μm (length x diameter), we calculate the volume fraction of fibrin fibers within a network relative to the total volume. Each fiber in the network is divided into 20 segments to open the possibility to form inter-fibers non-covalent bonds (Figure 4.3 A). Fiber structural parameters are properly adjusted.

The alignment parameter κ is derived from confocal images and it is calculated as described in Chapter 3. In the stress-free state, it is found to be 0.242 and 0.265 for fibrin gels with concentrations of 2 mg/mL and 4 mg/mL, respectively. The network is constructed by constraining the number of fibers in such a way that the volume fraction is maintained, and the desired initial network topology is achieved.

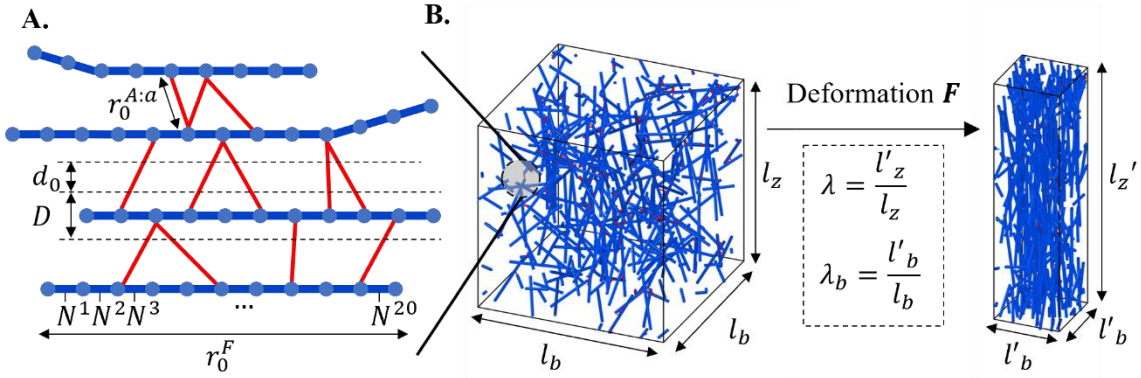

Figure 4.3. Discrete network model for fibrin gels. **A.** Schematic representation of the discrete network system. Each individual fiber (blue) with resting length r_0^F is discretized into 20

segments with proportional l_p^F and L^F, effectively approximating the continuous fiber structure. Non-covalent cross-link interactions (red) are placed between fibers with a resting length $r_0^{A:a}$. **B.** Visualization of the network before (left) and after (right) applying the deformation gradient tensor $\boldsymbol{F}$.

Once the intended initial alignment is accomplished, we provide sufficient time for the network formation through the establishment of non-covalent *A*:*a* interactions between fibers. As a result, the cross-linked fibers embody the distinct branches that shape the fibrin network structure. Bonds are created between fibrin fibers situated at a distance $d_{A:a} = D + d_0$, in which D signifies the fiber diameter, and d_0 functions as a correction factor facilitating bond formation (Figure 4.3 A). The equilibrium bond length is defined at $r_0^{A:a}$.

Jimenez *et al*. (2023) observed that fibrin gels were not incompressible when stretched. In addition to their large extensibility, fibrin gels also display a dramatic decrease in volume when they are stretched[122]. The deformation gradient $\boldsymbol{F}(t)$ tensor takes the simple form $\boldsymbol{F}(t) = \text{diag}[\lambda_l, \lambda_l, \lambda]$, where $\lambda \geq 1$ is the length ratio along the pre-alignment direction and $0 < \lambda_l \leq 1$ represents the lateral length ratio (Figure 4.3 B). The change in volume may be attributable to significant fluid loss between fibers, a phenomenon previously observed and ascribed to either fiber buckling perpendicular to the deformation direction or protein unfolding that augmented exposure to hydrophobic groups[122], thereby expelling water and compacting stretched fibers. Although non-poroelastic behaviors are considered, we deliberately apply a compressible deformation by controlling the stretch exerted in each direction.

4.5. RESULTS

4.5.1. *In silico* quantification of fibrin fibers material properties

The focus of this analysis is to explore the mechanical response of the protofibril bundle and its dependence on the number of protofibrils (N) present in the bundle's cross-sectional area. It is hypothesized that an increase in the cross-sectional number of fibers results in a stiffer mechanical response from the bundle. To test this hypothesis, five different bundle sizes are evaluated, with N values ranging from 100 to 500.

Non-periodic simulations were conducted using the Large-scale Atomic/Molecular Massively Parallel Simulator (LAMMPS) to investigate the behavior of protofibril bundles. These simulations involve fixing the position of the face, with particles moving outside the face being deleted in the subsequent timestep when re-neighboring occurs.

Prior to the application of axial stretch to the bundles, a two-stage equilibration process was employed. The first stage aimed to minimize both the potential energy and force balance within the system between protofibrils, while the second stage was implemented after the formation of αC-regions between the protofibrils at a maximum distance of 30 nm. Subsequent to the second equilibration stage, the mechanical response of the protofibril bundle was assessed. The initial length of the protofibrils was modeled by a normal distribution encompassing 15 to 20 segments (N^m) with a length of 10 nm per segment. The axial alignment of the segments permits an intra-protofibril gap, thereby facilitating the formation of αC-regions along the axial orientation. Total axial initial length of the bundle was 1.7 μm. The bundles were elastically deformed until reaching a maximum applied stretch of 3.82 ± 0.017 (ϵ = 282%)[205]. This is comparable to the single-fiber extensibility that is observed when a fibrin fiber is laterally stretched with an atomic force

microscope[210].

The structural parameters for fibrin fibers (L^F and l_p^F), were directly fitted based on the mechanical response derived from the protofibril bundle simulations. The fibers were characterized using the same constitutive model as previously introduced by Blundell and Terentjev. The objective function consisted of the mean squared error (MSE) between the bundle model predictions and the fiber simulations for each number of protofibrils in the cross-sectional area (N) (Figure 4.2 C). The results demonstrate that as the bundle becomes thicker, the persistence length of the fibers (l_p^F) decreases. This observation can be described by the equation $l_p^F = 4\text{E}7D^{-3.8}$ (R^2=1). Conversely, the contour length (L^F) remains constant across varying N values, with L^F = 7.89 ± 0.024 μm (Figure 4.2 D).

In accordance with earlier studies[16,170,211–213], the findings from our simulations are noteworthy as they suggest that the unfolding process of the αC-region within the bundles plays a crucial role in determining the elasticity, strain-stiffening, and maximum stretch observed in the mechanical properties of fibrin fibers.

4.5.2. Evolution of fiber alignment in fibrin networks

Upon determining L^F and l_p^F of fibrin fibers, we proceeded to assess the predictive effectiveness of our model in relation to the evolution of network topology. As described in Section 4.4.2., we initialized the networks with an alignment parameter κ. We evaluated our model for fibrin gels at concentrations of 2 mg/mL and 4 mg/mL, employing values of $\kappa = 0.242$ and 0.265, respectively. It is noticeable that the gels deviated from perfect isotropy (κ = 1/3), revealing alignment in a preferred direction, $\boldsymbol{a_0}$, prior to deformation. In our simulations, the preferred direction was situated along the *z*-axis.

After bond formation, we subjected the network to compressible tensile loading, reaching a stretch of λ = 1.3 in the $\boldsymbol{a_0}$ direction (*z*-axis), assuming periodic boundary conditions. By matching the volume fraction *J* observed in the experimental data at high strain as compressive deformation in the *x* and *y* directions, we quantified the network alignment parameter κ and volume fraction *J* evolution. As illustrated in Figure 4.4, our model accurately predicted alignment for both concentrations and effectively captured the volume fraction evolution observed in the experimental data.

The model's predictions align with experimental observations of fiber alignment. At the end of the deformation stage, the model predicted alignment parameter κ of 0.06 and 0.048, while experimental values are 0.063 ± 0.005 and 0.052 ± 0.004 for 2 mg/mL and 4 mg/mL concentrations, respectively.

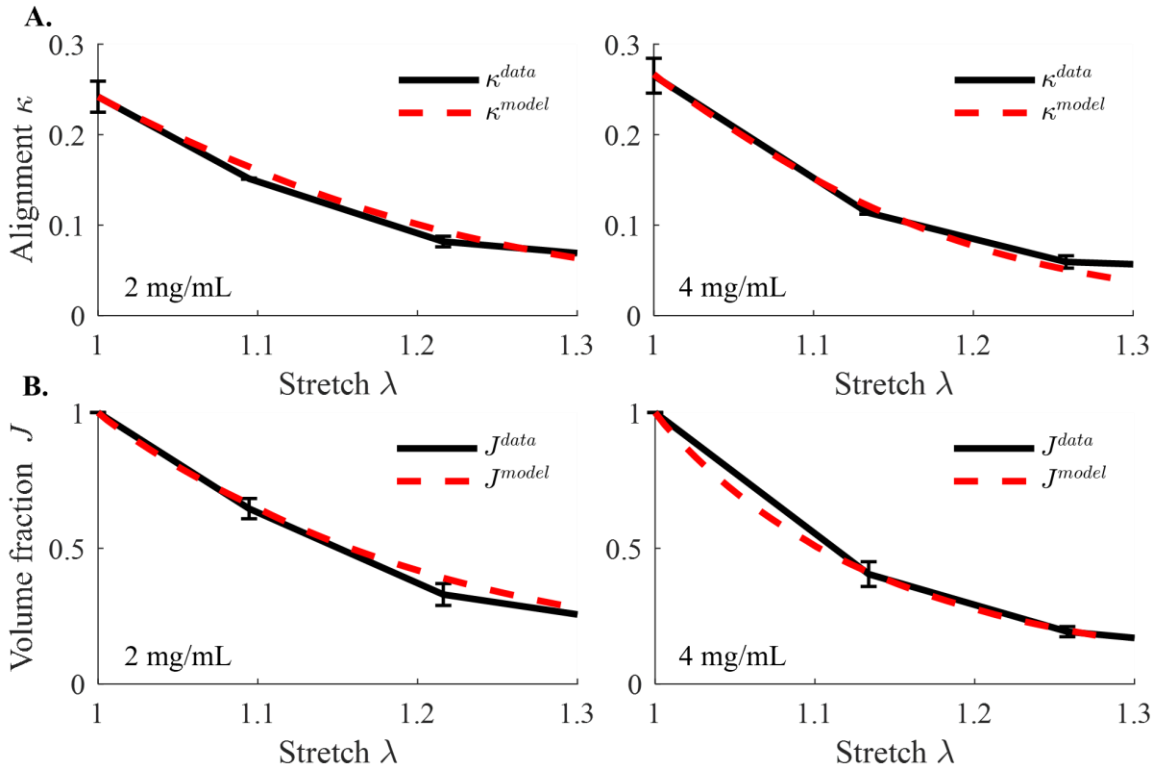

Figure 4.4. Comparison of the evolution of the alignment parameter κ (**A**) and volume fraction J (**B**) between experimental data and discrete network model for fibrin gels with concentrations of 2 mg/mL (left) and 4 mg/mL (right).

4.5.3 Time-dependent response

Next, we can proceed to model a fibrin network and characterize its viscoelastic properties through the analysis of non-covalent bonds (*A*:*a* interactions[181]) between fibers. Multi-step stress-relaxation experiments served as an indispensable tool for calibrating and validating the time-dependent response of the discrete model. Within these experiments, the gels underwent a sequence of strain increments, each followed by a relaxation period. Each increment consisted of 10% strain and was maintained for one hour, ultimately culminating in a final strain of 30%.

The experimental stress evolution curve was derived from the recorded force data obtained during experimental testing and the actual cross-sectional area. Simulation results remarkable captured the experimental stress evolution data for fibrin gels with concentrations of 4 mg/mL (Figure 4.5) and provided insights on the alignment parameter κ.

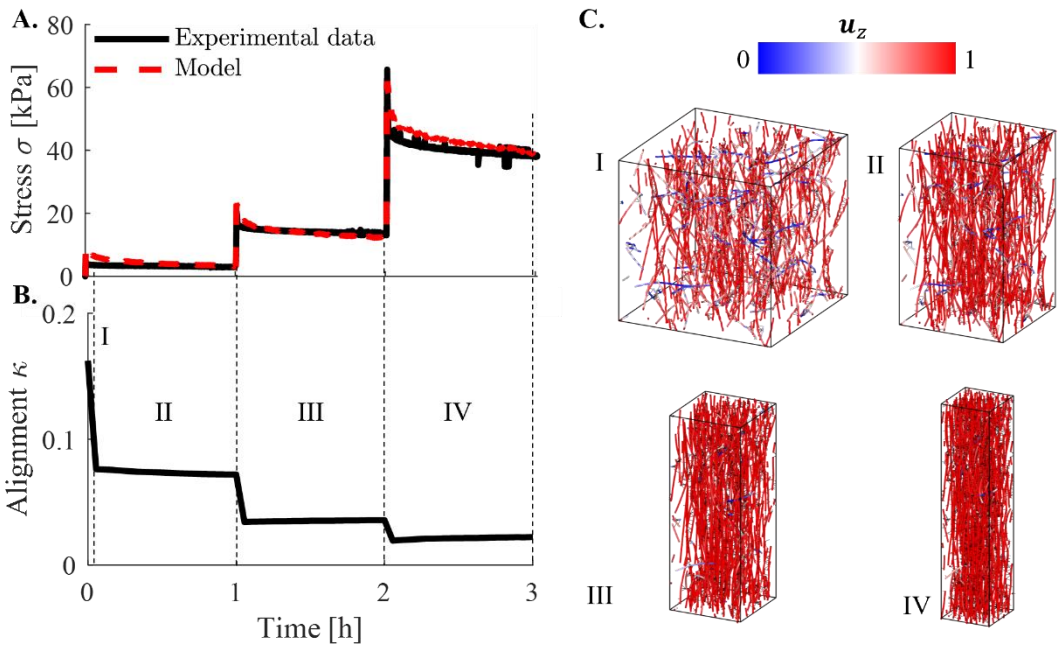

Figure 4.5. Time-dependent response of the discrete network model in 4 mg/mL fibrin gels. **A.** An analytical comparison of stress evolution between mean experimental data derived from Jimenez *et al*. (2023) and the discrete network model. **B.** A predictive assessment of the variation in the alignment parameter κ. At the stress-free state, the discrete model matches the experimental topology recorded. **C.** I-IV highlights the reorganization of network structures throughout the multi-step stress relaxation process. Bonds are colored by alignment, computing the *z*-component of the unit vector of the bond direction.

The proposed model successfully captured critical aspects of the system, including the peak stress at the conclusion of each loading phase and the equilibrium stress at the end of relaxation stages. The force-dependent dissociation rate ($k_d(f)$) enabled the accurate representation of both short-term and long-term relaxation responses. For fibrin gels with a concentration of 4 mg/mL, the parameters k_0 and f_0 were determined to be 0.011 and 1656, respectively.

4.6. DISCUSSION

This study proposes an innovative multiscale computational framework to investigate fibrin fiber networks and their underlying mechanics. The model is designed to capture complex mechanical behaviors observed in fibrin gels, such as strain-stiffening, viscoelasticity, and plasticity, while simultaneously elucidating the associated microstructural mechanisms. By combining a physically- based model of fibrin fibers at the protofibril level using a discrete network model, we effectively reproduced the experimental mechanical response of fibrin gels. This work provides novel insights into the structure-function relationships governing the behavior of fibrin gels under tensile loading.

Our approach begins with simulating protofibril bundles to determine the fibrin fibers' material properties, namely contour length (L^F) and persistence length (l_p^F). The analysis revealed a dependency of l_p^F on the number of protofibrils (N) within the bundle's cross-sectional area, with l_p^F decreasing as the bundle becomes thicker. Conversely, L^F remains relatively constant across different N values, signifying that the bundle size did not have a significant impact on the fiber's intrinsic stretching properties.

Upon determining the fibrin fibers' structural parameters, the model is extended to the network scale, capturing the evolution of network topology and alignment under compressible tensile loading. The model accurately predicts alignment for fibrin gels at different concentrations by effectively reproducing the volume fraction evolution observed experimentally. This demonstrates the model's ability to capture the interplay between fiber mechanics and network rearrangement under deformation, providing critical insights into how the network topology influences macroscopic mechanical properties.

Furthermore, the discrete network model is employed to characterize the time-dependent response of fibrin gels by analyzing non-covalent *A*:*a* interactions between fibers. The model successfully captures the stress evolution and relaxation response observed in multi-step stress-relaxation experiments, further showcasing its potential for providing a comprehensive understanding of fibrin gel mechanics.

Overall, the proposed multiscale computational framework demonstrates a robust ability to capture complex fibrin network behaviors and offers valuable insights into the structure-function relationships governing these materials. This model can potentially serve as a powerful tool for investigating fibrin gel mechanics in various applications, including wound healing, guide approaches for tissue engineering using fibrin gels, and to study pathological conditions related to fibrin clot formation.

4.7. FUTURE DIRECTIONS

The current multiscale computational framework has demonstrated its ability to capture the mechanical properties of fibrin networks, providing valuable insights into the structure-function relationships governing their behavior. However, there are several areas for improvement and future developments:

Compressible deformation and fluid phase implementation: In the current model, compressible deformation is imposed through boundary conditions, which does not account for the effects of fluid diffusion leaving the system. To provide a more comprehensive understanding of fibrin gel mechanics, future iterations of the model will include the implementation of a fluid phase. By considering fluid diffusion, the model can better capture the coupled mechanical and transport phenomena occurring in fibrin networks, leading to a more accurate representation of their behavior under various loading conditions.

Capturing plastic deformation and network rearrangement: The present model can track network topology and capture any plastic deformation of the network, depending on the boundary conditions applied to it. To further validate and improve the model's predictions, additional experiments can be performed where the sample is imaged after removing the load. These experimental observations will provide valuable insight into the network rearrangement and plastic deformation processes occurring in fibrin gels, ultimately enhancing the model's predictive capabilities.

By addressing these steps, the multiscale computational framework can be further refined to provide an even more accurate and comprehensive understanding of fibrin network mechanics.

CHAPTER 5:

CONCLUSIONS

As the study of biological soft materials gains increasing attention, it is essential to understand the mechanics of these complex systems to advance the various fields such as biophysics, materials science, and tissue engineering. The mechanical properties of biological networks play a critical role in their functionality[214], and consequently, the development of accurate models is vital for understanding their behavior under different conditions[14,215–218] (i.e., mechanical stress, strain, temperature, *p*H, and chemical environments). In this final chapter, we summarize the main findings of this dissertation, which contribute to bridging the knowledge gap in the field of semi-flexible network mechanics, with a focus on the viscoelastic-plastic response of agarose and fibrin networks.

While flexible network mechanics has been extensively studied, semi-flexible networks remain underexplored. Interest in characterizing semi-flexible network mechanics has surged due to the need to understand complex systems, such as connective tissue or the extracellular matrix[13,219]. Existing models fail to link network topology with macroscopic mechanical response, lacking accuracy due to the omission of molecular movement and rearrangement[69,220]. Many semi-flexible networks behave as dynamic networks, featuring reversible bonds with viscoelastic, nonlinear mechanical responses, which are an essential aspect of many biological systems[148]. Researchers endeavor to understand the interactions in these systems that lead to globally emergent responses, as they often exhibit rich mechanical behaviors. Accurate characterization is crucial for material choice, design, and advancements in cellular scale mechanobiology[151,221].

This thesis aims to develop physically based computational models of biological soft materials, integrating experimental observations, statistically based continuum mechanics, and discrete

numerical modeling techniques to offer new insights into the viscoelastic-plastic response of agarose and fibrin networks.

In **Chapter 2**, we developed a novel, physically based model for predicting the time-dependent behavior of agarose networks under unconfined compression, providing a reinterpretation of agarose network viscoelastic behavior using the transient network theory (TNT)[222]. This new approach considers the time-dependent evolution of the stress resulting from bond-exchange within the polymer network, setting it apart from previous phenomenological and continuum models describing viscoelasticity. Existing poroviscoelastic models do not accurately account for the movement and rearrangement of molecules within the agarose network[70,76]. By capturing the non-linear force-dependent evolution of bond dynamics, our model has uncovered a crucial insight: the lifetime of a bond is dependent on the force applied to it.

Our research has significant implications for the broader field of biopolymer networks. By characterizing the two main microstructural features responsible for agarose viscoelastic behavior, our continuum model can be extrapolated to other biopolymer networks, such as collagen and fibrin, to predict their material response as a function of bond kinetics. This enables the design and fabrication of gels based on bond dynamics to achieve specific time-sensitive behavior, with potential applications in bioengineering and tissue engineering.

Furthermore, our study demonstrates that the TNT can be applied in commercial finite element analysis (FEA) software, allowing for future 3D modeling of complex polymer behavior, such as crack propagation or cavity generation. This computational implementation has broad applicability, enabling the study of more complex geometries and offering insights into the coupling of poromechanics with network relaxation. The minor role of poromechanics in agarose supports the use of the TNT to control and predict the macroscopic time-dependent response of

physically crosslinked gels.

In **Chapter 3**, we introduced a coarse-grained, discrete numerical model specifically designed to investigate topological changes in transient semi-flexible networks without incurring the high computational costs associated with modeling the elemental constituents. This innovative approach enables us to explore a wider range of networks and assess their properties more efficiently. To enhance the representativeness of the networks that can be examined through this model, we incorporated nonlinear Blundell and Terentjev chains[139]. This choice offers several advantages, including capturing the appropriate physics in both low and high temperature limits, as well as in tension and compression/buckling regimes up to the highly bent elastic limit. Furthermore, our model considers the finite length of true entropic chains, which consistently serves to stiffen the network. The effects of this stiffening become particularly significant when the rate of deformation exceeds that of relaxation. This observation highlights the importance of considering the finite length of entropic chains when characterizing the mechanical properties of semi-flexible networks, as it can greatly influence their behavior under various deformation rates.

Our model demonstrated its effectiveness by accurately replicating the continuum stress-stretch approximation described by the GOH model, which is widely used in characterizing the mechanical behavior of biological materials[137]. By investigating the relationship between the network orientation parameter, κ, and the GOH characteristic and phenomenological parameters, k_1 and k_2, we have provided valuable insights into the mechanical behavior of biological solids, including their anisotropic and non-linear response to deformation.

For a network with dynamic bonds, we have highlighted the importance of the Weissenberg number in regulating the mechanical response of semi-flexible networks by examining the strain-rate effect on the viscoelastic response of these networks. This finding underscores the need to

consider strain-rate effects when characterizing the mechanical behavior of semi-flexible networks. Our study has also revealed the significant impact of holding time on plastic realignment during stress-relaxation. These insights can be instrumental in guiding the design and optimization of semi-flexible networks for various applications.

In **Chapter 4**, we expanded upon the research conducted in Chapter 3 by focusing on fibrin gels, which contribute to the mechanical strength of blood clots, and are considered among the most robust protein materials in nature[136]. Fibrin gels consist of protofibrils that self-assemble and bundle, forming networks of semi-flexible fibers. Our investigation demonstrated that the exceptional strain-stiffening response of fibrin networks is intrinsically linked to the hierarchical architecture of fibrin fibers.

To this end, we developed a comprehensive protofibril bundle model, informed by existing literature. Our model used nonlinear Blundell and Terentjev chains for the protofibril backbone, extension-limited flexible chains for the αC-regions, and probabilistic slip-bond detachment via Eyring's model for the *A*:*a* non-covalent bonds. This approach allowed us to capture the energetic penalty associated with highly stretched networks. Our findings revealed that the long extensibility characteristic of fibrin fibers primarily results from the deployment of αC-domains, while *A*:*a* interactions stabilize the bundle.

By stretching the bundles, we determined the structural parameters for fibrin fibers, which informed our chain model. This approach elucidates the underlying mechanisms responsible for the remarkable properties of fibrin networks. Our network model incorporated force-dependent dynamic bonds between fibers, enabling the examination of the nonlinear viscoelastic response of the gels. The model accurately represented the experimental data for fibrin gels provided by Jimenez et al. (2023) and demonstrated the capacity to predict the alignment and volume fraction

of the network domain during deformation[18].

Our model may help us to understand how mutations or pathological alterations in fibrin change the resilience of clots, which can cause hemorrhage or thromboembolism[223–225]. Specifically, our work may shed light on the molecular mechanism by which mutations or truncations of fibrinogen in its αC-region lead to several clotting disorders (dysfibrinogenemias[226]). Moreover, our findings suggest a new design concept for resilient synthetic materials with potential applications in drug delivery and tissue repair.

There are undoubtedly limitations associated with this current modeling approach. Firstly, the current model does not account for fluid diffusion effects, as it imposes compressible deformation through boundary conditions. To enhance the accuracy of the model, future iterations should incorporate a fluid phase, allowing the model to better represent the coupled mechanical and transport phenomena that occur in fibrin networks under various loading conditions. Secondly, although the model can track network topology and capture plastic deformation, it could benefit from additional experiments where the sample is imaged after load removal. These observations would offer deeper insights into network rearrangement and plastic deformation processes in fibrin gels, ultimately improving the model's predictive capabilities. By addressing these limitations, the multiscale computational framework can be further refined to provide a more comprehensive understanding of fibrin network mechanics.

As we look towards the future, our research aims to develop an advanced continuum theoretical framework, based on transient network theory, to further our understanding of the mechanical behavior of semi-flexible networks with relatively short cross-links. By comparing the results from continuum model simulations with those from discrete model simulations, we hope to validate the accuracy and reliability of both approaches.

In parallel to the advancements in our understanding of semi-flexible networks through the development of a continuum theoretical framework, another area of focus for our research will be centered around the properties and functionality of fibrin gels. The fibrin gel's physical properties and physiological functionality are predominantly governed by its topological and morphological characteristics, which hinge upon factors such as fiber dimensions, branching degree, spatial distribution, and mean inter-fiber distance, denoting the gel mesh size. Our multi-scale model facilitates regulation of these parameters, and upon validation through empirical data, future iterations can analyze the implications of modifying network topology on the consequent mechanical response, providing a comprehensive understanding of the interplay between fibrin gel network properties and their mechanical outcomes.

Our model offers valuable insights into controlling the αC-domains unfolding process in protofibrils bundles, which could pave the way for novel thrombus disruption strategies. One possible approach may involve stabilizing the coiled α-chain, making clots more brittle and thus easier to remove during thrombectomy. Alternatively, destabilizing the coiled α-chain could result in softer, less occlusive clots. Furthermore, the structural transitions observed at various scales in αC-domains may also have implications for the mechanics of other protein assemblies. This knowledge can potentially contribute to a deeper understanding of protein structure and function in numerous biological contexts.

In conclusion, this thesis has significantly advanced our understanding of soft matter mechanics, specifically the viscoelastic-plastic response of agarose and fibrin networks, through the development of innovative computational models that integrate experimental observations, statistically based continuum mechanics, and discrete numerical modeling techniques. Our findings have broad implications for the fields of biopolymer networks, bioengineering, and tissue

engineering, providing new insights into material choice and design, as well as the mechanical behavior of biological materials. By characterizing the critical microstructural features and dynamics that dictate the mechanical response of semi-flexible networks, we have laid the foundation for further advancements in cellular length-scale mechanobiology and the design of novel materials for various applications. As we continue to refine and validate our models, we anticipate that our research will contribute to a deeper understanding of the interplay between soft matter physics and the biological processes they govern, ultimately leading to innovative solutions for challenges in biotechnology, nanotechnology, and beyond.

LIST OF PUBLICATIONS

In support of these studies and other works that I contributed to thus far in my doctoral studies, my list of published works to date and works in late stages of preparation include the following:

- Crespo-Cuevas, V., Vernerey, F.J., Ferguson, V.L., **A Mesoscale Viscoelastic-Plastic Constitutive Model of Fibrin Gels**. [Manuscript in preparation]
- Vernerey, F.J., Crespo-Cuevas, V., Lamont, S., **Time-dependent mechanics of dynamically cross-linked semi-flexible networks**. [Manuscript in preparation]
- Crespo-Cuevas, V., Vernerey, F.J., Ferguson, V.L., **Poroviscoelastic-plastic mechanical response of agarose hydrogels**. *Soft matter* (2023), [https://doi.org/10.1039/D2SM01356H]
- Yu, Y., Fischenich, K.M., Weatherford, S., Schoonraad, S.A. Muralidharan, A., Uzcategui, A.C., Eckstein, K., Crespo-Cuevas, V., Rodriguez-Fontan, F., Guangheng, L., McLeod, R., Miller, N.H., Ferguson, V.L., Bryant, S.J., Payne, K.A., **3D Printed Growth Plate Mimetic for the Treatment of Physeal Injuries in a Rabbit Model**. *NPJ Regenerative Medicine* (2022), [https://doi.org/10.1038/s41536-022-00256-1]
- Tomaschke, A.A., Crespo-Cuevas, V., DelRio, F., Ferguson, V.L., **Influence of surface roughness on indentation-based micromechanical property assessments of a soft, hydrated material**, [Manuscript in preparation]. Planned Submission, 2023.
- Muralidharan, A., Crespo-Cuevas, V., Ferguson, V. L., McLeod, R.R., Bryant, S.J., **Effects of Kinetic Chain Length on the Degradation of Poly(β-amino ester)-Based Networks and Use in 3D Printing by Projection Microstereolithography**. *Biomacromolecules* (2022) [https://doi.org/10.1021/acs.biomac.2c00362].
- Hergert, J.E., Uzcategui, A.C., Muralidharan, A., Crespo-Cuevas, V., Ferguson, V.L., McLeod, R.R., **3D Printed Polymer Blends Fabricated using Grayscale Digital Light**

Processing. *Advanced Engineering Materials* (2022), [https://doi.org/10.1002/adem.202101543].

- Schoonrad, S.A., Fischenich, K.M., Eckstein, K.N., Crespo-Cuevas, V., Savard, L.M., Muralidharan, A., Tomaschke, A.A., Uzcategui, A.C., Randolph, M.A., McLeod, R.R., Ferguson, V.L., Bryant, S.J., **Biomimetic and Mechanically Supportive 3D Printed Scaffolds for Cartilage and Osteochondral Tissue Engineering using Photopolymers and Digital Light Processing**. *Biofabrication* (2021), [https://doi.org/10.1088/1758-5090/ac23ab].
- Uzcategui, A.C., Higgins, C.I., Hergert, J.E., Tomaschke, A.E., Crespo-Cuevas, V., Ferguson, V.L., Bryant, S., McLeod, R.R., Killgore, J.P., **Microscale Photopatterning of Through-thickness Modulus in a Monolithic and Functionally Graded 3D Printed Part**. *Small Science* (2020), 2000017 [https://doi.org/10.1002/smsc.202000017].
- Ghosh, S., Crespo-Cuevas, V., Seelbinder, B., Neu, C.P. **Image-based elastography of heterochromatin and euchromatin domains in the deforming cell nucleus**. *Small* (2020), 2006109 [https://doi.org/10.1002/smll.202006109].

REFERENCES

1. Löwen, H. Colloidal soft matter under external control. *J. Phys. Condens. Matter* **13**, R415 (2001).

2. Brown, M. F. Soft matter in lipid-protein interactions. *Annu Rev Biophys* **46**, 379–410 (2017).

3. Wagner, R. J., Dai, J., Su, X. & Vernerey, F. J. A mesoscale model for the micromechanical study of gels. *J. Mech. Phys. Solids* **167**, 104982 (2022).

4. de Gennes, P. G. Soft Matter. *Science* **256**, 495–497 (1992).

5. Lagerwall, J. P. F. & Scalia, G. A new era for liquid crystal research: Applications of liquid crystals in soft matter nano-, bio- and microtechnology. *Curr. Appl. Phys.* **12**, 1387–1412 (2012).

6. Vernerey, F. J., Lalitha Sridhar, S., Muralidharan, A. & Bryant, S. J. Mechanics of 3D Cell–Hydrogel Interactions: Experiments, Models, and Mechanisms. *Chem. Rev.* **121**, 11085–11148 (2021).

7. Maskarinec, S. A. & Tirrell, D. A. Protein engineering approaches to biomaterials design. *Curr. Opin. Biotechnol.* **16**, 422–426 (2005).

8. Langer, R. & Tirrell, D. A. Designing materials for biology and medicine. *Nature* **428**, 487–492 (2004).

9. Petka, W. A., Harden, J. L., McGrath, K. P., Wirtz, D. & Tirrell, D. A. Reversible hydrogels from self-assembling artificial proteins. *Science* **281**, 389–392 (1998).

10. Shen, T., Long, R. & Vernerey, F. Computational modeling of the large deformation and flow of viscoelastic polymers. *Comput. Mech.* **63**, 725–745 (2019).

11. Doi, M. *Soft Matter Physics*. (Oxford University Press, 2013). doi:10.1093/acprof:oso/9780199652952.001.0001.

12. Vernerey, F. J., Long, R. & Brighenti, R. A statistically-based continuum theory for polymers with transient networks. *J. Mech. Phys. Solids* **107**, 1–20 (2017).

13. Vernerey, F. J. Mechanics of transient semi-flexible networks: Soft-elasticity, stress relaxation and remodeling. *J. Mech. Phys. Solids* **160**, 104776 (2022).

14. H. Pritchard, R., Huang, Y. Y. S. & M. Terentjev, E. Mechanics of biological networks: from the cell cytoskeleton to connective tissue. *Soft Matter* **10**, 1864–1884 (2014).

15. Li, Y., Xiao, Y. & Liu, C. The Horizon of Materiobiology: A Perspective on Material-Guided Cell Behaviors and Tissue Engineering. *Chem. Rev.* **117**, 4376–4421 (2017).

16. Collet, J.-P. *et al.* The αC domains of fibrinogen affect the structure of the fibrin clot, its physical properties, and its susceptibility to fibrinolysis. *Blood* **106**, 3824–3830 (2005).

17. Weisel, J. W. & Litvinov, R. I. Fibrin Formation, Structure and Properties. in *Fibrous Proteins: Structures and Mechanisms* (eds. Parry, D. A. D. & Squire, J. M.) 405–456 (Springer International Publishing, 2017). doi:10.1007/978-3-319-49674-0_13.

18. Jimenez, J. M. *et al.* Multiscale Mechanical Characterization and Computational Modeling of Fibrin Gels. *Acta Biomater.* (2023) doi:10.1016/j.actbio.2023.03.026.

19. Chaudhuri, O., Cooper-White, J., Janmey, P. A., Mooney, D. J. & Shenoy, V. B. Effects of extracellular matrix viscoelasticity on cellular behaviour. *Nature* **584**, 535–546 (2020).

20. Zarrintaj, P. *et al.* Agarose-based biomaterials for tissue engineering. *Carbohydr. Polym.* **187**, 66–84 (2018).

21. Lewis, C. L., Stewart, K. & Anthamatten, M. The Influence of Hydrogen Bonding Side-Groups on Viscoelastic Behavior of Linear and Network Polymers. *Macromolecules* **47**, 729–740 (2014).

22. Litvinov, R. I. & Weisel, J. W. Shear strengthens fibrin: the knob–hole interactions display 'catch-slip' kinetics. *J. Thromb. Haemost.* **11**, 1933–1935 (2013).

23. Labropoulos, K. C., Rangarajan, S., Niesz, D. E. & Danforth, S. C. Dynamic Rheology of Agar Gel Based Aqueous Binders. *J. Am. Ceram. Soc.* **84**, 1217–1224 (2001).

24. Arnott, S. *et al.* The agarose double helix and its function in agarose gel structure. *J. Mol. Biol.* **90**, 269–284 (1974).

25. Rossiter, J. Soft robotics: the route to true robotic organisms. *Artif. Life Robot.* **26**, 269–274 (2021).

26. Dziuba, R., Kucharska, M., Madej-Kiełbik, L., Sulak, K. & Wiśniewska-Wrona, M. Biopolymers and Biomaterials for Special Applications within the Context of the Circular Economy. *Materials* **14**, 7704 (2021).

27. Martău, G. A., Mihai, M. & Vodnar, D. C. The Use of Chitosan, Alginate, and Pectin in the Biomedical and Food Sector—Biocompatibility, Bioadhesiveness, and Biodegradability. *Polymers* **11**, 1837 (2019).

28. Lakes, R. S. *Viscoelastic solids*. (CRC press, 2017).

29. Casalini, T. Molecular modeling of transport phenomena in hydrogels. (Politecnico di Milano, 2013).

30. Miehe, C., Göktepe, S. & Lulei, F. A micro-macro approach to rubber-like materials—Part I: the non-affine micro-sphere model of rubber elasticity. *J. Mech. Phys. Solids* **52**, 2617–2660 (2004).

31. Miehe, C. & Göktepe, S. A micro–macro approach to rubber-like materials. Part II: The micro-sphere model of finite rubber viscoelasticity. *J. Mech. Phys. Solids* **53**, 2231–2258 (2005).

32. Vernerey, F. J. Transient response of nonlinear polymer networks: A kinetic theory. *J. Mech. Phys. Solids* **115**, 230–247 (2018).

33. Tanaka, F. & Edwards, S. F. Viscoelastic properties of physically crosslinked networks. 1. Transient network theory. *Macromolecules* **25**, 1516–1523 (1992).

34. Yamamoto, M. The Visco-elastic Properties of Network Structure I. General Formalism. *J. Phys. Soc. Jpn.* **11**, 413–421 (1956).

35. Shen, T., Song, Z., Cai, S. & Vernerey, F. J. Nonsteady fracture of transient networks: The case of vitrimer. *Proc. Natl. Acad. Sci.* **118**, e2105974118 (2021).

36. Xu, L. *et al.* Thermosensitive P(AAc-co-NIPAm) Hydrogels Display Enhanced Toughness and Self-Healing via Ion–Ligand Interactions. *Macromol. Rapid Commun.* **43**, 2200320 (2022).

37. Vernerey, F. J. & Lamont, S. Transient mechanics of slide-ring networks: A continuum model. *J. Mech. Phys. Solids* **146**, 104212 (2021).

38. de Gennes, P. G. & Leger, L. Dynamics of Entangled Polymer Chains. *Annu. Rev. Phys. Chem.* **33**, 49–61 (1982).

39. Hui, C.-Y., Cui, F., Zehnder, A. & Vernerey, F. J. Physically motivated models of polymer networks with dynamic cross-links: comparative study and future outlook. *Proc. R. Soc. Math. Phys. Eng. Sci.* **477**, 20210608 (2021).

40. Le Tallec, P., Rahier, C. & Kaiss, A. Three-dimensional incompressible viscoelasticity in large strains: Formulation and numerical approximation. *Comput. Methods Appl. Mech. Eng.* **109**, 233–258 (1993).

41. Reese, S. & Govindjee, S. A theory of finite viscoelasticity and numerical aspects. *Int. J. Solids Struct.* **35**, 3455–3482 (1998).

42. Lubliner, J. A model of rubber viscoelasticity. *Mech. Res. Commun.* **12**, 93–99 (1985).

43. Gooneie, A., Schuschnigg, S. & Holzer, C. A Review of Multiscale Computational Methods in Polymeric Materials. *Polymers* **9**, 16 (2017).

44. Aksimentiev, A. & Hołyst, R. Single-chain statistics in polymer systems. *Prog. Polym. Sci.* **24**, 1045–1093 (1999).

45. Hatami-Marbini, H. & Picu, R. C. Scaling of nonaffine deformation in random semiflexible fiber networks. *Phys. Rev. E* **77**, 062103 (2008).

46. Picu, R. C. Mechanics of random fiber networks—a review. *Soft Matter* **7**, 6768–6785 (2011).

47. Hatami-Marbini, H. & Rohanifar, M. Mechanical properties of subisostatic random networks composed of nonlinear fibers. *Soft Matter* **16**, 7156–7164 (2020).

48. Arbabi, S. & Sahimi, M. Mechanics of disordered solids. I. Percolation on elastic networks with central forces. *Phys. Rev. B* **47**, 695–702 (1993).

49. Eyring, H. The Activated Complex in Chemical Reactions. *J. Chem. Phys.* **3**, 107–115 (1935).

50. Bell, G. I. Models for the Specific Adhesion of Cells to Cells. *Science* **200**, 618–627 (1978).

51. Ghareeb, A. & Elbanna, A. An adaptive quasicontinuum approach for modeling fracture in networked materials: Application to modeling of polymer networks. *J. Mech. Phys. Solids* **137**, 103819 (2020).

52. Ghareeb, A. & Elbanna, A. Modeling Fracture in Rate-Dependent Polymer Networks: A Quasicontinuum Approach. *J. Appl. Mech.* **88**, (2021).

53. Tabatabai, A. P. *et al.* Detailed Balance Broken by Catch Bond Kinetics Enables Mechanical-Adaptation in Active Materials. *Adv. Funct. Mater.* **31**, 2006745 (2021).

54. Rincon, S. A. *et al.* Kinesin-5-independent mitotic spindle assembly requires the antiparallel microtubule crosslinker Ase1 in fission yeast. *Nat. Commun.* **8**, 15286 (2017).

55. Singh, G. & Sundararaghavan, V. Modeling self-healing behavior of vitrimers using molecular dynamics with dynamic cross-linking capability. *Chem. Phys. Lett.* **760**, 137966 (2020).

56. Kaplan, D. L. Introduction to Biopolymers from Renewable Resources. in *Biopolymers from Renewable Resources* (ed. Kaplan, D. L.) 1–29 (Springer, 1998). doi:10.1007/978-3-662-03680-8_1.

57. Van de Velde, K. & Kiekens, P. Biopolymers: overview of several properties and consequences on their applications. *Polym. Test.* **21**, 433–442 (2002).

58. Kierfeld, J., Baczynski, K., Gutjahr, P. & Lipowsky, R. Semiflexible Polymers and Filaments: From Variational Problems to Fluctuations. *AIP Conf. Proc.* **1002**, 151–185 (2008).

59. Naghdi, T. *et al.* Chitin Nanofiber Paper toward Optical (Bio)sensing Applications. *ACS Appl. Mater. Interfaces* **12**, 15538–15552 (2020).

60. Aga, M. B. *et al.* Recent insights into carrageenan-based bio-nanocomposite polymers in food applications: A review. *Int. J. Biol. Macromol.* **192**, 197–209 (2021).

61. Comaposada, J., Marcos, B., Bou, R. & Gou, P. Influence of surfactants and proteins on the properties of wet edible calcium alginate meat coatings. *Food Res. Int.* **108**, 539–550 (2018).

62. Kato, Y., Iwamoto, M. & Koike, T. Fibroblast growth factor stimulates colony formation of differentiated chondrocytes in soft agar. *J. Cell. Physiol.* **133**, 491–498 (1987).

63. Horwitz, A. L. & Dorfman, A. THE GROWTH OF CARTILAGE CELLS IN SOFT AGAR AND LIQUID SUSPENSION. *J. Cell Biol.* **45**, 434–438 (1970).

64. Bnjía, J., Sittinger, M., Pitzke, P., Wilmes, E. & Hammer, C. Synthesis of Human Cartilage Using Organotypic Cell Culture. *ORL* **55**, 347–351 (1993).

65. Megone, W., Roohpour, N. & Gautrot, J. E. Impact of surface adhesion and sample heterogeneity on the multiscale mechanical characterisation of soft biomaterials. *Sci. Rep.* **8**, 6780 (2018).

66. Roberts, J. J., Earnshaw, A., Ferguson, V. L. & Bryant, S. J. Comparative study of the viscoelastic mechanical behavior of agarose and poly(ethylene glycol) hydrogels. *J. Biomed. Mater. Res. B Appl. Biomater.* **99B**, 158–169 (2011).

67. Martikainen, L., Bertula, K., Turunen, M. & Ikkala, O. Strain Stiffening and Negative Normal Force of Agarose Hydrogels. *Macromolecules* **53**, 9983–9992 (2020).

68. Bertula, K. *et al.* Strain-Stiffening of Agarose Gels. *ACS Macro Lett.* **8**, 670–675 (2019).

69. Wang, X., June, R. K. & Pierce, D. M. A 3-D constitutive model for finite element analyses of agarose with a range of gel concentrations. *J. Mech. Behav. Biomed. Mater.* **114**, 104150 (2021).

70. Ed-Daoui, A. & Snabre, P. Poroviscoelasticity and compression-softening of agarose hydrogels. *Rheol. Acta* **60**, 327–351 (2021).

71. Olberding, J. E. & Francis Suh, J.-K. A dual optimization method for the material parameter identification of a biphasic poroviscoelastic hydrogel: Potential application to hypercompliant soft tissues. *J. Biomech.* **39**, 2468–2475 (2006).

72. Soussou, J. E., Moavenzadeh, F. & Gradowczyk, M. H. Application of Prony Series to Linear Viscoelasticity. *Trans. Soc. Rheol.* **14**, 573–584 (1970).

73. Chen, J., Bader, D. L., Lee, D. A. & Knight, M. M. Finite Element Modeling of Cell Deformation When Chondrocyte Seeded Agarose Is Subjected to Compression. in *8th International Conference on Cell & Stem Cell Engineering (ICCE)* (eds. El Haj, A. & Bader, D.) 17–20 (Springer, 2011). doi:10.1007/978-3-642-19044-5_5.

74. Pauly, H. M., Place, L. W., Haut Donahue, T. L. & Kipper, M. J. Mechanical Properties and Cell Compatibility of Agarose Hydrogels Containing Proteoglycan Mimetic Graft Copolymers. *Biomacromolecules* **18**, 2220–2229 (2017).

75. Caccavo, D. & Lamberti, G. PoroViscoElastic model to describe hydrogels' behavior. *Mater. Sci. Eng. C Mater. Biol. Appl.* **76**, 102–113 (2017).

76. Caccavo, D., Cascone, S., Poto, S., Lamberti, G. & Barba, A. A. Mechanics and transport phenomena in agarose-based hydrogels studied by compression-relaxation tests. *Carbohydr. Polym.* **167**, (2017).

77. Wang, X., Eriksson, T. S. E., Ricken, T. & Pierce, D. M. On incorporating osmotic prestretch/prestress in image-driven finite element simulations of cartilage. *J. Mech. Behav. Biomed. Mater.* **86**, 409–422 (2018).

78. Pierce, D. M., Unterberger, M. J., Trobin, W., Ricken, T. & Holzapfel, G. A. A microstructurally based continuum model of cartilage viscoelasticity and permeability incorporating measured statistical fiber orientations. *Biomech. Model. Mechanobiol.* **15**, 229–244 (2016).

79. Wang, Q.-M., Mohan, A. C., Oyen, M. L. & Zhao, X.-H. Separating viscoelasticity and poroelasticity of gels with different length and time scales. *Acta Mech. Sin.* **30**, 20–27 (2014).

80. Hu, Y., Zhao, X., Vlassak, J. J. & Suo, Z. Using indentation to characterize the poroelasticity of gels. *Appl. Phys. Lett.* **96**, 121904 (2010).

81. Galli, M., Comley, K. S. C., Shean, T. A. V. & Oyen, M. L. Viscoelastic and poroelastic mechanical characterization of hydrated gels. *J. Mater. Res.* **24**, 973–979 (2009).

82. Strange, D. G. T. *et al.* Separating poroviscoelastic deformation mechanisms in hydrogels. *Appl. Phys. Lett.* **102**, 031913 (2013).

83. Terzaghi, K. *Theoretical Soil Mechanics*. (John Wiley & Sons, Ltd, 1943). doi:10.1002/9780470172766.

84. Coussy, O. *Poromechanics*. (John Wiley & Sons, 2004).

85. Bear, J. & Bachmat, Y. Macroscopic Description of Transport Phenomena in Porous Media. in *Introduction to Modeling of Transport Phenomena in Porous Media* 43–262 (Springer Netherlands, 1990). doi:10.1007/978-94-009-1926-6_2.

86. Gu, W. Y., Yao, H., Huang, C. Y. & Cheung, H. S. New insight into deformation-dependent hydraulic permeability of gels and cartilage, and dynamic behavior of agarose gels in confined compression. *J. Biomech.* **36**, 593–598 (2003).

87. Mao, B., Bentaleb, A., Louerat, F., Divoux, T. & Snabre, P. Heat-induced aging of agar solutions: Impact on the structural and mechanical properties of agar gels. *Food Hydrocoll.* **64**, 59–69 (2017).

88. Watase, M. & Arakawa, K. Rheological Properties of Hydrogels of Agar-agar. III. Stress Relaxation of Agarose Gels. *Bull. Chem. Soc. Jpn.* **41**, 1830–1834 (1968).

89. Holzapfel, G. A. *Nonlinear Solid Mechanics: A Continuum Approach for Engineering*. (2000).

90. Long, R., Qi, H. J. & Dunn, M. L. Modeling the mechanics of covalently adaptable polymer networks with temperature-dependent bond exchange reactions. *Soft Matter* **9**, 4083–4096 (2013).

91. Lee, E. H. Elastic-Plastic Deformation at Finite Strains. *J. Appl. Mech.* **36**, 1–6 (1969).

92. Eyring, H. Viscosity, Plasticity, and Diffusion as Examples of Absolute Reaction Rates. *J. Chem. Phys.* **4**, 283–291 (1936).

93. Lamont, S. & Vernerey, F. J. A Transient Microsphere Model for Nonlinear Viscoelasticity in Dynamic Polymer Networks. *J. Appl. Mech.* **89**, 011009 (2022).

94. Erdmann, T. & Schwarz, U. S. Stability of adhesion clusters under constant force. *Phys. Rev. Lett.* **92**, 108102 (2004).

95. Schwarz, U. S. & Safran, S. A. Physics of adherent cells. *Rev. Mod. Phys.* **85**, 1327–1381 (2013).

96. Klumpp, S. & Lipowsky, R. Cooperative cargo transport by several molecular motors. *Proc. Natl. Acad. Sci.* **102**, 17284–17289 (2005).

97. Buehler, M. J. & Yung, Y. C. Deformation and failure of protein materials in physiologically extreme conditions and disease. *Nat. Mater.* **8**, 175–188 (2009).

98. Prechtel, K. *et al.* Dynamic Force Spectroscopy to Probe Adhesion Strength of Living Cells. *Phys. Rev. Lett.* **89**, 028101 (2002).

99. Cates, M. E. Nonlinear viscoelasticity of wormlike micelles (and other reversibly breakable polymers). *J. Phys. Chem.* **94**, 371–375 (1990).

100. Thirion, P. & Tassin, J. Nonlinear viscoelasticity of entangled polymer chains. I. Response of the slip-link model to elongation strains. *J. Polym. Sci. Polym. Phys. Ed.* **21**, 2097–2108 (1983).

101. Pluen, A., Netti, P. A., Jain, R. K. & Berk, D. A. Diffusion of Macromolecules in Agarose Gels: Comparison of Linear and Globular Configurations. *Biophys. J.* **77**, 542–552 (1999).

102. Laurent, T. C. Determination of the structure of agarose gels by gel chromatography. *Biochim. Biophys. Acta BBA - Gen. Subj.* **136**, 199–205 (1967).

103. Johnson, E. M., Berk, D. A., Jain, R. K. & Deen, W. M. Diffusion and partitioning of proteins in charged agarose gels. *Biophys. J.* **68**, 1561–1568 (1995).

104. Fernández, E. *et al.* Rheological and thermal properties of agarose aqueous solutions and hydrogels. *J. Polym. Sci. Part B Polym. Phys.* **46**, 322–328 (2008).

105. Mow, V. C., Kuei, S. C., Lai, W. M. & Armstrong, C. G. Biphasic creep and stress relaxation of articular cartilage in compression? Theory and experiments. *J. Biomech. Eng.* **102**, 73–84 (1980).

106. Shen, T. & Vernerey, F. J. Rate-dependent fracture of transient networks. *J. Mech. Phys. Solids* **143**, 104028 (2020).

107. Pajic-Lijakovic, I., Milivojevic, M. & Clark, A. G. Collective Cell Migration on Collagen-I Networks: The Impact of Matrix Viscoelasticity. *Front. Cell Dev. Biol.* **10**, (2022).

108. Kendall, K. & Fuller, K. N. G. J-shaped stress/strain curves and crack resistance of biological materials. *J. Phys. Appl. Phys.* **20**, 1596 (1987).

109. Takano, Y. & Koibuchi, H. J-shaped stress-strain diagram of collagen fibers: Frame tension of triangulated surfaces with fixed boundaries. *Phys. Rev. E* **95**, 042411 (2017).

110. Long, R., Mayumi, K., Creton, C., Narita, T. & Hui, C.-Y. Time Dependent Behavior of a Dual Cross-Link Self-Healing Gel: Theory and Experiments. *Macromolecules* **47**, 7243–7250 (2014).

111. Lalitha Sridhar, S. & Vernerey, F. J. Mechanics of transiently cross-linked nematic networks. *J. Mech. Phys. Solids* **141**, 104021 (2020).

112. Speicher, D. W. & Marchesi, V. T. Erythrocyte spectrin is comprised of many homologous triple helical segments. *Nature* **311**, 177–180 (1984).

113. Wang, K., Ash, J. F. & Singer, S. J. Filamin, a new high-molecular-weight protein found in smooth muscle and non-muscle cells. *Proc. Natl. Acad. Sci.* **72**, 4483–4486 (1975).

114. Shoulders, M. D. & Raines, R. T. Collagen Structure and Stability. *Annu. Rev. Biochem.* **78**, 929–958 (2009).

115. Km, P., A, N., Gm, G., El, E. & Gi, Z. Incremental mechanics of collagen gels: new experiments and a new viscoelastic model. *Ann. Biomed. Eng.* **31**, (2003).

116. Ozerdem, B. & Tözeren, A. Physical response of collagen gels to tensile strain. *J. Biomech. Eng.* **117**, 397–401 (1995).

117. Krishnan, L., Weiss, J. A., Wessman, M. D. & Hoying, J. B. Design and application of a test system for viscoelastic characterization of collagen gels. *Tissue Eng.* **10**, 241–252 (2004).

118. Silver, F. H. & Landis, W. J. Viscoelasticity, Energy Storage and Transmission and Dissipation by Extracellular Matrices in Vertebrates. in *Collagen: Structure and Mechanics* (ed. Fratzl, P.) 133–154 (Springer US, 2008). doi:10.1007/978-0-387-73906-9_6.

119. Das, R. K., Gocheva, V., Hammink, R., Zouani, O. F. & Rowan, A. E. Stress-stiffening-mediated stem-cell commitment switch in soft responsive hydrogels. *Nat. Mater.* **15**, 318–325 (2016).

120. Petrie, R. J., Gavara, N., Chadwick, R. S. & Yamada, K. M. Nonpolarized signaling reveals two distinct modes of 3D cell migration. *J. Cell Biol.* **197**, 439–455 (2012).

121. Storm, C., Pastore, J. J., MacKintosh, F. C., Lubensky, T. C. & Janmey, P. A. Nonlinear elasticity in biological gels. *Nature* **435**, 191–194 (2005).

122. Brown, A. E. X., Litvinov, R. I., Discher, D. E., Purohit, P. K. & Weisel, J. W. Multiscale mechanics of fibrin polymer: gel stretching with protein unfolding and loss of water. *Science* **325**, 741–744 (2009).

123. Onck, P. R., Koeman, T., van Dillen, T. & van der Giessen, E. Alternative explanation of stiffening in cross-linked semiflexible networks. *Phys. Rev. Lett.* **95**, 178102 (2005).

124. Nam, S., Hu, K. H., Butte, M. J. & Chaudhuri, O. Strain-enhanced stress relaxation impacts nonlinear elasticity in collagen gels. *Proc. Natl. Acad. Sci.* **113**, 5492–5497 (2016).

125. Guidry, C. & Grinnell, F. Contraction of Hydrated Collagen Gels by Fibroblasts: Evidence for Two Mechanisms by which Collagen Fibrils are Stabilized. *Coll. Relat. Res.* **6**, 515–529 (1987).

126. Chandran, P. L. & Barocas, V. H. Microstructural mechanics of collagen gels in confined compression: poroelasticity, viscoelasticity, and collapse. *J. Biomech. Eng.* **126**, 152–166 (2004).

127. Abou Neel, E. A., Cheema, U., Knowles, J. C., Brown, R. A. & Nazhat, S. N. Use of multiple unconfined compression for control of collagen gel scaffold density and mechanical properties. *Soft Matter* **2**, 986–992 (2006).

128. Kayhanian, H. *et al.* Host muscle cell infiltration in cell-seeded plastic compressed collagen constructs. *J. Tissue Eng. Regen. Med.* **3**, 72–75 (2009).

129. Wess, T. J. Collagen Fibrillar Structure and Hierarchies. in *Collagen: Structure and Mechanics* (ed. Fratzl, P.) 49–80 (Springer US, 2008). doi:10.1007/978-0-387-73906-9_3.

130. Bhattacharjee, A. & Bansal, M. Collagen structure: the Madras triple helix and the current scenario. *IUBMB Life* **57**, 161–172 (2005).

131. Buehler, M. J. Atomistic and continuum modeling of mechanical properties of collagen: Elasticity, fracture, and self-assembly. *J. Mater. Res.* **21**, 1947–1961 (2006).

132. Xu, B., Li, H. & Zhang, Y. Understanding the viscoelastic behavior of collagen matrices through relaxation time distribution spectrum. *Biomatter* **3**, e24651 (2013).

133. Tang, Y., Ballarini, R., Buehler, M. J. & Eppell, S. J. Deformation micromechanisms of collagen fibrils under uniaxial tension. *J. R. Soc. Interface* **7**, 839–850 (2010).

134. Wagner, R. J., Hobbs, E. & Vernerey, F. J. A network model of transient polymers: exploring the micromechanics of nonlinear viscoelasticity. *Soft Matter* **17**, 8742–8757 (2021).

135. Salbreux, G., Charras, G. & Paluch, E. Actin cortex mechanics and cellular morphogenesis. *Trends Cell Biol.* **22**, 536–545 (2012).

136. Blombäck, B. & Okada, M. Fibrin gel structure and clotting time. *Thromb. Res.* **25**, 51–70 (1982).

137. Gasser, T. C., Ogden, R. W. & Holzapfel, G. A. Hyperelastic modelling of arterial layers with distributed collagen fibre orientations. *J. R. Soc. Interface* **3**, 15–35 (2006).

138. Heussinger, C., Bathe, M. & Frey, E. Statistical Mechanics of Semiflexible Bundles of Wormlike Polymer Chains. *Phys. Rev. Lett.* **99**, 048101 (2007).

139. Blundell, J. R. & Terentjev, E. M. Stretching Semiflexible Filaments and Their Networks. *Macromolecules* **42**, 5388–5394 (2009).

140. Thompson, A. P. *et al.* LAMMPS - a flexible simulation tool for particle-based materials modeling at the atomic, meso, and continuum scales. **1**, (2021).

141. Holzapfel, G. A., Gasser, T. C. & Ogden, R. W. A New Constitutive Framework for Arterial Wall Mechanics and a Comparative Study of Material Models. *J. Elast. Phys. Sci. Solids* **61**, 1–48 (2000).

142. Hollenstein, M., Nava, A., Valtorta, D., Snedeker, J. G. & Mazza, E. Mechanical Characterization of the Liver Capsule and Parenchyma. in *Biomedical Simulation* (eds. Harders, M. & Székely, G.) 150–158 (Springer, 2006). doi:10.1007/11790273_17.

143. Herbert, L. A., Chen, W. C., Hartmann, A. & Garancis, J. C. Mechanical properties of the dog renal capsule. *J. Appl. Physiol.* **40**, 164–170 (1976).

144. Cui, L., Maas, H., Perreault, E. J. & Sandercock, T. G. In situ estimation of tendon material properties: differences between muscles of the feline hindlimb. *J. Biomech.* **42**, 679–685 (2009).

145. Shadwick, R. E. Elastic energy storage in tendons: mechanical differences related to function and age. *J. Appl. Physiol. Bethesda Md 1985* **68**, 1033–1040 (1990).

146. McKee, C. T., Last, J. A., Russell, P. & Murphy, C. J. Indentation versus tensile measurements of Young's modulus for soft biological tissues. *Tissue Eng. Part B Rev.* **17**, 155–164 (2011).

147. Li, J. & Mooney, D. J. Designing hydrogels for controlled drug delivery. *Nat. Rev. Mater.* **1**, 1–17 (2016).

148. Chaudhuri, O. Viscoelastic hydrogels for 3D cell culture. *Biomater. Sci.* **5**, 1480–1490 (2017).

149. Cameron, Andrew. R., Frith, Jessica. E. & Cooper-White, Justin. J. The influence of substrate creep on mesenchymal stem cell behaviour and phenotype. *Biomaterials* **32**, 5979–5993 (2011).

150. Cameron, A. R., Frith, J. E., Gomez, G. A., Yap, A. S. & Cooper-White, J. J. The effect of time-dependent deformation of viscoelastic hydrogels on myogenic induction and Rac1 activity in mesenchymal stem cells. *Biomaterials* **35**, 1857–1868 (2014).

151. Chaudhuri, O. *et al.* Hydrogels with tunable stress relaxation regulate stem cell fate and activity. *Nat. Mater.* **15**, 326–334 (2016).

152. Weisel, J. W. & Litvinov, R. I. Mechanisms of fibrin polymerization and clinical implications. *Blood* **121**, 1712–1719 (2013).

153. Radosevich, M., Goubran, H. A. & Burnouf, T. Fibrin Sealant: Scientific Rationale, Production Methods, Properties, and Current Clinical Use. *Vox Sang.* **72**, 133–143 (1997).

154. Janmey, P. A., Winer, J. P. & Weisel, J. W. Fibrin gels and their clinical and bioengineering applications. *J. R. Soc. Interface* **6**, 1–10 (2008).

155. Litvinov, R. I. & Weisel, J. W. What Is the Biological and Clinical Relevance of Fibrin? *Semin. Thromb. Hemost.* 333–343 (2016) doi:10.1055/s-0036-1571342.

156. Murphy, K. C. & Leach, J. K. A reproducible, high throughput method for fabricating fibrin gels. *BMC Res. Notes* **5**, 423 (2012).

157. Ferri, F. *et al.* Growth kinetics and structure of fibrin gels. *Phys. Rev. E* **63**, 031401 (2001).

158. Benkherourou, M., Guméry, P. Y., Tranqui, L. & Tracqui, P. Quantification and macroscopic modeling of the nonlinear viscoelastic behavior of strained gels with varying fibrin concentrations. *IEEE Trans. Biomed. Eng.* **47**, 1465–1475 (2000).

159. Shpichka, A. I. *et al.* Digging deeper: structural background of PEGylated fibrin gels in cell migration and lumenogenesis. *RSC Adv.* **10**, 4190–4200 (2020).

160. Kita, R., Takahashi, A., Kaibara, M. & Kubota, K. Formation of Fibrin Gel in Fibrinogen−Thrombin System: Static and Dynamic Light Scattering Study. *Biomacromolecules* **3**, 1013–1020 (2002).

161. Sproul, E. P., Hannan, R. T. & Brown, A. C. Controlling Fibrin Network Morphology, Polymerization, and Degradation Dynamics in Fibrin Gels for Promoting Tissue Repair. in *Biomaterials for Tissue Engineering: Methods and Protocols* (ed. Chawla, K.) 85–99 (Springer, 2018). doi:10.1007/978-1-4939-7741-3_7.

162. Raber, M. N. Coagulation Tests. in *Clinical Methods: The History, Physical, and Laboratory Examinations* (eds. Walker, H. K., Hall, W. D. & Hurst, J. W.) (Butterworths, 1990).

163. Weisel, J. W. Which knobs fit into which holes in fibrin polymerization? *J. Thromb. Haemost.* **5**, 2340–2343 (2007).

164. Nelson, A. C. & Fogelson, A. L. Towards understanding the effect of fibrinogen interactions on fibrin gel structure. *Phys. Rev. E* **107**, 024413 (2023).

165. Kostelansky, M. S., Betts, L., Gorkun, O. V. & Lord, S. T. 2.8 Å Crystal Structures of Recombinant Fibrinogen Fragment D with and without Two Peptide Ligands: GHRP Binding to the "b" Site Disrupts Its Nearby Calcium-binding Site. *Biochemistry* **41**, 12124–12132 (2002).

166. Everse, S. J., Spraggon, G., Veerapandian, L., Riley, M. & Doolittle, R. F. Crystal structure of fragment double-D from human fibrin with two different bound ligands. *Biochemistry* **37**, 8637–8642 (1998).

167. Kononova, O. *et al.* Molecular Mechanisms, Thermodynamics, and Dissociation Kinetics of Knob-Hole Interactions in Fibrin*. *J. Biol. Chem.* **288**, 22681–22692 (2013).

168. Guthold, M. *et al.* A Comparison of the Mechanical and Structural Properties of Fibrin Fibers with Other Protein Fibers. *Cell Biochem. Biophys.* **49**, 165–181 (2007).

169. Litvinov, R. I. *et al.* Direct Evidence for Specific Interactions of the Fibrinogen αC-Domains with the Central E Region and with Each Other. *Biochemistry* **46**, 9133–9142 (2007).

170. Houser, J. R. *et al.* Evidence that αC Region Is Origin of Low Modulus, High Extensibility, and Strain Stiffening in Fibrin Fibers. *Biophys. J.* **99**, 3038–3047 (2010).

171. Soon, A. S. C., Lee, C. S. & Barker, T. H. Modulation of fibrin matrix properties via knob:hole affinity interactions using peptide–PEG conjugates. *Biomaterials* **32**, 4406–4414 (2011).

172. Collet, J.-P., Shuman, H., Ledger, R. E., Lee, S. & Weisel, J. W. The elasticity of an individual fibrin fiber in a clot. *Proc. Natl. Acad. Sci. U. S. A.* **102**, 9133–9137 (2005).

173. Roska, F. J. & Ferry, J. D. Studies of fibrin film. I. Stress relaxation and birefringence. *Biopolymers* **21**, 1811–1832 (1982).

174. Kang, H. *et al.* Nonlinear elasticity of stiff filament networks: strain stiffening, negative normal stress, and filament alignment in fibrin gels. *J. Phys. Chem. B* **113**, 3799–3805 (2009).

175. Piechocka, I. K., Bacabac, R. G., Potters, M., MacKintosh, F. C. & Koenderink, G. H. Structural Hierarchy Governs Fibrin Gel Mechanics. *Biophys. J.* **98**, 2281–2289 (2010).

176. Hudson, N. E. *et al.* Stiffening of Individual Fibrin Fibers Equitably Distributes Strain and Strengthens Networks. *Biophys. J.* **98**, 1632–1640 (2010).

177. Conti, E. & MacKintosh, F. C. Cross-Linked Networks of Stiff Filaments Exhibit Negative Normal Stress. *Phys. Rev. Lett.* **102**, 088102 (2009).

178. Purohit, P. K., Litvinov, R. I., Brown, A. E. X., Discher, D. E. & Weisel, J. W. Protein unfolding accounts for the unusual mechanical behavior of fibrin networks. *Acta Biomater.* **7**, 2374–2383 (2011).

179. Litvinov, R. I., Faizullin, D. A., Zuev, Y. F. & Weisel, J. W. The α-Helix to β-Sheet Transition in Stretched and Compressed Hydrated Fibrin Clots. *Biophys. J.* **103**, 1020–1027 (2012).

180. Wen, Q., Basu, A., Janmey, P. A. & Yodh, A. G. Non-affine deformations in polymer hydrogels. *Soft Matter* **8**, 8039–8049 (2012).

181. Litvinov, R. I. & Weisel, J. W. Fibrin mechanical properties and their structural origins. *Matrix Biol.* **60–61**, 110–123 (2017).

182. Sundaram, M. N. *et al.* Bioadhesive, Hemostatic, and Antibacterial in Situ Chitin–Fibrin Nanocomposite Gel for Controlling Bleeding and Preventing Infections at Mediastinum. *ACS Sustain. Chem. Eng.* **6**, 7826–7840 (2018).

183. Litvinov, R. I. *et al.* Molecular Mechanism of Transition from Catch-Bond to Slip-Bond in Fibrin. *arXiv.org* https://arxiv.org/abs/1709.05727v1 (2017) doi:10.48550/arXiv.1709.05727.

184. Litvinov, R. I. *et al.* Regulatory element in fibrin triggers tension-activated transition from catch to slip bonds. *Proc. Natl. Acad. Sci.* **115**, 8575–8580 (2018).

185. Maksudov, F. *et al.* Strength, deformability and toughness of uncrosslinked fibrin fibers from theoretical reconstruction of stress-strain curves. *Acta Biomater.* **136**, 327–342 (2021).

186. Brown André, E. X., Litvinov, R. I., Discher, D. E. & Weisel, J. W. Forced Unfolding of Coiled-Coils in Fibrinogen by Single-Molecule AFM. *Biophys. J.* **92**, L39–L41 (2007).

187. Pancaldi, F., Kim, O. V., Weisel, J. W., Alber, M. & Xu, Z. Computational biomechanical modeling of fibrin networks and platelet-fiber network interactions. *Curr. Opin. Biomed. Eng.* **22**, 100369 (2022).

188. Sree, V. D. & Tepole, A. B. Computational systems mechanobiology of growth and remodeling: Integration of tissue mechanics and cell regulatory network dynamics. *Curr. Opin. Biomed. Eng.* **15**, 75–80 (2020).

189. Guo, Y., Calve, S. & Tepole, A. B. Multiscale mechanobiology: Coupling models of adhesion kinetics and nonlinear tissue mechanics. *Biophys. J.* **121**, 525–539 (2022).

190. Sander, E. A., Barocas, V. H. & Tranquillo, R. T. Initial Fiber Alignment Pattern Alters Extracellular Matrix Synthesis in Fibroblast-Populated Fibrin Gel Cruciforms and Correlates with Predicted Tension. *Ann. Biomed. Eng.* **39**, 714–729 (2011).

191. Chen, C., Wang, Z. & Suo, Z. Flaw sensitivity of highly stretchable materials. *Extreme Mech. Lett.* **10**, 50–57 (2017).

192. Lange, F. *et al.* Connectivity and Structural Defects in Model Hydrogels: A Combined Proton NMR and Monte Carlo Simulation Study. *Macromolecules* **44**, 9666–9674 (2011).

193. Wang, E. & Escobedo, F. Swelling and Tensile Properties of Tetra-Polyethylene glycol via Coarse-Grained Molecular Models. *Macromol. Theory Simul.* **26**, 1600098 (2017).

194. Aghvami, M., Billiar, K. L. & Sander, E. A. Fiber Network Models Predict Enhanced Cell Mechanosensing on Fibrous Gels. *J. Biomech. Eng.* **138**, (2016).

195. Zohravi, E., Moreno, N. & Ellero, M. Computational Mesoscale Framework for Biological Clustering and Fractal Aggregation. 2023.02.14.528441 Preprint at https://doi.org/10.1101/2023.02.14.528441 (2023).

196. Filla, N., Zhao, Y. & Wang, X. Fibrin fiber deformation mechanisms: insights from phenomenological modeling to molecular details. *Biomech. Model. Mechanobiol.* (2023) doi:10.1007/s10237-022-01685-z.

197. Frenkel, D. & Smit, B. *Understanding Molecular Simulation: From Algorithms to Applications*. (Elsevier, 2001).

198. Delong, S., Balboa Usabiaga, F. & Donev, A. Brownian dynamics of confined rigid bodies. *J. Chem. Phys.* **143**, 144107 (2015).

199. Moore, F., Russo, J., Liverpool, T. B. & Royall, C. P. Active Brownian particles in random and porous environments. *J. Chem. Phys.* **158**, 104907 (2023).

200. Markutsya, S., Subramaniam, S., Vigil, R. D. & Fox, R. O. On Brownian Dynamics Simulation of Nanoparticle Aggregation. *Ind. Eng. Chem. Res.* **47**, 3338–3345 (2008).

201. Blundell, J. R. & Terentjev, E. M. Buckling of semiflexible filaments under compression. *Soft Matter* **5**, 4015–4020 (2009).

202. Subramaniyan, A. K. & Sun, C. T. Continuum interpretation of virial stress in molecular simulations. *Int. J. Solids Struct.* **45**, 4340–4346 (2008).

203. Zhmurov, A. *et al.* Atomic Structural Models of Fibrin Oligomers. *Structure* **26**, 857-868.e4 (2018).

204. Stukowski, A. Visualization and analysis of atomistic simulation data with OVITO–the Open Visualization Tool. *Model. Simul. Mater. Sci. Eng.* **18**, 015012 (2009).

205. Falvo, M. R., Millard, D., O'Brien, E. T., Superfine, R. & Lord, S. T. Length of Tandem Repeats in Fibrin's αC Region Correlates with Fiber Extensibility. *J. Thromb. Haemost. JTH* **6**, 1991–1993 (2008).

206. Ferry, J. D. The Mechanism of Polymerization of Fibrinogen*. *Proc. Natl. Acad. Sci.* **38**, 566–569 (1952).

207. Yesudasan, S. & Averett, R. D. Fracture mechanics analysis of fibrin fibers using mesoscale and continuum level methods. *Inform. Med. Unlocked* **23**, 100524 (2021).

208. Weisel, J. W., Nagaswami, C. & Makowski, L. Twisting of fibrin fibers limits their radial growth. *Proc. Natl. Acad. Sci. U. S. A.* **84**, 8991–8995 (1987).

209. Piechocka, I. K. *et al.* Multi-scale strain-stiffening of semiflexible bundle networks. *Soft Matter* **12**, 2145–2156 (2016).

210. Liu, W. *et al.* Fibrin fibers have extraordinary extensibility and elasticity. *Science* **313**, 634 (2006).

211. Burton, R. A., Tsurupa, G., Medved, L. & Tjandra, N. Identification of an Ordered Compact Structure within the Recombinant Bovine Fibrinogen αC-Domain Fragment by NMR. *Biochemistry* **45**, 2257–2266 (2006).

212. Tsurupa, G., Tsonev, L. & Medved, L. Structural Organization of the Fibrin(ogen) αC-Domain. *Biochemistry* **41**, 6449–6459 (2002).

213. Gorkun, O. V., Veklich, Y. I., Medved', L. V., Henschen, A. H. & Weisel, J. W. Role of the .alpha.C Domains of Fibrin in Clot Formation. *Biochemistry* **33**, 6986–6997 (1994).

214. Smith, L. R., Cho, S. & Discher, D. E. Stem Cell Differentiation is Regulated by Extracellular Matrix Mechanics. *Physiol. Bethesda Md* **33**, 16–25 (2018).

215. Dobrynin, A. V. & Carrillo, J.-M. Y. Universality in Nonlinear Elasticity of Biological and Polymeric Networks and Gels. *Macromolecules* **44**, 140–146 (2011).

216. Kurniawan, N. A., Wong, L. H. & Rajagopalan, R. Early Stiffening and Softening of Collagen: Interplay of Deformation Mechanisms in Biopolymer Networks. *Biomacromolecules* **13**, 691–698 (2012).

217. Fernández-Castaño Romera, M. *et al.* Strain-Stiffening in Dynamic Supramolecular Fiber Networks. *J. Am. Chem. Soc.* **140**, 17547–17555 (2018).

218. Jacobs, M. & Dobrynin, A. V. Deformation Model of Chains and Networks with Extendable Bonds. *Macromolecules* **53**, 10874–10881 (2020).

219. Sun, B. The mechanics of fibrillar collagen extracellular matrix. *Cell Rep. Phys. Sci.* **2**, 100515 (2021).

220. Kim, O. V., Litvinov, R. I., Weisel, J. W. & Alber, M. S. Structural basis for the nonlinear mechanics of fibrin networks under compression. *Biomaterials* **35**, 6739–6749 (2014).

221. Richardson, B. M., Wilcox, D. G., Randolph, M. A. & Anseth, K. S. Hydrazone covalent adaptable networks modulate extracellular matrix deposition for cartilage tissue engineering. *Acta Biomater.* **83**, 71–82 (2019).

222. Crespo-Cuevas, V., Ferguson, V. L. & Vernerey, F. Poroviscoelasto-plasticity of agarose-based hydrogels. *Soft Matter* **19**, 790–806 (2023).

223. Ridgway, H. J., Brennan, S. O., Faed, J. M. & George, P. M. Fibrinogen Otago: a major alpha chain truncation associated with severe hypofibrinogenaemia and recurrent miscarriage. *Br. J. Haematol.* **98**, 632–639 (1997).

224. Soria, J., Soria, C. & Caen, P. A new type of congenital dysfibrinogenaemia with defective fibrin lysis--Dusard syndrome: possible relation to thrombosis. *Br. J. Haematol.* **53**, 575–586 (1983).

225. Lijnen, H. R., Soria, J., Soria, C., Collen, D. & Caen, J. P. Dysfibrinogenemia (fibrinogen Dusard) associated with impaired fibrin-enhanced plasminogen activation. *Thromb. Haemost.* **51**, 108–109 (1984).

226. Morris, T. A. *et al.* High prevalence of dysfibrinogenemia among patients with chronic thromboembolic pulmonary hypertension. *Blood* **114**, 1929–1936 (2009).

227. Normand, V., Lootens, D. L., Amici, E., Plucknett, K. P. & Aymard, P. New Insight into Agarose Gel Mechanical Properties. *Biomacromolecules* **1**, 730–738 (2000).

APPENDIX I: INTRINSIC PERMEABILITY AND VOID RATIO EVOLUTION IN AGAROSE GELS

The intrinsic permeability κ for agarose gels was defined using the evolutions equations described by Gu *et al.* (2003)[86].

$$\kappa = \kappa_0 \left(\frac{J_e - \phi_0}{1 - \phi_0}\right)^n, \phi = \frac{\phi_0}{J_e} \quad (20)$$

Therefore, in this study, the intrinsic permeability κ and the solid volume fraction ϕ were assumed to be a function of the macroscopic deformation applied on the gel, in this case using the Jacobian J_e of the elastic deformation gradient tensor $\boldsymbol{F_e}$. The initial permeability was defined as $\kappa_0 = p_1 \left(\frac{1-\phi_0}{\phi_0}\right)^{p_2}$ where p_1 and p_2 were fitting parameters. Here, the initial solid volume fraction ϕ_0 was obtained using the relationship established by Pluen *et al.* (1999)[101]; $\phi_0 = \frac{1}{\rho_{agarose}\omega_{agarose}} c_o$ where c_o is the agarose concentration, $\rho_{agarose}$ = 1.64 g/ml is the dry agarose density[102] and $\omega_{agarose}$ = 0.625 is the mass fraction of agarose in a fiber[103].

The initial hydraulic conductance K was defined as $K = \frac{\gamma_s}{\mu}\kappa$ where μ is the dynamic viscosity of the fluid and γ_s is the specific weight of the fluid. Since the fluid was a PBS solution, μ = 1E-9 N·s/mm^2 and γ_s = 9.81E-06 N/mm^3. Once ϕ was calculated and assuming the porosity $\theta = 1 - \phi$, the void ratio was defined as $e_0 = \frac{\theta_0}{1-\theta_0} = \frac{J_e}{\phi_0} - 1$. Values were summarized in Table 2 and assumed to remain constant during the whole deformation process.

c_0[%]	ϕ_0[%]	e_0	κ_0 [mm^2]	K_0 [mm/s]
5	4.88	19.5	2.32E-11	2.56E-07
7.5	7.32	12.67	1.22E-11	1.22E-07
10	9.76	9.25	7.75E-12	7.60E-08

Table A1. Parameters used to describe poromechanics for each agarose composition used in the study.

APPENDIX II: CAUCHY STRESS AND TANGENT STIFFNESS MATRIX DERIVATION

To derive the required expressions for the implementation of the TNT into Abaqus, we first rewrote the elastic energy as:

$$\psi = c_{10}(\bar{I}_1 - 3) + \frac{1}{D_1}(J_e - 1)^2 \tag{21}$$

We here assumed elastic compressibility but inelastic incompressibility (from Equation 6). Consequently, in the remainder of our derivations, $J_e = J$. The constitutive equation for the Cauchy stress can be written directly in terms of the deformation gradient[32]:

$$\sigma_{ij} = \frac{2}{J}\mu_{ik}\frac{\partial \psi}{\partial \mu_{kj}} \tag{22}$$

Now we compute the derivatives of the invariants $\bar{I}_1$, $\bar{I}_2$ and J with respect to the conformation tensor $\boldsymbol{\mu}$ components

$$\frac{\partial \psi}{\partial \mu_{ij}} = \frac{\partial \psi}{\partial \bar{I}_1}\frac{\partial \bar{I}_1}{\partial \mu_{ij}} + \frac{\partial \psi}{\partial \bar{I}_2}\frac{\partial \bar{I}_2}{\partial \mu_{ij}} + \frac{\partial \psi}{\partial J}\frac{\partial J}{\partial \mu_{ij}}, \tag{23}$$

and obtain the stress expression

$$\sigma_{ij} = \frac{2}{J}\left[\frac{1}{J^{\frac{2}{3}}}\left(\frac{\partial \psi}{\partial \bar{I}_1} + \bar{I}_1\frac{\partial \psi}{\partial \bar{I}_2}\right)\mu_{ij} - \frac{1}{3}\left(\bar{I}_1\frac{\partial \psi}{\partial \bar{I}_1} + 2\bar{I}_2\frac{\partial \psi}{\partial \bar{I}_2}\right)\delta_{ij} - \frac{1}{J^{\frac{4}{3}}}\frac{\partial \psi}{\partial \bar{I}_2}\mu_{ik}\mu_{kj}\right] + \frac{\partial \psi}{\partial J}\delta_{ij} \tag{24}$$

In our case

$$\sigma_{ij} = \frac{2}{J}c_{10}\left(\bar{\mu}_{ij} - \frac{1}{3}\delta_{ij}\bar{\mu}_{kk}\right) + \frac{2}{D_1}(J-1)\delta_{ij} \tag{25}$$

To obtain the tangent stiffness matrix we first need to define virtual rate of deformation

$$\delta D_{ij} = \frac{1}{2}\left(\delta F_{im}\, F_{mj}^{-1} + F_{im}^{-1}\, \delta F_{jm}\right) = \frac{1}{2}\left(L_{ij} + L_{ji}\right) \tag{26}$$

The Kirchhoff stress is

$$\tau_{ij} = J\, \sigma_{ij} \tag{27}$$

The material Jacobian derives from the variation in Kirchhoff stress.

$$\tau_{ij} = J\, C_{ijkl}\, \delta D_{kl} \tag{28}$$

then

$$C_{ijkl} = \frac{2}{J} c_{10} \left[\frac{1}{2}\left(\delta_{ij}\bar{\mu}_{jl} + \bar{\mu}_{ik}\delta_{jl} + \delta_{il}\bar{\mu}_{jk} + \bar{\mu}_{il}\delta_{jk}\right) - \frac{2}{3}\left(\delta_{ij}\bar{\mu}_{kl} + \bar{\mu}_{ij}\delta_{kl} + \frac{1}{3}\delta_{ij}\delta_{kl}\bar{\mu}_{mm}\right)\right] + \frac{2}{D_1}(J_e - 1)\delta_{ij}\delta_{kl} \tag{29}$$

$$c_{10} = \frac{E}{4(1+\nu)} \text{ and } D_1 = \frac{6(1-2\nu)}{E}$$

APPENDIX III: FITTING PROCEDURE LINKING ABAQUS AND MATLAB

To estimate the input material parameters (k_d^I, k_d^{II}, α, β, γ and k_{d0}^I) of agarose gels, an optimization procedure linking Abaqus and MATLAB (MathWorks, Natick, MA, USA) was developed. Briefly, initial guess values of the material parameters were assigned in the input file model and the Abaqus run was executed to compute the system contact force response F^{sim}. Then, the sum of root-mean-square error in the contact force was defined as

$$SE = min \sum_{i=1}^{n} \left(F_i^{test} - F_i^{sim}\right)^2 \quad (30)$$

where n is the number of iterations. Subsequently, an optimization algorithm was used to iteratively calculate the value of the input variables by minimizing the objective function SE. For solving the optimization problem, the in-house code was used based on the MATLAB function *fminsearch*. The lower and upper bounds in the function were properly chosen to accommodate a wide range of values for each of the material properties.

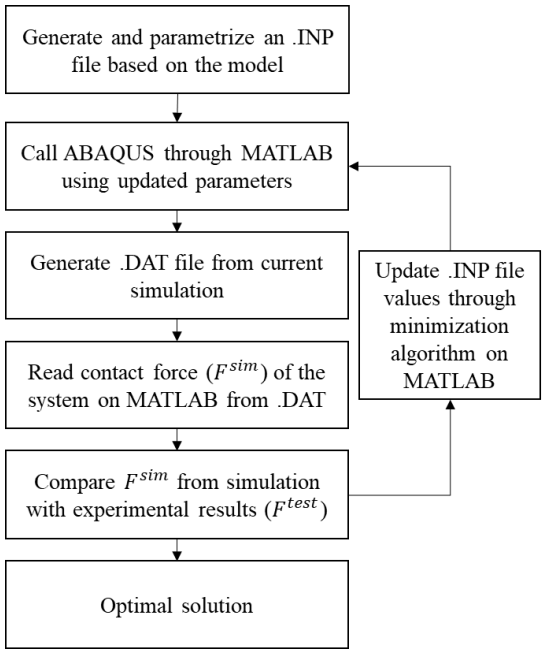

APPENDIX IV: ELASTIC MODULUS OF THE SOLID NETWORK E_S AND AGGREGATE MODULUS H_A

Once the Poisson's ratio was properly determined and set to $\nu_s = 0.17$; the elastic modulus of the solid network E_s was obtained using the fitting procedure described on Appendix III. This procedure was repeated for each of the four loading steps for every sample. Fully swollen agarose gels exhibited an elastic response with a strong correlation between stress/strain ($R^2 \approx 1$). Most studies in the literature report the aggregate modulus H_A instead of the elastic modulus of the solid network. The aggregate modulus for different agarose composition can however be obtained directly from E_s and ν_s as:

$$H_A = \frac{3}{2}\frac{(1-2\nu_s)}{(1-\nu_s)}E_s \qquad 31$$

At 5% strain and before relaxation, the mean aggregate modulus values could therefore be estimated as 0.97 MPa, 1.7 MPa, and 2.43 MPa for 5%, 7.5% and 10% w/w agarose respectively. These results were in excellent agreement with the previously reported by Normand *et al.* (2000)[227]. During the compressive stage that followed stress relaxation, we further observed an increase in the aggregate modulus with respect to its initial value. In this study, H_A was observed to exponentially increase with applied deformation in the following fashion ($R^2 \approx 1$) (Figure 11):

$$H_A = a(\bar{\mu})^b + c \qquad 32$$

Values for fitting parameters were summarized in Table A2.

c_o	a	b	c
5% w/w	7.27E5	10.86	0.97
7.5% w/w	1.92E6	11.31	1.70
10% w/w	3.65E6	11.76	2.44

Table A2. Control parameters a, b, and c as a function of the agarose concentration c_o used in the samples.

The parameter c was directly related to the elastic modulus found at 5% strain (H_A^0) before the network had time to relax. This fact motivated the idea of finding the following master equation as a function of the agarose concentration c_o.

$$H_A = H_A^0\left[\frac{3}{2}10^6 c_o(\bar{\mu})^b + 1\right] \qquad 33$$

The master Equation 27 shows that agarose network becomes stiffer as the overall deformation is increased and held during large periods of time. Parameter b increases as the concentration of agarose in the samples increases. However, we found that assuming parameter b constant and equal to the average of the values shown on Table 3 $\left(\bar{b} = 11.3\right)$ did not have major differences in the fitted curves shown in Figure 9.

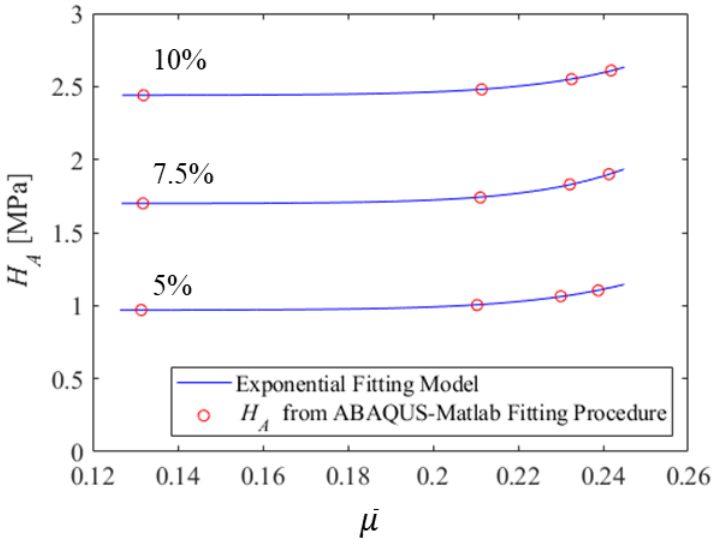

Figure A1. Evolution of the aggregate modulus H_A as a function of the second invariant of the conformation tensor $\bar{\mu}$.